University of Texas at El Paso

ScholarWorks@UTEP

Open Access Theses & Dissertations

2023-05-01

Computational Analysis Of Water Braking Phenomena For High-Speed Sled And Its Machine Learning Framework

Jose A. Terrazas
University of Texas at El Paso

Recommended Citation

COMPUTATIONAL ANALYSIS OF WATER BRAKING PHENOMENA FOR HIGH-SPEED

SLED AND ITS MACHINE LEARNING FRAMEWORK

JOSE ARMANDO TERRAZAS

Doctoral Program in Mechanical Engineering

APPROVED:

_____

Vinod Kumar, Ph.D., Chair

_____

Robert Edmonds, Ph.D., Co-Chair

_____

V.M. Krushnarao Kotteda, Ph.D.

_____

Jorge Munoz, Ph.D.

_____

Art Bronson, Ph.D.

_____

Oscar Mondragon, Ph.D.

_____

Stephen L. Crites, Jr., Ph.D.
Dean of the Graduate School

Dedication

I dedicate this work to my mom, brother, sister, cousins, family, and friends that helped me along the way, for their constant support and encouragement.

I would also like to dedicate this work to all my mentors since middle school, high school, and college that saw potential in me and set me on this path.

Finally, to my graduate advisors and mentors that encouraged me to complete this work and helped me develop intellectually.

COMPUTATIONAL ANALYSIS OF WATER BRAKING PHENOMENA FOR HIGH-SPEED

SLED AND ITS MACHINE LEARNING FRAMEWORK

by

JOSE ARMANDO TERRAZAS, MSSE

DISSERTATION

Presented to the Faculty of the Graduate School of

The University of Texas at El Paso

in Partial Fulfillment

of the Requirements

for the Degree of

DOCTOR OF PHILOSOPHY

Department of Aerospace and Mechanical Engineering

THE UNIVERSITY OF TEXAS AT EL PASO

May 2023

Acknowledgements

Abstract

Specializing in high-speed testing, Holloman High-Speed Test Track (HHSTT) uses a process called 'water braking' as a method to bring vehicles at the test track to a stop. This method takes advantage of the higher density of water, compared to air, to increase braking capability through momentum exchange. By studying water braking using Computational Fluid Dynamics (CFD), forces acting on track vehicles can be approximated and prepared for prior to the actual test. In this study, focus will be made on the brake component of the track sled that is responsible for interacting with the water for braking. By discretizing a volume space around our brake, we accelerate water and air to relatively simulate the brake engaging. The model is a multi-phase flow that uses the governing equations of gas and liquid phases with the finite volume method, to perform 3D simulations. By adjusting the inflow velocity of air and water, it is possible to simulate HHSTT sled tests at various operational speeds. In the development of the 3D predictive model, convergence issues associated with the numerical mesh, initial/boundary conditions, and compressibility of the fluids were encountered. Once resolved, the effect of inflow velocities of water and air on the braking of the sled is studied.

Improving the prediction capabilities of water braking phenomena has the potential to result in radical changes in the designs of sleds, improve rocket sled velocity-time test profile predictions, provide greater confidence of braking mechanisms, and decrease risk in the recovery of critical infrastructures. Understanding the water's behavior with the sled is critical to predicting how the water could damage the sled, which affects the recoverability of the sled and can determine the success of a mission, and the amount of drag it will experience from the air and water. Traditionally, sled design for the test missions for water braking has been guided by empirical/hand calculations to estimate the forces on various components. The calculations

involve various approximations in arriving at the force balance law and predicting the acceleration/deceleration profile. The CFD results from various geometry configurations for the sled and modeling parameters will be presented. The main goals of the CFD investigations are to improve the accuracy of the predicted profile that often depends on the complexity of the design and operating conditions.

Due to CFD modeling being very computationally expensive, however, a machine learning (ML) framework is suggested to increase result turnover and fidelity. This framework consists of multiple neural networks that once trained are to be validated and coupled. In addition to the framework, a project management plan is outlined to guide the integration of computational modeling with the machine learning framework.

In summary, five different geometries of the sled water braking mechanism, scoop, are simulated in a 3-dimensional space and a machine learning framework is provided to offset the CFD requirement of expensive computational resources.

Table of Contents

List of Tables

List of Figures

List of Plots

Chapter 1: Introduction

Advances, accessibility, and increasing computational capability in the past few years has made it possible to model and solve, within small error, complex system of equations that approximate fluid flows with enough accuracy to make the results useful for engineering analysis. These complex systems of equations are known as Navier – Stokes Equations and are used to imitate a wind tunnel and fluid phenomena in a virtual space. The development and solving of these virtual models are what Computational Fluid Dynamics (CFD) is about. By using CFD, engineers and scientists can analyze and study fluids in a quick, cost effective, non-intrusive, and feasible manner compared to running real tests and experiments. To this end, CFD modeling is a great tool for the US Air Force (USAF) at HHSTT because they work with pusher sleds to test vehicles under high-speed conditions. CFD allows for better engineering, building and predictability of the braking files of the vehicles being tested. Improving the design of the pusher sleds allows for better breaking performance and reusability which will decrease the cost of testing in the track and increase the speeds at which the vehicles can be tested.

Just as computational capability and advances have enabled CFD, they have also made Machine Learning (ML) through Neural Networks (NN) possible. Machine Learning enables statistics to learn how to perform a specific task independently. It has characteristics in several different fields, including artificial intelligence, statistics, and computer science [29].

By combining CFD and ML it will lead to an improved USAF capability to engineer, test, and analyze testing models at HHSTT. In this study, we review CFD of water braking and suggest the framework of coupled neural nets (NN) to use along with CFD data. The NN suggested in the framework are a Super Resolution Neural Net to increase "fidelity" of data and a new type of Neural Net known as Physics Informed Neural Net (PINN) to speed up accuracy and speed of fluid

flow simulations. Along with these NN, transfer learning is suggested to reduce training of future NN compared to past NN. To couple everything together a high-level management plan is also suggested. We will then conclude with a discussion of the expected outcome from integration of all tools to improve HHSTT ability to model and predict test profiles for water braking along with future work.

The main problems this research is meant to solve are reduction of distance required for braking, increasing water braking capability, and engaging water braking at faster velocities. The objective of this work is to model three-dimensional multi-phase flows, identify geometric features that improve sled drag performance and quantify such improvements, perform sensitivity analysis on different modeling parameters, and to develop framework to address high computational cost, fidelity, and turnaround time associated with computational fluid dynamics. To accomplish them, three questions must be answered.

- How does boundary layer transition influence turbulence and the effects of drag and lift forces acting on the sled?
- How effective can CFD be in modeling multi-physics phenomena and how may this tool be leveraged to improve capability of testing capability at HHSTT?
- How can advances in machine learning be leveraged to mitigate computational expense associated with CFD?

Chapter 2: Technical Background

To successfully complete and analyze CFD models in this study we must understand the technical components that make it up. Since we will be braking with drag from air and water, we will review fluid flows and the equations governed by them. In this section we will go over the technical components required and used to successfully obtain CFD results in the scope of our study. Additionally, we will also review ML and NNs.

2.1 COMPUTATIONAL FLUID DYNAMICS (CFD)

By solving a group of partial differential equations, it is possible to model fluids virtually. Before CFD was possible, engineers and scientists had to do testing and studies in specially designed testing set ups such as wind tunnels. Although relatively expensive testing set ups are still done, CFD offers many benefits over real world testing. A list of benefits include cost, turnaround time, exact similarity, non-intrusive measuring, analysis, feasibility, and extendibility. A list of disadvantages includes turbulence, accuracy, and error control.

Building, operating, and maintaining a test lab can be expensive, there are so many variables to consider. Size of object being tested, simulating testing conditions, construction of actual test object, number of tests being performed, and staff, just to name a few. CFD provides an opportunity, if done right, to mitigate costs as unique tests with variable conditions can be easily altered with comparatively little cost, time, and effort. Also, to gather data on real world tests, sensors must be used. These sensors can perturb or intrude flows and alter results not to mention that data may only be collected at sensor location, in this too CFD has an advantage. With CFD you do not need intrusive sensors and data can be collected on any point of the testing item not just on selected points which can lead to better analysis and understanding of fluid behavior or

impact. Another advantage is that conditions that may not be measured experimentally may be measured virtually, for example gas effects on a missile during reentry.

All the benefits, however, are not without disadvantages and experimental testing is sometimes still necessary. Turbulence models in 3-D for example involve very small flow features at high Reynolds numbers that even with today's super computers is still impossible to simulate all the details [28]. This in turn, depending on tolerance for error, can make CFD too inaccurate. Errors incurred from the insufficient detail of turbulence models can make the model's accuracy unquantifiable.

Despite the drawbacks CFD is still a key technology that when used right can offer substantial value. For some flows CFD will only be able to provide qualitative results but they may provide some insight that may be used for a better experimental setup. The components needed for a CFD solution are a physical model, a mathematical model, a numerical method, the mesh, and pre- and post-processing tools [28].

2.1.1 Physical Model

The physical model is the most basic component to CFD, it is the geometry of the test object and where the space or environment in which it will be modeled is defined. The physical model does require assumptions to make the model simpler and solvable, this includes boundary conditions, continuum assumption, the type of flow description, and conservation principles.

When building a fluid dynamics model, we are usually not concerned with tracking individual particles of molecular or atomic size. The particles are too small, the number of particles to track would be unnecessarily large, and the impact individual particles would have on a body in terms of lift and drag in our study would be negligibly minor. For this reason, an assumption made

in this study is the continuum assumption. The effect of this assumption is that we consider the statistical average of the particles bulk flow [28].

When analyzing dynamics there are two ways to do describe them, Eulerian and Lagrangian. In this study we will do it from the Eulerian viewpoint as it allows for the use of a control volume in which conservation of momentum principles apply.

Building on continuum and control volume principles we consider the balance of transported quantities in that control volume. It is then possible to define and analyze at each location in space how much mass, momentum, and energy is entering and exiting each space.

2.1.2 Mathematical Model

Once assumptions and conservation of momentum and mass are established from the Physical Model, mathematical equations based on them can be derived. To examine the conservation of momentum equations let us begin with an example in 1 dimension by assuming constant flow in y and z. By assuming constant flow in y and z we are left with variations in the x direction only. We will derive the equations for mass conservation in 1-D x-coordinate and then apply it to y and z cartesian coordinates, see figure 2.1. First, we will use Taylor's expansion
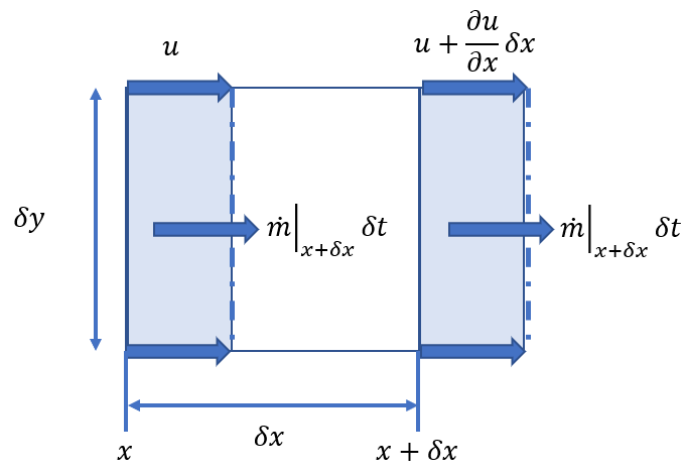
Figure 2.1 Conservation of mass on 1-dimensional fluid element

to approximate the mass flux $(pu)|_{x+\delta x}$ at the right edge of the element $x + \delta x$ in terms of mass flux $(pu)|_x$ at x:

$$(pu)|_{x+\delta x} = (pu)|_x + \frac{d(\rho u)}{dx}\delta x + \frac{1}{2}\frac{d^2(\rho u)}{dx^2}\delta x^2 + O(\delta x^3) \tag{2.1}$$

From Figure 2.1 we can then see that the fluid entering on the left-hand side at x in time δt is

$$\dot{m}|_x \delta t = (pu)|_x \delta y \delta z \delta t \tag{2.2}$$

And the amount of fluid exiting on the right-hand side $x + \delta x$ in the same time interval δt is

$$\dot{m}|_{x+\delta x}\delta t = (pu)|_{x+\delta x}\delta y \delta z \delta t \tag{2.3}$$

From these equations we can then get change in mass in the control volume in time δt by subtracting fluid entering $\dot{m}|_x \delta t$ from $\dot{m}|_{x+\delta x}\delta t$ and multiplying it by the time interval δt.

$$\delta m = \dot{m}|_x \delta t - \dot{m}|_{x+\delta x}\delta t$$
$$\delta m = (pu)|_x \delta y \delta z \delta t - (pu)|_{x+\delta x}\delta y \delta z \delta t \tag{2.4}$$

Then using Taylor expansion for pu we obtain

$$\delta m = ((pu)|_x)\delta y \delta z \delta t - \left((pu)|_x + \frac{d(\rho u)}{dx}\delta x + \frac{1}{2}\frac{d^2(\rho u)}{dx^2}\delta x^2 + O(\delta x^3)\right)\delta y \delta z \delta t$$

Which simplifies to

$$\delta m = -\left(\frac{d(\rho u)}{dx}\delta x + \frac{1}{2}\frac{d^2(\rho u)}{dx^2}\delta x^2 + O(\delta x^3)\right)\delta y \delta z \delta t$$

Divide by size of control volume $\delta x \delta y \delta z$ and time interval δt to end up with

$$\frac{\delta m}{\delta x\, \partial y \delta z \delta t} = \frac{\delta \rho}{\delta t} = -\frac{d(\rho u)}{dx} - \frac{1}{2}\frac{d^2(\rho u)}{dx^2}\delta x + O(\delta x^2) \qquad (2.5)$$

The mass flow gradient $\frac{d(\rho u)}{dx}$ can be relatively large but if we make the size of the element δx sufficiently small, $\lim \delta x \to 0$ then $\delta x \ll 1$ and the second and third term on the right side of (2.5) become negligible. We are then left with

$$\frac{\delta \rho}{\delta t} = -\frac{d(\rho u)}{dx} = -\rho\frac{du}{dx} - u\frac{d\rho}{dx} \qquad (2.6)$$

Because we will be braking with water we take the case of incompressible flow in which density is constant, $\rho = $ constant, and therefore cannot vary so $\frac{d\rho}{dx} = 0$. This means that we end up with

$$\frac{\delta \rho}{\delta t} = -\rho\frac{du}{dx} \qquad (2.7)$$

And if there is no variation in y and z then velocity can not vary so $\frac{du}{dx} = 0$ so

$$\frac{\delta \rho}{\delta t} = 0 \qquad (2.8)$$

This becomes important when looking at velocity variations when we couple velocity components in x, y, and z in a continuity equation.

In 3-dimensional mass conservation we will start with (2.4) but in all cartesian coordinates.

$$\delta m = \dot{m}|_x \delta t \; - \; \dot{m}|_{x+\delta x}\delta t \; + \;\; \delta m = \dot{m}|_y \delta t \; - \; \dot{m}|_{y+\delta y}\delta t \;\;\; + \delta m = \dot{m}|_z \delta t \; - \; \dot{m}|_{z+\delta z}\delta t \qquad (2.9)$$

As a result, we end up with

$$\delta m = \; -\frac{d(\rho u)}{dx}\delta x \delta y \delta z \delta t \;\; -\frac{d(\rho v)}{dy}\delta x \delta y \delta z \delta t \;\; -\frac{d(\rho w)}{dz}\delta x \delta y \delta z \delta t \qquad (2.10)$$

Dividing by the control volume and small enough time steps, lim $\delta t \rightarrow 0$, produces

$$\lim_{\delta t \to 0}\frac{\delta m}{\delta x \, \partial y \delta z \delta t} \;=\; \lim_{\delta t \to 0}\frac{\delta \rho}{\delta t} \;=\; \frac{\partial \rho}{\partial t} \qquad (2.11)$$

By assuming continuity and therefore infinite control volume in 3-D we obtain

$$\frac{\partial \rho}{\partial t} \;+\; \frac{\partial(\rho u)}{\partial x} \;+\; \frac{\partial(\rho v)}{\partial y} \;+\; \frac{\partial(\rho \omega)}{\partial z} = 0 \qquad (2.12)$$

Understanding that $\frac{\partial \rho}{\partial t} = 0$ from our one-dimensional analysis, we end up with

$$\frac{\partial(u)}{\partial x} \;+\; \frac{\partial(v)}{\partial y} \;+\; \frac{\partial(\omega)}{\partial z} = 0 \qquad (2.13)$$

For the incompressible continuity equation.

As we cannot have more mass into a control volume once full, the inflow must balance with the outflow. If flow then slows in the x direction the flow entering at x must flow out the y and z directions. This occurance is the divergence constraint and (2.13) is the divergence of the

8

velocity field that will be coupled in a system of equations that will track fluid flow computationally. In (2.10) we can see the conservation of mass, the difference between what is going in and what is going out must be inside the control volume.

For the derivation of the momentum equations of a fuild, force of moving fluid must be balanced. Because force is a vector and we have three coordinates, we will have three momentum equations. The momentum equations will be derived from Newton's second law F=ma. Using a Eulerian viewpoint established at the beginning of the section we can consider

$$\frac{d(m\vec{v})}{dt} = \vec{F} \tag{2.14}$$

For all of the three coordinate directions.

Because we are working with high speed turbulent flow we assume high Reynold's Number. This means that fluid elements will be able to slide past each other and we can focus on pressure forces and gravity when deriving the equations. Recalling that pressure is a scalar and only acquires direction when acting on a surface, positive pressure will be compressive and pressure on face x will result in a positive force on the x-direction. This means that pressure on the $x + \delta x$ face will be negative, see figure 2.2 to view pressure forces on the faces of a fluid element. The difference in the forces acting on each other will provide us with the net force on the element.

$$F_{p,x} = (p|_x - p|_{x+\delta x})\delta y \delta z \tag{2.15}$$

Using Taylor expansion like in conservation of mass, but this time just in the first order or linear term we get

$$= \left(p|_x - \left(p|_x + \left.\frac{\partial p}{\partial x}\right|_x \delta x\right)\right)\delta y\delta z$$

$$= -\frac{\partial p}{\partial x}\delta x\delta y\delta z = -\frac{\partial p}{\partial x}\delta V \tag{2.16}$$
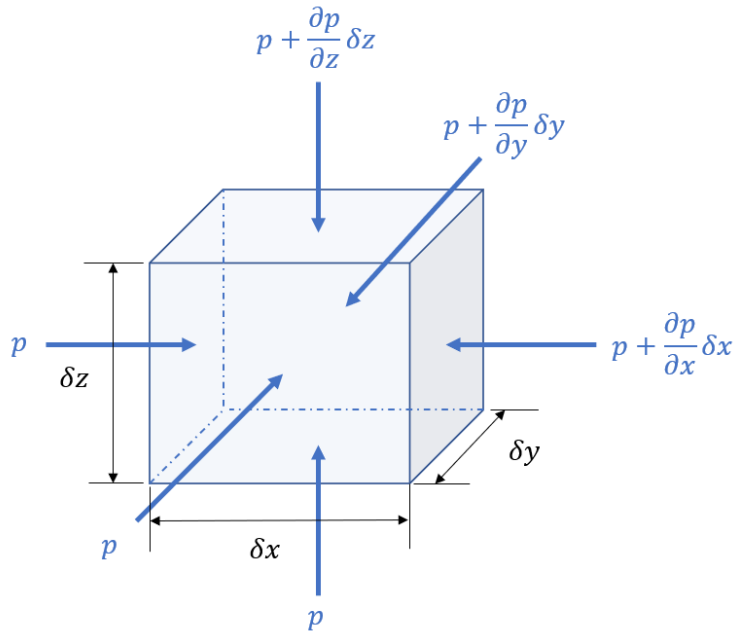
Figure 2.2 Pressure forces on 3-dimensional fluid element

Where δV is the size of the control volume $\delta x\delta y\delta z$. In the same manner as we just derived the

Force component in the x direction, we derive the force on the y and z directions.

$$F_{p,y} = -\frac{\partial p}{\partial y}\delta V \tag{2.17}$$

$$F_{p,z} = -\frac{\partial p}{\partial z}\delta V \tag{2.18}$$

In vector notation the pressure force vector is

$$F_p = \begin{bmatrix} F_{p,x} \\ F_{p,y} \\ F_{p,z} \end{bmatrix}$$

10

Taking into consideration gravity in the -z direction and the sum of all body forces we end up with

x-direction

$$p\left(\frac{\partial u}{\partial t} + u\frac{\partial u}{\partial x} + v\frac{\partial u}{\partial y} + w\frac{\partial u}{\partial z}\right) = -\frac{\partial p}{\partial x} + \mu\left(\frac{\partial^2 u}{\partial x^2} + \frac{\partial^2 u}{\partial y^2} + \frac{\partial^2 u}{\partial z^2}\right) \qquad (2.19)$$

y-direction

$$p\left(\frac{\partial v}{\partial t} + u\frac{\partial v}{\partial x} + v\frac{\partial v}{\partial y} + w\frac{\partial v}{\partial z}\right) = -\frac{\partial p}{\partial y} + \mu\left(\frac{\partial^2 v}{\partial x^2} + \frac{\partial^2 v}{\partial y^2} + \frac{\partial^2 v}{\partial z^2}\right) \qquad (2.20)$$

z-direction

$$p\left(\frac{\partial w}{\partial t} + u\frac{\partial w}{\partial x} + v\frac{\partial w}{\partial y} + w\frac{\partial w}{\partial z}\right) = -\frac{\partial p}{\partial z} + \mu\left(\frac{\partial^2 w}{\partial x^2} + \frac{\partial^2 w}{\partial y^2} + \frac{\partial^2 w}{\partial z^2}\right) - \rho g \qquad (2.21)$$

One more equation to consider is energy balance but it is not always required. For compressible flows yes but inviscid incompressible flows, which is what was used in the study, it is not needed. For those type of flows if it satisfies the momentum equation it will also respect Bernoulli's equation [28].

2.1.2.1 Turbulence Modeling

When a fluid flow interacts with obstructions, such as objects, the flow will transition into turbulence as swirls in the flow manifest, see Figure 2.3. Characteristics affecting this transition include geometry of obstruction, roughness, velocity of flow to name a few. This turbulence phenomenon is chaotic in nature and becomes very important in representing fluid flow along with other parameters in the flow such as velocity, force, and pressure caused by it.
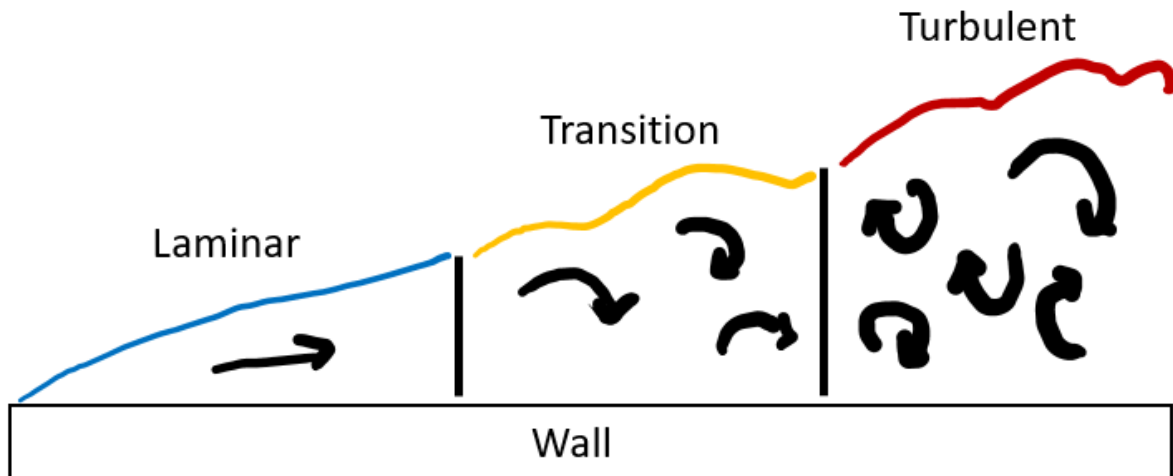
Figure 2.3 Fluid flow transition from laminar to turbulent

"Turbulence is characterized by the existence of eddies, vortical swirls in the fluid, in a variety of scales" [28]. Modeling it is critical to simulating fluid flow as kinetic energy dissipates from larger eddies to smaller ones in the form of heat, see Figure 2.4.
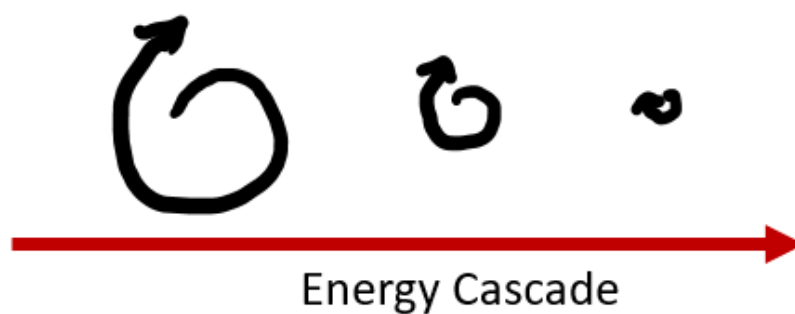
Figure 2.4 Eddy energy cascade

To represent fluid flow three main approaches are used. Going from least accurate to most, they are Reynolds-Averaged Navier-Stokes (RANS), Large Eddy Simulation (LES), and Direct Numerical Simulation (DNS). Though it may be tempting to model turbulence with the greatest fidelity and use DNS, computational costs associated with it make it very computationally expensive for highly turbulent flows. Referencing the characterization of turbulence as eddies, to

12

have a more precise representation of fluid flow the smallest of eddies must be calculated. This requires computation resources needed for DNS to be relatively much more than for LES and RANS as RANS for example does not directly solve all the eddies in the flow. The difference between RANS, LES, and DNS that leads to the difference in fidelity is in the number of eddies resolved. In Figure 2.5, blue arrows represent eddies resolved while black is eddies modeled.
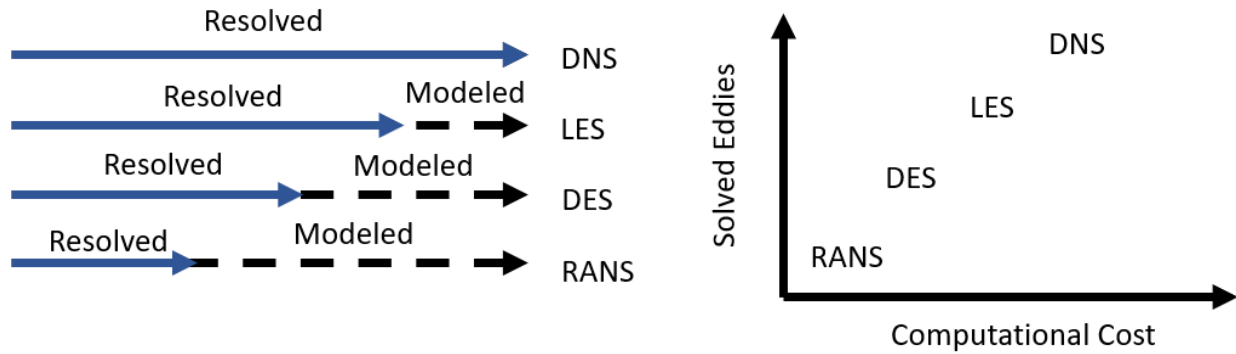
Figure 2.5 Modeling methods and their computational cost

RANS is an option for practical applications in which estimations and quick turnaround times are necessary. LES is a midpoint between DNS and RANS, more time consuming than RANS but with more accuracy while being faster and less accurate than DNS. DES, Detached Eddy Simulation, is like LES a halfway measure but between LES and RANS.

To summarize turbulent flows, show a range of vortices cascading from large to small and simulating them is critical for an accurate representation of fluid flow. Simulating them however is computationally expensive depending on the amount of fidelity required and technique used.

2.1.3 Numerical Method and Discretization

Having established the mathematical model for fluid dynamics we now need to identify a numerical model or process by which to solve the system of partial differential equations (PDE) of conservation of mass, momentum, and energy.

Having determined the control volume in which the simulation will take place, we need to establish exactly how the discretization of the volume space will take place. The discretization translates the mass equations, or continuous equations, to the computer using a discrete set of points in the control volume. This discretization, linked to the mesh, is what defines the connectivity of all these points. The connectivity of these points forms cells, or elements, for which there are two main ones, see Figure 2.6. The mesh and points form the elements in the control volume in which mass, momentum, and energy of fluids are described may then be calculated when provided with initial conditions. An important thing to keep in mind is poor discretization, or mesh, can lead to numerical instability and may cause the model to blow up. For this reason, there are two types of meshes that we must consider, structured and unstructured. While each has its advantages, in general, structured is good for 'non-complex' geometry and unstructured is good with geometry with arcs. The type of mesh selected will impact the solving of the PDEs and can lead to faster or slower CFD run time.

Because the scoop consists of arcs, we will be using unstructured mesh and the Finite Volume Method (FVM) which is used for unstructured mesh. To mitigate the possibility of numerical instability, and because we are dealing with high-speed flows, a small-time step of 1e-6 seconds or less must be used. Time-step, δt, is an initial condition required for solving Navier Stokes.
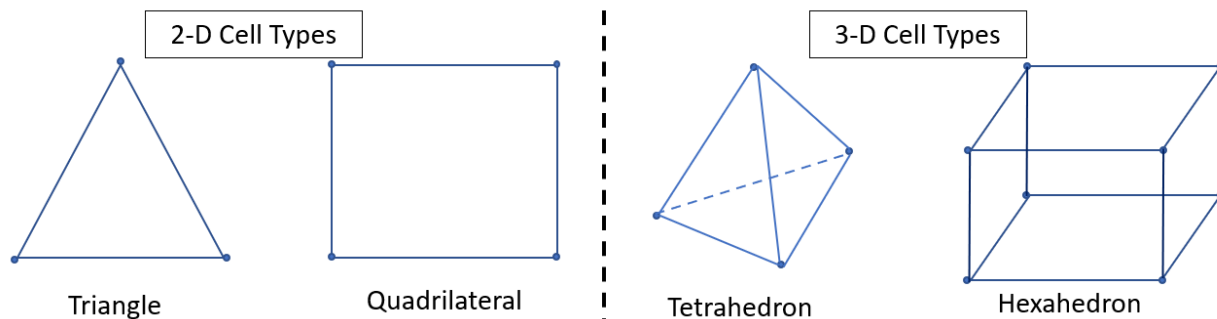
Figure 2.6 Cell types for 2-D and 3-D spaces

Once discretization and mathematical system of equations describing the physics are determined we still need a numerical scheme or algorithm to solve for said equations from initial conditions. In this study the two numerical schemes were used, SIMPLE and PISO.

2.1.4 Post-Processing Analysis

Once the software finishes running the model, we must analyze our results and determine if they are appropriate, or if they fall within expectations. For post-processing we can produce contours that provide information of the entire control volume. This information includes velocity vectors, volume fraction, pressure magnitudes, and more.

2.2 MACHINE LEARNING

As computational power has increased, it has been accompanied by a wide range of new applications. With the increase in computational capability, previously unfeasible tools and methods have reemerged to take advantage of this rise. Among these are more complex Machine Learning (ML) techniques. Machine learning is the science of a computer learning from data [29]. By harnessing computational power and coupling with the capability to learn from data, tasks can become automated, and productivity increased.

Uses of ML can range from email spam filters, language translation, voice recognition, to image recognition, to more advanced uses that can take advantage of unsupervised learning.

2.2.1 Neural Networks

Neural networks (NN) in machine learning are inspired from our brain's architecture. In a similar fashion to birds inspiring flight through planes and planes achieving flight differently to birds, NN have developed differently that than its biological inspiration. It is in this difference however that they become versatile, powerful, and scalable with the capability for large and

complex tasks such as classifying billions of images, speech recognition, video recommendation on YouTube, and even beating the best Chess players in the world.

Neural networks are composed of layers of nodes that are connected to each other. From layer to layer they then create weights from the inputs being provided. Using inputs and an activation function, NN are able to produce outputs. These activation functions are usually nonlinear functions such as the commonly used sigmoid function or Rectified Linear Unit (ReLu), see Figure 2.8. The activation function is used by passing the summation of the inputs by their respective weights and a bias into the function. The output is denoted by h in Figure 2.8. In the equation
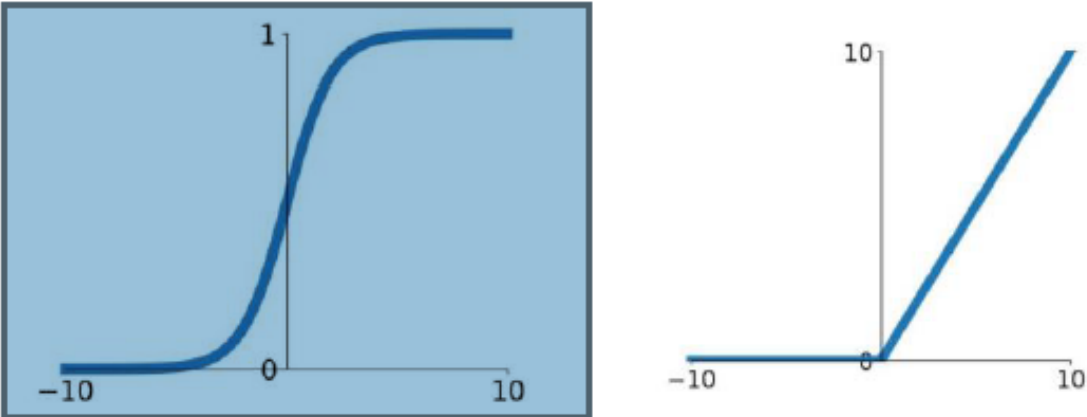
Figure 2.7 – Sigmoid function (left) and ReLu Function (right)

below, (2.22), we can also see the weight denoted by w for each input. Figure 2.9 represents the NN node for the equation

A layer in a NN is a group of nodes that share the same inputs and can be seen in Figure 2.9. A series of layers feeding into the next one together makes a NN further explained below.

$$h_1 = f(x_1 w, +x_2 w_2 + x_3 w_3 + b) \tag{2.22}$$

16
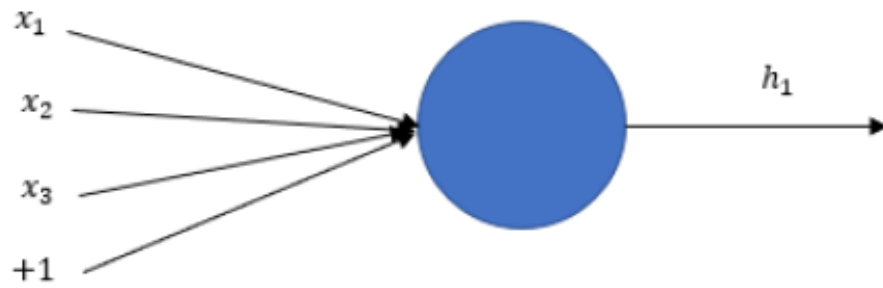
Figure 2.8 – Neural Net Node

Now that a NN node and layer has been established, let us look at a simple NN and break down the components. A simple NN consists of an input layer, hidden layer, and output layer, see Figure 2.10.
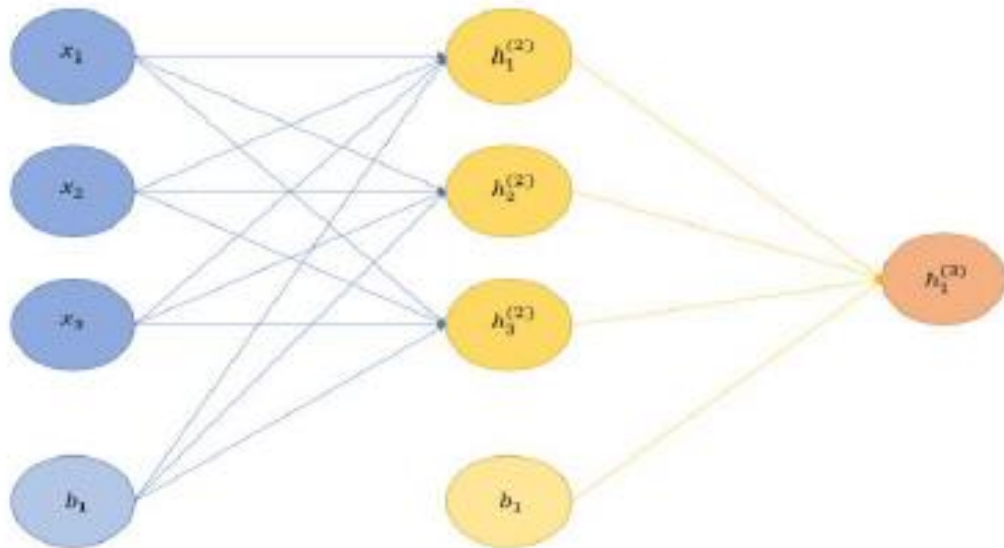
Figure 2.9 – Input layer (blue), Hidden layer (yellow), Output layer (red)

The process by which NN predicts any output is called feedforward, as each layer feeds its output into the next layer an input vector is passed, the weights and biases are applied and then passed into an activation function. This process is repeated for each successive layer until we reach the end. The hidden layers are initialized randomly and are supposed to represent the relationship that a model has determined for obtaining an output. Using both the input and output data, we

17

update the hidden layer weights starting with the last layer and ending with the first layer. This is how the NN learns, this process is referred to as the backward propagation of the loss or error. Backward propagation is using the difference between the model's output and the true output to determine how to update the weights, a previously established method known as gradient descent.

2.2.2 Convolutional Neural Network

Convolutional Neural Networks (CNN) emerged by studying the brain's visual cortex and have been used in a limited capacity since the 1980s [29]. A big limiter of CNNs in the 80s was the absence of today's computational power and data. By studying the brain scientists have come to understand to a certain degree how the human brain processes visual, auditory, and other inputs from our eyes, ears, and other sensors into images, sounds, and other information. A CNN is a specific type of NN that is specialized for pattern recognition.

Through experimental studies during the late 1950s on cats and monkeys, crucial insights of the structure of the visual cortex were derived. The authors of the experiments discovered how neurons in the visual cortex of the brain reacted to visual stimuli located on a small area of the visual field. They noticed that patterns in neurons; some react to horizontal lines, others to different line orientation, some have larger receptive fields, some react to complex patterns that are a combination of other patterns [29]. Those studies inspired neocognition which eventually evolved into convolutional neural networks.

CNNs consist of two types of layers, Convolutional and Pooling Layers. Typical CNN architectures are conceptually simple. They have a few convolutional layers, then a pooling layer, then another few convolutional layers, followed by another pooling layer, and so forth. See Figure 2.10 for a visual representation.

18
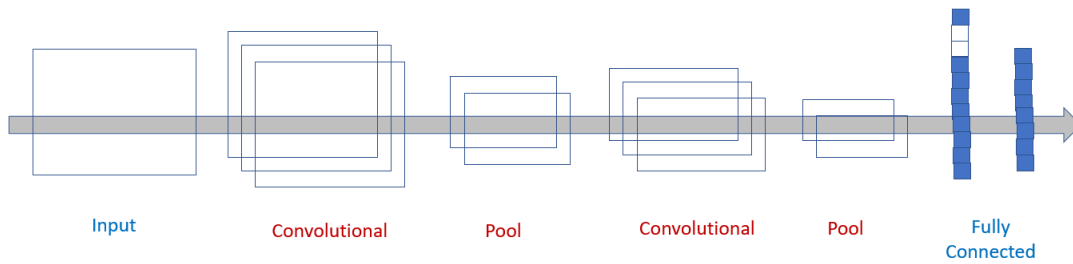
Figure 2.10 - Typical CNN Architecture

The convolutional layers are the most important building block of any CNN. CNNs consist of multiple layers that work in collaboration to improve image recognition. See Figure 2.12.
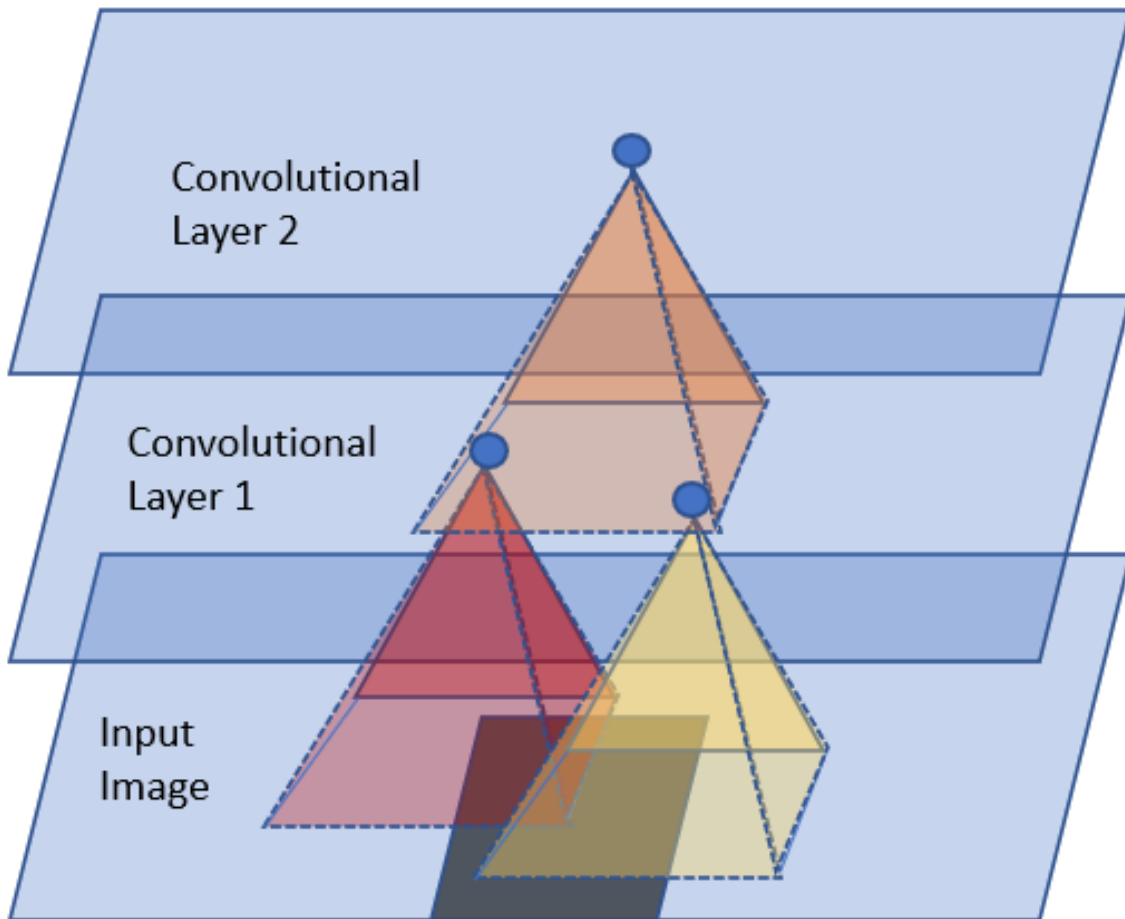
Figure 2.11 – Convolutional Layers

19

Neurons in the first convolutional layer are only connected to their receptive fields and not every pixel in the input image [29]. The second layer on the otherhand is connected only to neurons in a small rectangle of the first. This design allows the neural network to focus on specific low level features in the first layer and then assemble them into higher level features in the next layer, and so forth. This structure is what allows CNNs to work really well for image recognition.

The weight of a neuron can be represented by a small image the size of a receptive field. Figure 2.13 consists of two possible sets of weights, vertical and horizontal. They are also called filters or convolutional kernels.
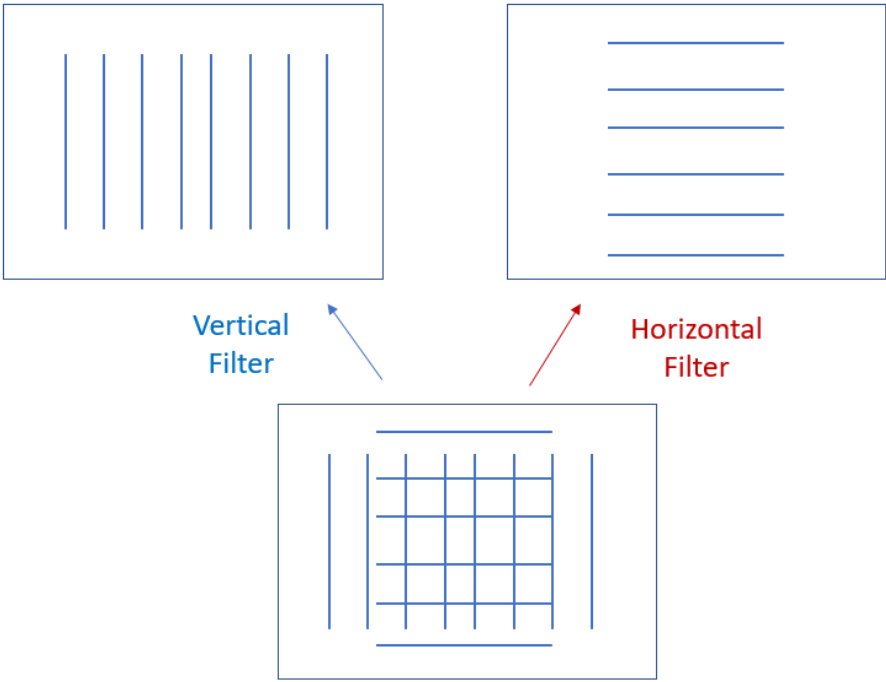
Figure 2.12 – Feature Filters

What the neuron in the filters do is ignore everything in their receptive field (in this case the entire input image) except for the ones they were assigned to (vertical or horizontal). If all neurons are assigned to the vertical filter for example, the outcome would be the top left figure on

Figure 2.13. Vice versa if all are applied to the horizontal filter the outcome would be the top right figure on Figure 2.13.

Having a layer full of neurons using the same filter provides a feature map. A feature map highlights the areas in the image that are very similar to the filter. When a CNN is being trained what the CNN does is to find the most useful filters for its job and combines them into complex patterns. An example would be a cross would be where the vertical and horizontal filter are active.

To understand the concept of convolutional layers only 2D layers have been presented thus far. However, convolutional layers are composed of multiple feature maps of equal sizes [29]. Looking at Figure 2.14 it can be observed that they are more accurately represented in 3D.
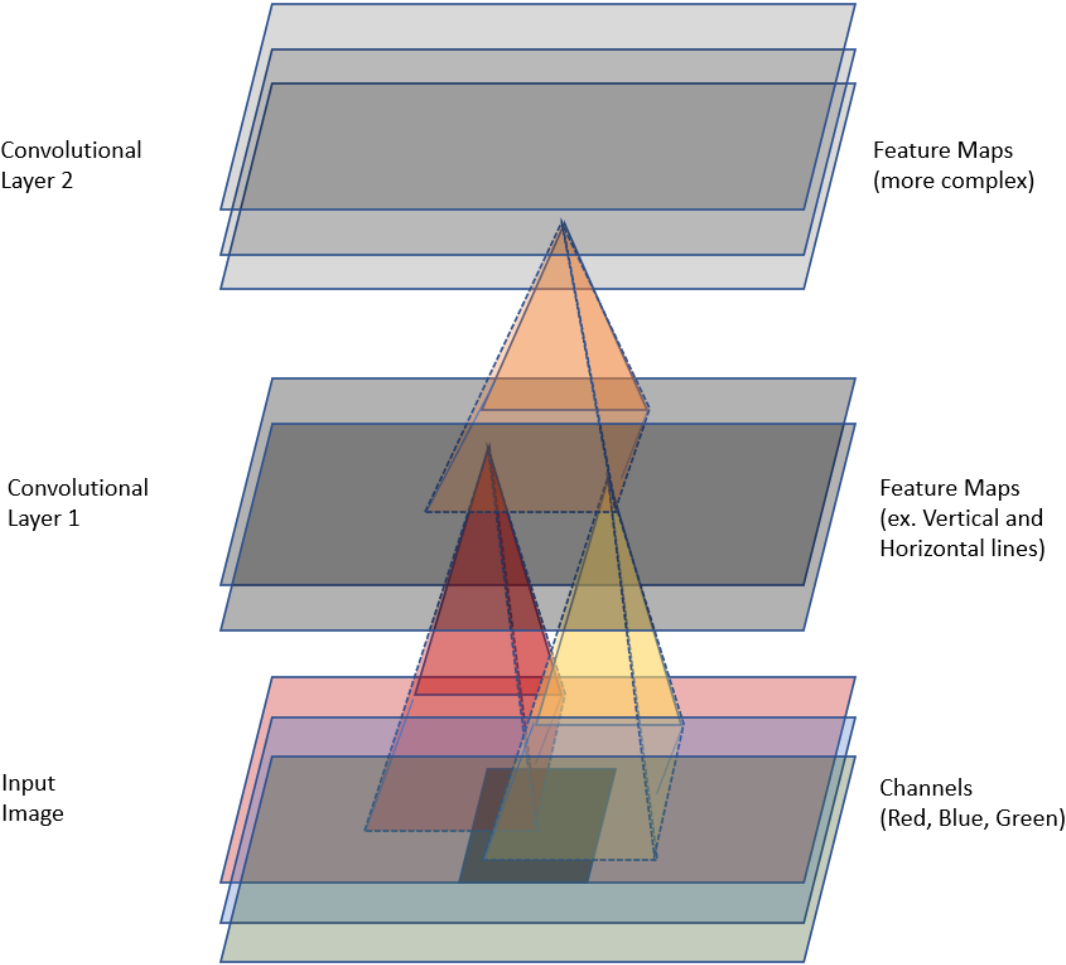
Figure 2.13 – Multiple Feature Maps

Within a single feature map, all neurons share the same parameters, weights, or bias term. When stacked with different feature maps the convolutional layer ends up having different parameters Neuron's receptive field in the layer extends to all previous feature maps [29]. Due to the stacking of multiple feature maps a convolutional layer can simultaneously apply multiple filters to its inputs and therefore making it able to detect multiple features anywhere in the input provided. Furthermore, input images are composed of multiple sublayers. Examples include color channels (red, green, blue or RGB) and satellite images capturing different light frequencies.

A problem with CNNs hinted earlier as the amount of computing power required lies a memory problem. Convolutional layers require a large amount of Random Available Memory (RAM). This is especially true during the training of the CNN "because the reverse pass of backpropagation requires all the intermediate values computed during a forward pass" [29]. When making a prediction for a new instance the RAM occupied by a layer can be released as soon as the next layer is computed. You only need as much RAM as needed by two consecutive layers. The problem is when the CNN needs to be trained, when everything computed during the forward pass needs to be preserved for the reverse pass. The minimum amount of RAM needed is the total amount of RAM needed by all layers. A way to mitigate the memory problem is to reduce the mini-batch size or try removing a few layers. Also, the stride distance between two consecutive receptive fields can be reduced or the bit size of the floats, numbers, can be reduced from 32 to 16. Alternately all can be done.

The pooling layer is the second and final common building block of CNN, the first one being convolutional layer. The goal of the pooling layer is to subsample the input image in order to reduce the computational load, memory used, and number of parameters. Pooling layers can be

quite destructive as even taking a 2x2 kernel with a stride of 2 can result in a loss of 75% of input values.

Like in convolutional layers, neurons in pooling layers are connected to outputs of a limited number of neurons from the previous layer. Unlike a convolutional layer however, it has no weights. All it does is aggregate inputs using an aggregate function, like max or mean. For max only max input values in each kernel make it to the next layer.

Many variants of this architecture have been developed over the years, with increasingly reducing error rates. The advantage of CNN is that all neurons in a feature map sharing the same parameters drastically reduces the number of parameters in the model. This means that for the CNN once it has been trained and it has learned how to recognize a pattern in one location, it can recognize it in any other location.

CNNs are great tools to take advantage of machines computing power and will only become more useful as computing power increases. They will play a big part in future technologies in automation of many systems such as self-driving cars, language recognition, even customer service as it recognizes search patterns and preferences of customers. Although they currently there are a few nuances such as requiring many hyperparameters (number of filters, their height and weight, etc.) and requiring substantial amounts of RAM, their architecture and building blocks are simple to understand. Like any recent technology, however, it will develop and improve as tools are designed to make it easier to design and use. New CNN architectures are being developed every year and the field is moving very rapidly.

2.3 TURBULENCE

Turbulence may be described as a fluid flow phase description that transitions in three phases: laminar, transition, and turbulent. Though it is still a field of intensive study and much is yet to be understood we know that each face undergoes different effects that are important due to impact on the parameters that describe fluid flow. The laminar flow is steady and constant, while flow in transition is chaotic, and finally ends in turbulent flow. The parameters in this study include vorticity, turbulence intensity, turbulent kinetic energy, velocity, and volume fraction. Transition of laminar flow is caused by shear effects build up that cause rotations or eddies in the fluid flow to form, see Figure 2.14.
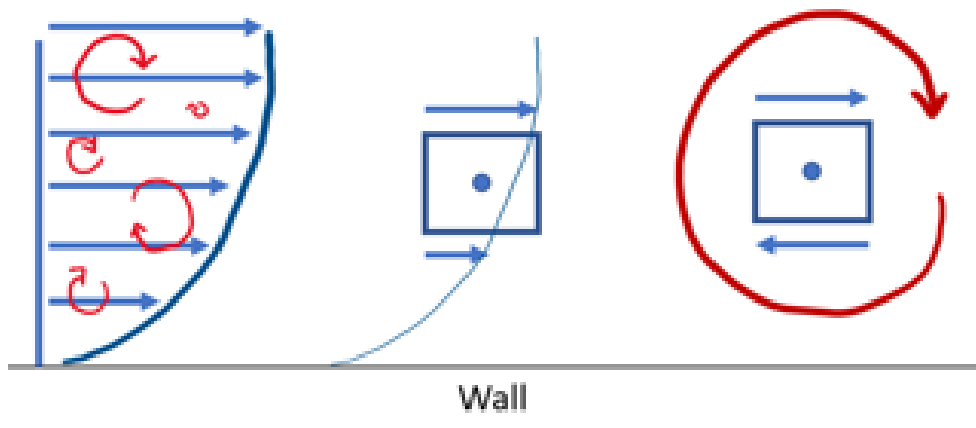
Figure 2.14 – Eddy formation

2.3.1 Turbulence Model

Referencing RANS model that will be used on this model, turbulence effects on it is modeled by K-ε or K-ω models depending on fidelity desired near wall boundaries.

k → turbulent KE
ε → dissipation rate
ω → specific dissipation

K−ε(2 eq)
Solve k and ε to compute for μ_t

$$\mu_t = C_\mu \frac{\rho k^2}{\epsilon} \qquad C_\mu = 0.09$$

K−ω(2 eq)

$$\omega = \frac{\epsilon}{C_\mu k}$$

Chapter 3: Computational Modeling

3.1 INTRODUCTION

The HHSTT at Holloman Air Force Base (HAFB) near Alamogordo, New Mexico, is operated by the 846th Test Squadron (TS). It is the world's premier facility for testing full-scale high-speed flight vehicles conducting cutting-edge Test and Evaluation (T&E) capabilities in support and development of critical weapon systems technology. The HHSTT performs a variety of tests for assessing the performance of various aerospace systems, including bomb and fuse functions, survivability for impact, weapon lethality, ejection seat performance, guidance system accuracy, material erosion, ablation, rain effects on the survivability of aerospace materials, aerodynamic characteristics of aerospace system designs, and others [1–3]. It has been used for conducting hypersonic (beyond Mach 8) [2,4–8] impact tests using rocket-propelled sleds that ran on a 9.63 miles steel rail track in the past. The rocket sleds are held on the rails by steel shoes/slippers [9,10].

The operational flight speed conditions are achieved by using rail-mounted rocket-propelled sleds. The sleds consist of a forebody component, where the braking system and tested item sit, and a pusher component that accelerates the forebody to desired velocity. Because many tests require recovery of the test item for post-test analysis, braking mechanisms with enough braking capability to bring the sled to a stop are required. Braking methods to stop/recover the sleds include curving the track, water braking, spoilers as air brakes, or hooks and cables [11]. There are several methods for deploying water braking depending on testing velocity profiles. Depending on velocity requirements the sled will be propelled in either dual rail or monorail, affecting how water braking is conducted. For dual-rail pusher sleds [2,12,13], water is deployed in a trough between the rails at increasing depths. Water depth is controlled using frangible dams

that are inserted into the channel at planned locations and distances. The sled braking scoop encounters and diverts the water in the trough and provides a drag force that consequently slows down the sled to a stop.

In the last decades, CFD simulations tools have experienced increased development and have become a powerful tool for the analysis and understanding of fluid dynamics phenomena. Due to increased CFD tools development, the designs of AF systems like the high-speed sleds at HHSTT can be improved. The increased capability of CFD tools is made possible by the advent of faster and faster supercomputers with increasing memory capabilities and advanced computing algorithms. It is important to note however that even with all the advances, CFD tools still have potential downsides. CFD results are strongly affected by the numerical methodology employed (i.e., accuracy, efficiency, geometrical modeling, etc.) and computer resources for real-life problems. The limitations of CFD need to be addressed due to the lack of understanding and/or inappropriate physical modeling as well as limited experimental information. The credibility of CFD simulations can only be established by a rigorous process of verification and validation [14–17]. Over several decades, the HHSTT has conducted several high-speed sled tests with water braking mechanisms and collected data of predicted profiles with varying degrees of success, confidence, and fidelity. This, along with tremendous knowledge built around the braking mechanism, would provide a rich dataset for the team to perform validations of predicted CFD results with a high degree of confidence. We follow the established guidelines for assessing the credibility of the CFD Modeling and Simulation results [14,18,19]. The geometry, computational domain, boundary conditions for the numerical simulations in three dimensions are presented in Problem Definition, Section 3.2. Section 3.3 dives into two-dimensional and three-dimensional results, analysis, and discussion of dual rail water braking, followed by section 3.4 which is a conclusion and final comparative analysis between all different designs.

3.2 PROBLEM DEFINITION

To begin, we must define our area or control volume space with the braking scoop and trough inside. This will allow us to set up the space in which we will be able to computationally discretize and simulate the multiphase flow interaction with our brake, in this case the scoop attached to the pusher component of the sled. Specific conditions in 2-D and 3-D designs will be provided in their respective design sections to follow.

A two-dimensional conceptual representation of the problem set up can be viewed in Figure 3.1. We have air and water inlet moving from left to right while scoop geometry remains static and centralized in the domain. By controlling the inlet velocity of air and water we can simulate scoop velocity relative to fluid flow therefore modeling our desired conditions. In Figure 3.2 we can see the discretization and focus of the scoop in Figure 3.1. Discretization around scoop, Figure 3.2, will be comprised of finer mesh to capture with greater detail parameters on and around the scoop.
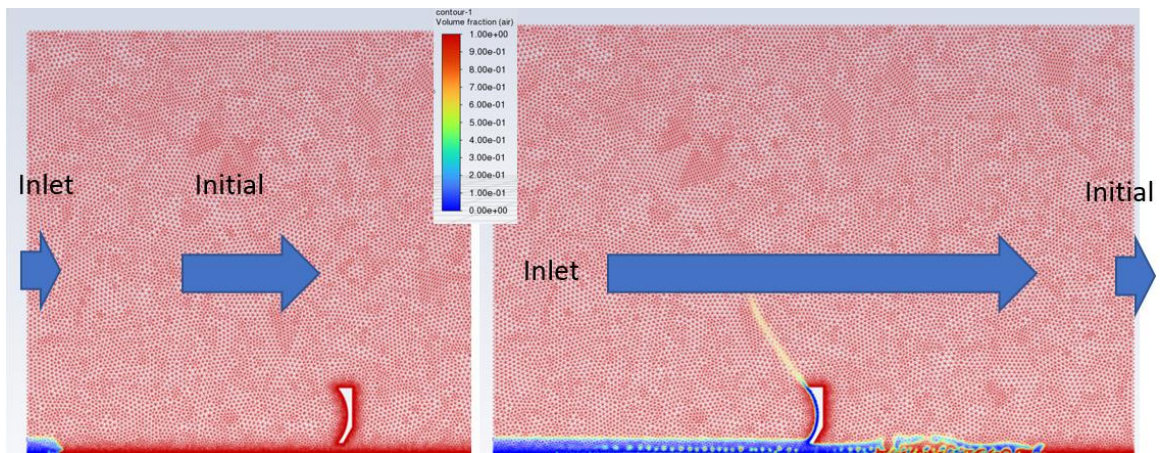
Figure 3.1: 2-D model initial conditions
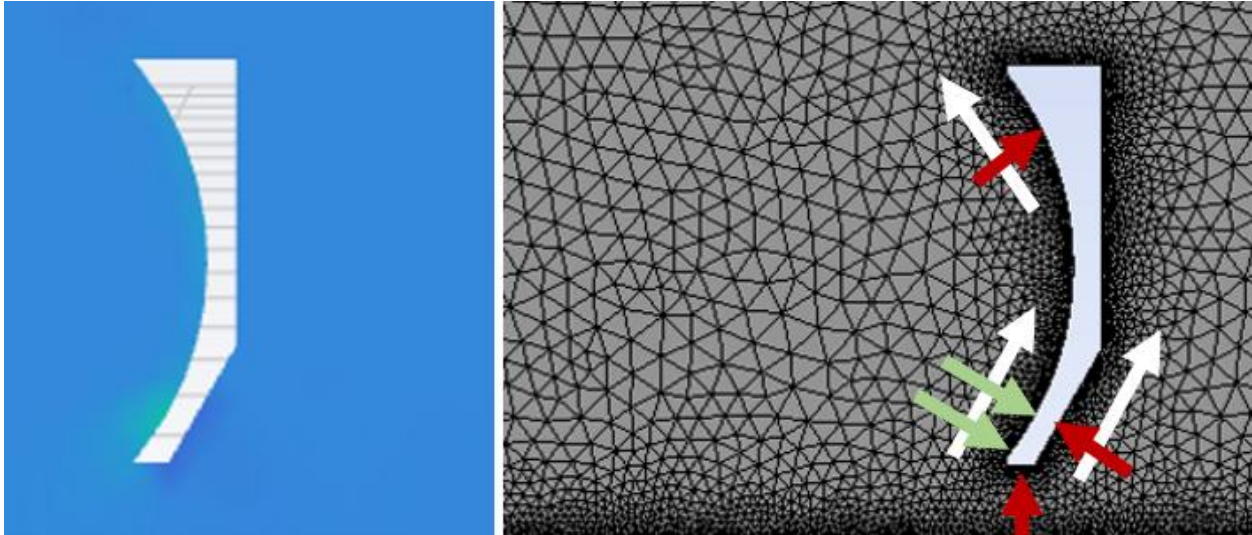
Figure 3.2: (Left) 2-D contour of Design.6 scoop. (Right) Discretization around scoop and expected forces

For the three-dimensional set up the concept and boundary conditions for all models can be understood from Figure 3.3 and Figure 3.4. In Figure 3.3 we have boundary conditions with water and air inlet from the left, pressure outlet from the right, and walls for top, bottom, and scoop. The difference between all the models are geometric changes to the scoop, all other conditions were kept the same. The turbulence model used for all was, k-epsilon 2 equation RANS model, with a SIMPLE numerical scheme.
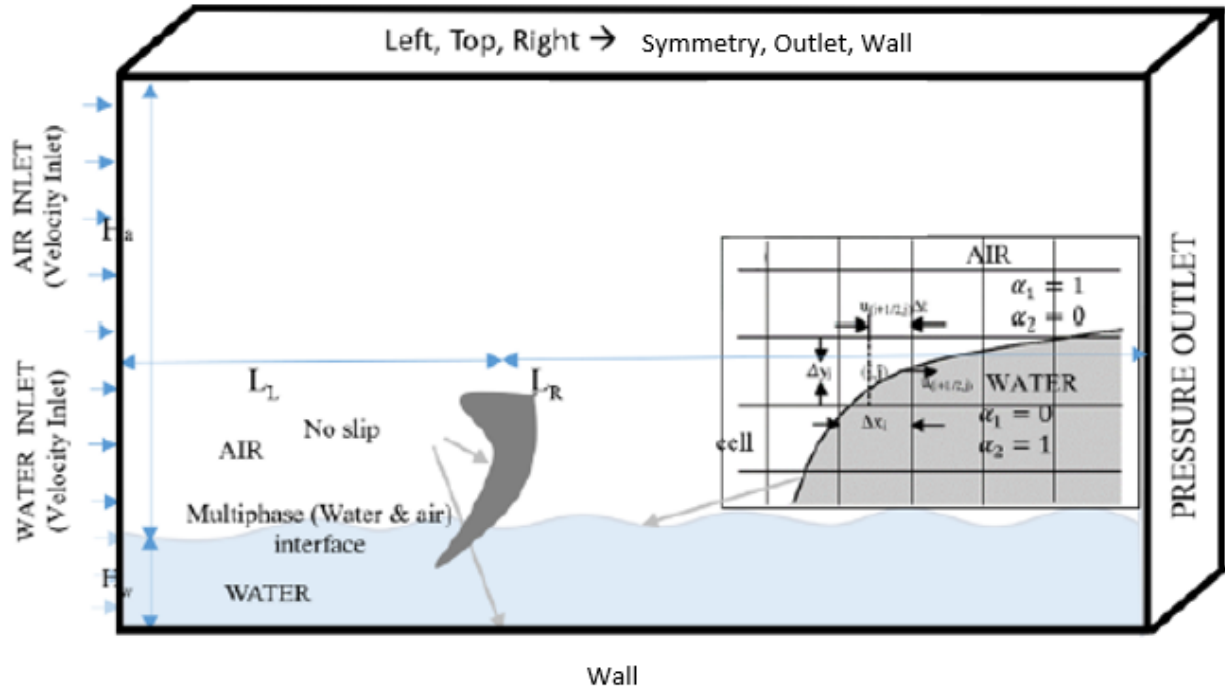
Figure 3.3: 3-D boundary conditions and set-up
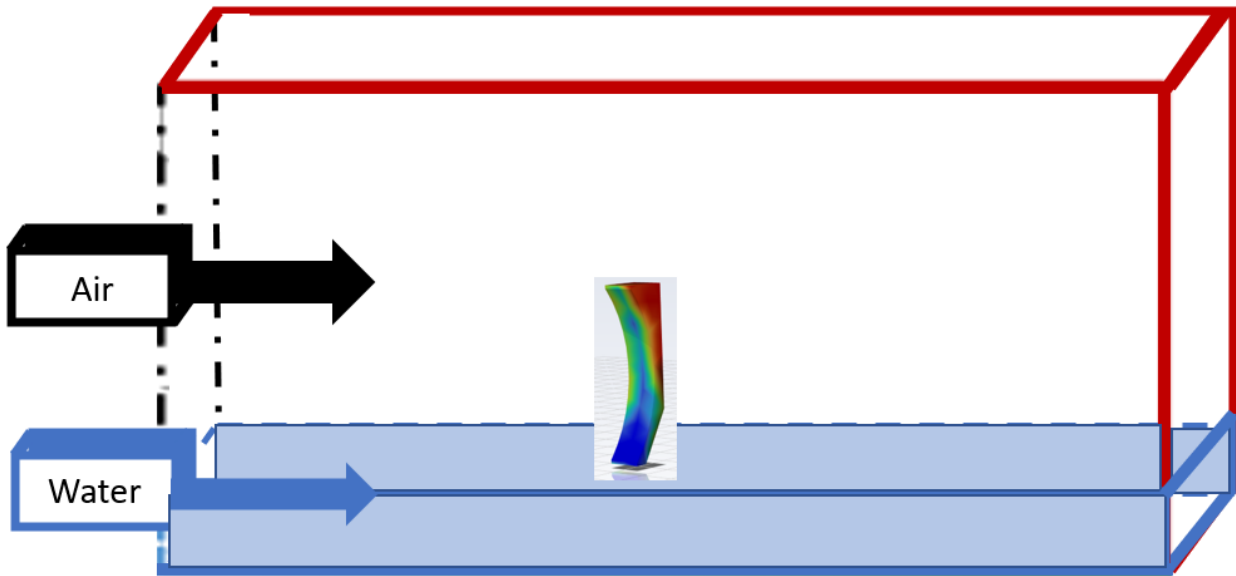
Figure 3.4: 3-D Multi-phase flow domain initial conditions

Data analyzed from each simulation was pressure, volume fraction, velocity, vorticity, turbulent kinetic energy, turbulent intensity, and volumetric flow rate.

29

3.3 METHODOLOGY

Analysis of scoop simulations began with 2-D case in which study of conditions and solvers were studied before proceeding to 3-D cases. The purpose was to get acquainted with the simulation of the scoop and ANSYS CFD software suit, Fluent, before doing much more time consuming and computationally expensive 3-D models. This section is partitioned into 2-D and 3-D modeling. Each partition consists of its own geometric, discretization statistics, and analysis of results sections unique to each scoop design. Consistency in mesh quality, domain, turbulence model, numerical scheme, and transient specifications was sustained in order to be able to make valid comparisons between the different geometries. Explicit solver was used to control the time step and produce structured and consistent data for the eventual neural network that will be trained on the data, greater control of residuals. An implicit solver though it would help model complete faster, it may lead to inconsistency in the data, good for speed but not necessarily accuracy.

3.3.1 2-D Modeling

The initial scoop design in 2-D is inspired in channeling water flow through the scoop while providing a 60 degree divergent geometry behind the bottom of the scoop to reduce the lift force caused from water flowing under the scoop, see Figure 3.5.
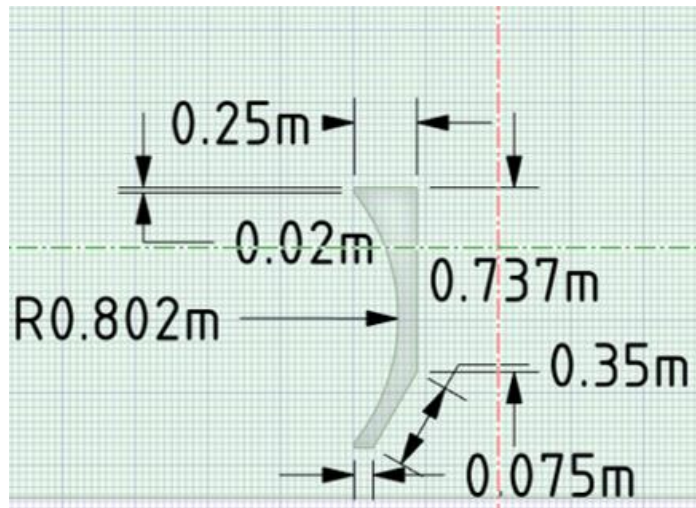
Figure 3.5: 2-D Design.6 Scoop geometric dimension

The discretization of the 2-D model was focused mainly on greater fidelity around the scoop and water channel as most of the force will be coming from the water, see Figure 3.6.
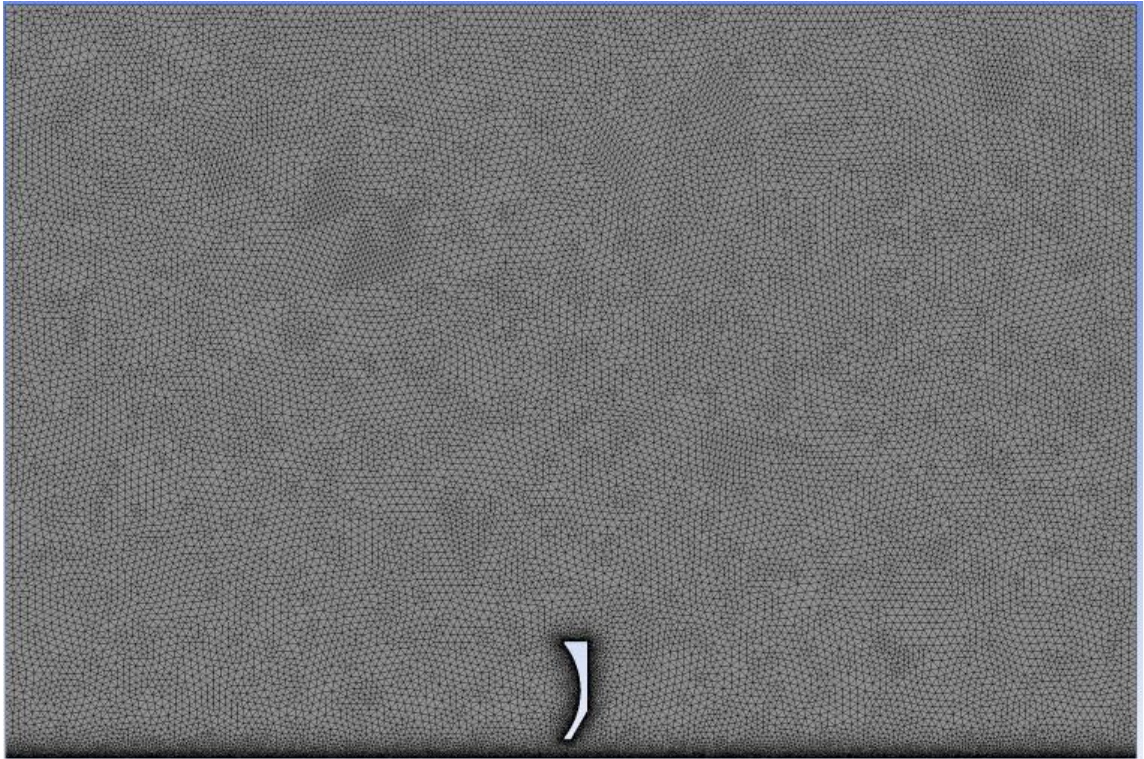
Figure 3.6: 2-D Design.6 mesh

(2-D models are geometrically 8 meters by 12 meters.) Element quality was very high with the average being 0.96229 insuring quality results. Element quality is a dimensionless unit that ranges from 0 to 1 and represents a perfect element. An issue with element quality however, specifically with complex geometries and unstructured meshes, is the minimum quality of an element. Due to some small geometric details, it can be difficult to obtain an acceptable lowest minimum quality element. Having even a few poor elements can be detrimental to a simulation and lead to numerical instability that keeps simulation from converging and reaching steady state. Details of the geometry such as lengths of all the sides and element quality are in Table 3.1.

Though a mesh dependency wasn't completed, it is important to keep in mind for future studies and heading into more complex and computationally expensive models for optimization and accuracy purposes. Of particular focus and caution to consider should be the mesh around the scoop as high speed flow will travel through multiple elements in one time step. Caution should be exercised for mesh structure and size. If mesh is not fine enough it'll fail to capture turbulent effects and its impact across different parameters, too fine however and model will take much longer to run.

Table 3.1: 2-D Design.6 Geometric domain

Bounding Box		Quality	
Length X	12. m	Check Mesh Quality	Yes, Errors
Length Y	8. m	Target Skewness	Default (0.9)
Length Z	0. m	Smoothing	High
Properties		Mesh Metric	Element Quality
Volume	0. m³	Min	2.9503e-002
Centroid X	6.0004 m	Max	1.
Centroid Y	4.0038 m		
Centroid Z	0. m	Average	0.96229
Surface Area(approx.)	95.878 m²	Standard Deviation	3.7793e-002

Object Name	water_inlet	air_inlet	top.bottom_wall	back_outlet	scoop_front.bottom_wall	scoop_walls
State	Fully Defined					
Scope						
Scoping Method	Geometry Selection					
Geometry	1 Edge		2 Edges	1 Edge		6 Edges
Definition						
Send to Solver	Yes					
Protected	Program Controlled					
Visible	Yes					
Program Controlled Inflation	Exclude					
Statistics						
Type	Manual					
Total Selection	1 Edge		2 Edges	1 Edge		6 Edges
Length	0.3 m	7.7 m	23.999 m	8. m	2.e-002 m	2.5117 m
Suppressed	0					
Used by Mesh Worksheet	No					

3.3.1.4 Results

Qualitative results in line with what is expected from initial air flow on the scoop seen in Figure 3.7. Figure 3.7 is in a contour of the Mach Number and density of the air that the scoop

experiences contact with the water early in the simulation. Later in the simulation after water contact the drag force captured a force of 8.79E6 N at inlet velocity of 300m/s, see Plot 3.1. As seen in Plot 3.1, force seems consistent and may hence reached a degree of steady state from which analysis of the fluid flow can be done. Plot 3.2 is a quantitative representation velocity magnitude as a mixture of both air and water.
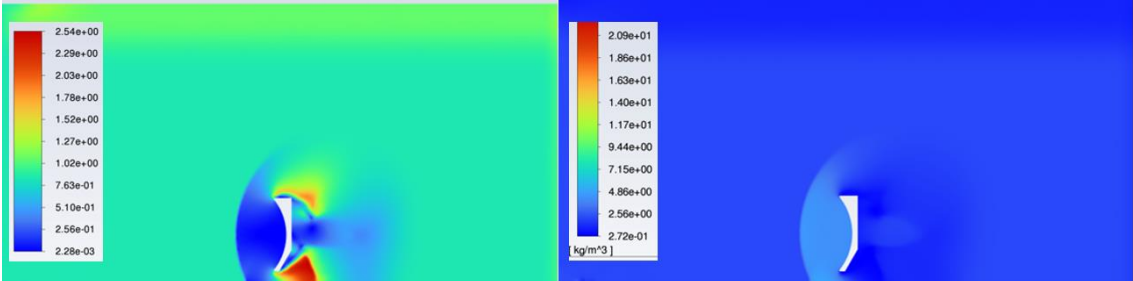
Figure 3.7: Mach number (left) and density of air (right) of 2-D Design.6 at 300 m/s
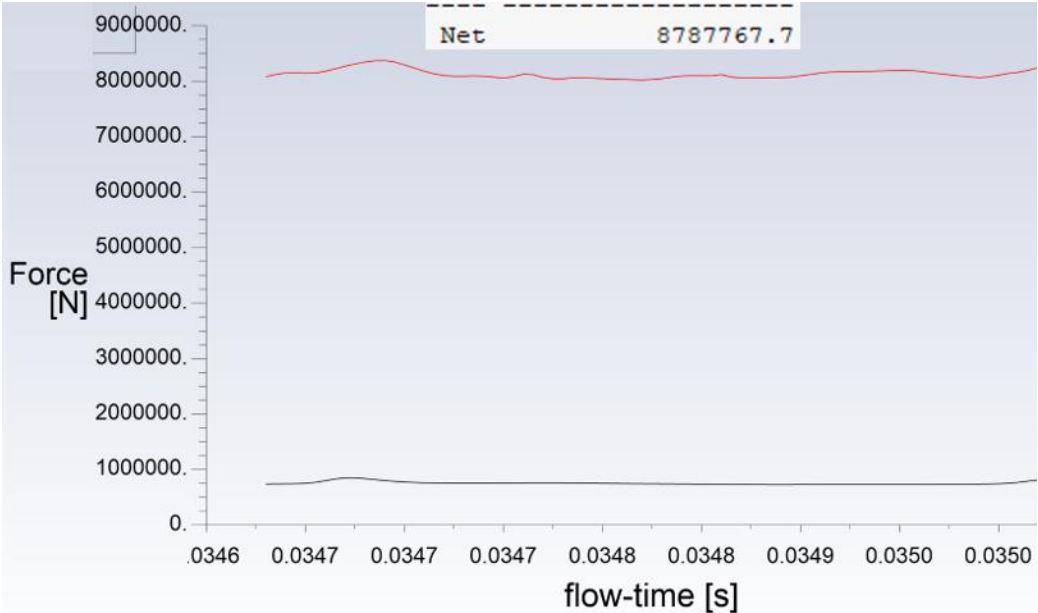
Plot 3.1: Force of Design.6 at 300m/s
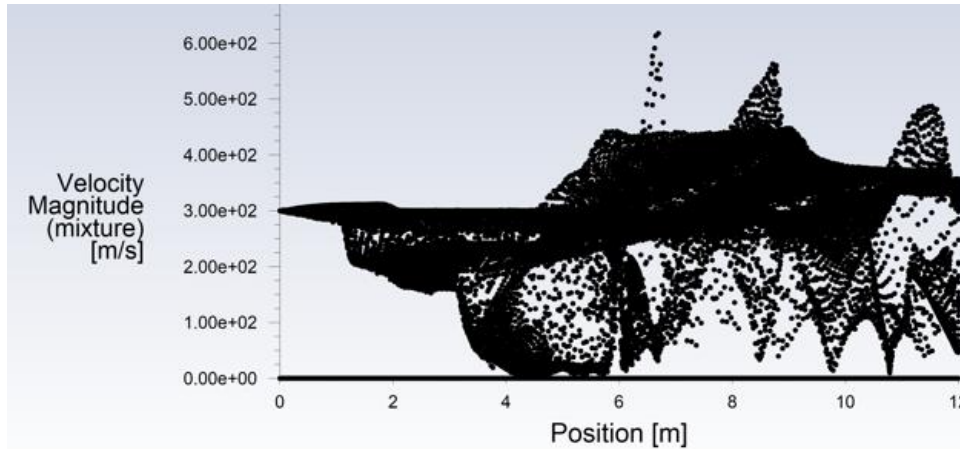
Plot 3.2: Velocity Magnitude of Design.6 at 300m/s

3.3.1.5 Verification

The 2D model in Figure 3.1, illustrates the control volume (domain) and fluid flow. 2D model was run with a 300m/s velocity inlet for both air and water inlet. As previously stated, the purpose of the 2D model was to establish initial conditions and boundary conditions. Using Figure 3.5, calculations by hand can be estimated at 300 m/s and compared to software simulation to validate. Results are shown below.

Force (by hand) = 9.0e6 N/m   Force (2D model) = 8.7e6 N/m

3.3.1.6 Conclusion

2-D modeling though important for establishing initial conditions, boundary conditions, and developing competence in ANSYS Fluent, has little utility from an analysis standpoint of a real-world condition. Being 2-D means it lacks depth in which water and air can also flow to, therefore changing the calculus of scoop geometric studies. Essentially a 2-D model may be viewed as a geometry that potentially has infinite depth.

34

3.3.2 3-D Modeling

The first step after 2-D modeling was to determine using different geometric changes from a 3-D version of the 2-D model. In total there were five different geometric variations including the 3-D adaptation of the 2-D scoop just analyzed in 2-D modeling section. The 2-D 3-D adaptation is known as Design.6. All geometries have single small changes from each other starting with Design.6. From Design.6 to Design.7 for example, "guards" were added to the sides of the front of the scoop to channel water in the scoop. In Figure 3.8, all five different variations are illustrated. Green demonstrates the addition from previous design while red is removal of a certain geometric distinction. Figure 3.9 shows front and side view of all scoop designs without pointing out geometric differences like in Figure 3.8. Combining Figure 3.9 and Figure 3.10 a clearer individual picture of the different scoop designs can be observed.
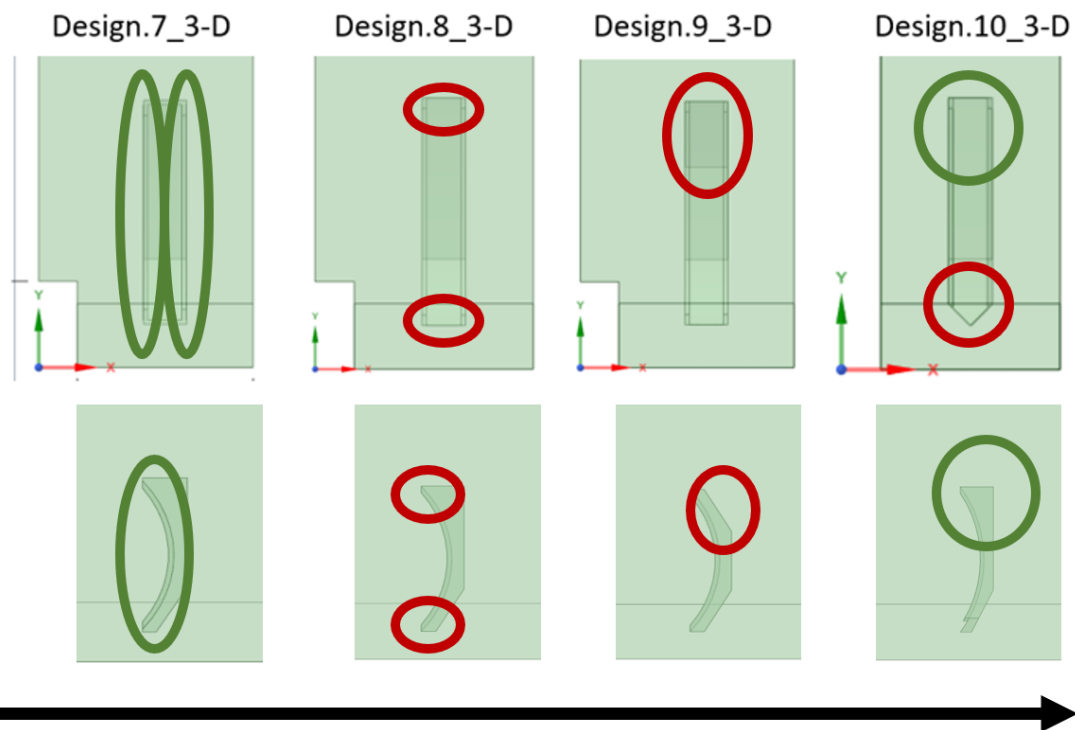
Figure 3.8: Variations between the different 3-D scoop designs. Green marks indicate additions and red indicate subtractions.
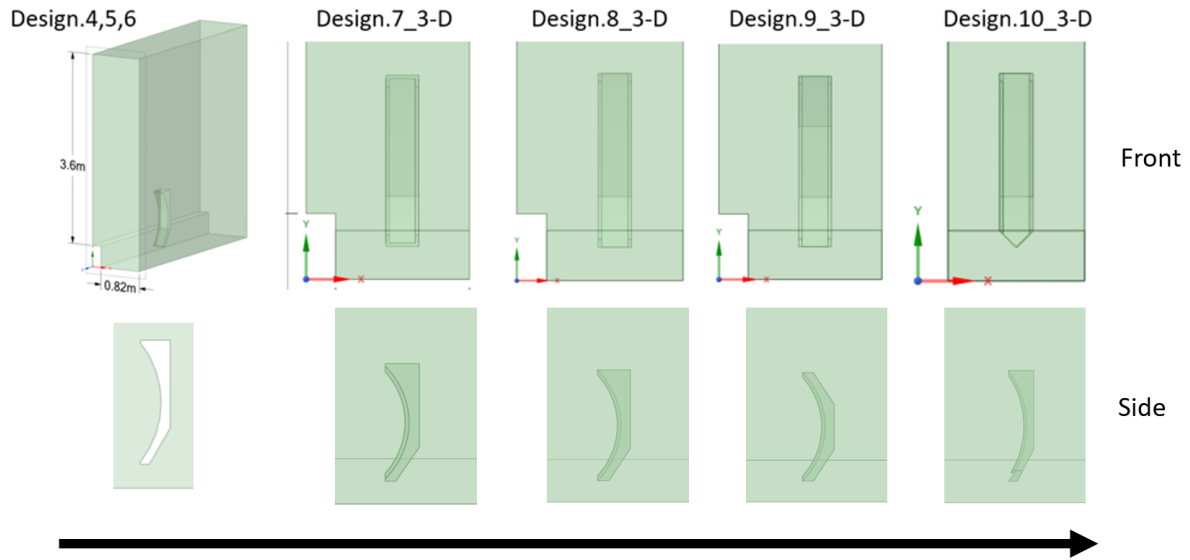
Geometries of each design after changes

Figure 3.9: All the different scoop designs front and side views.
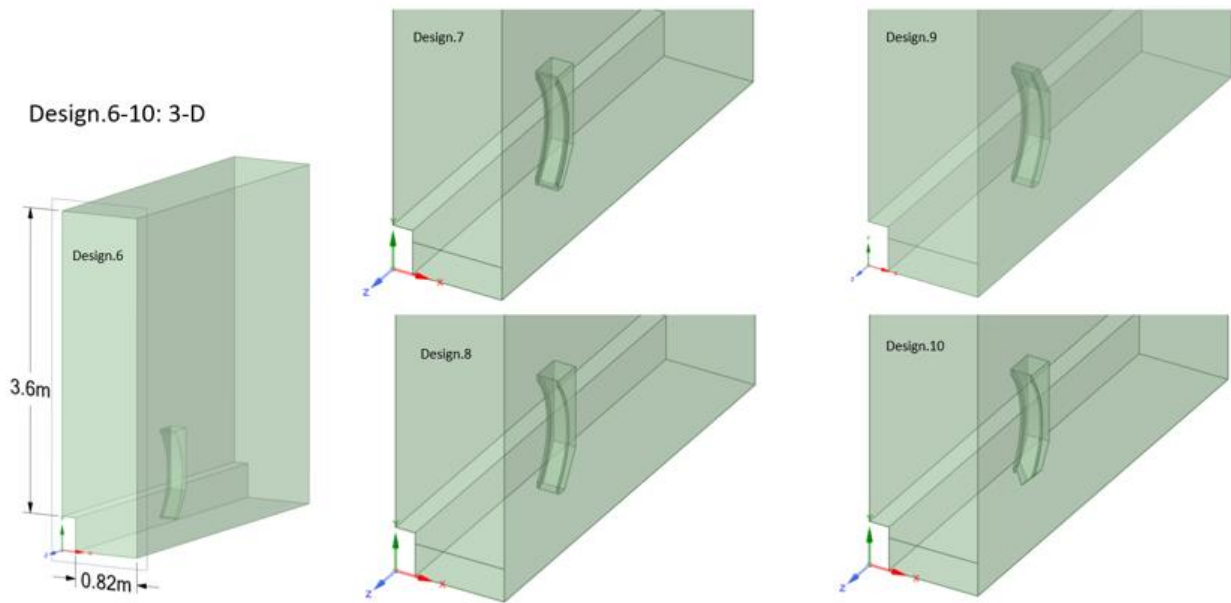
Figure 3.10: All the different scoop designs isometric view.

Figure 3.11 illustrates different meshes that were attempted for the 3-D models. Since consistency was important mesh cell geometry and statistics had to be as close as possible.
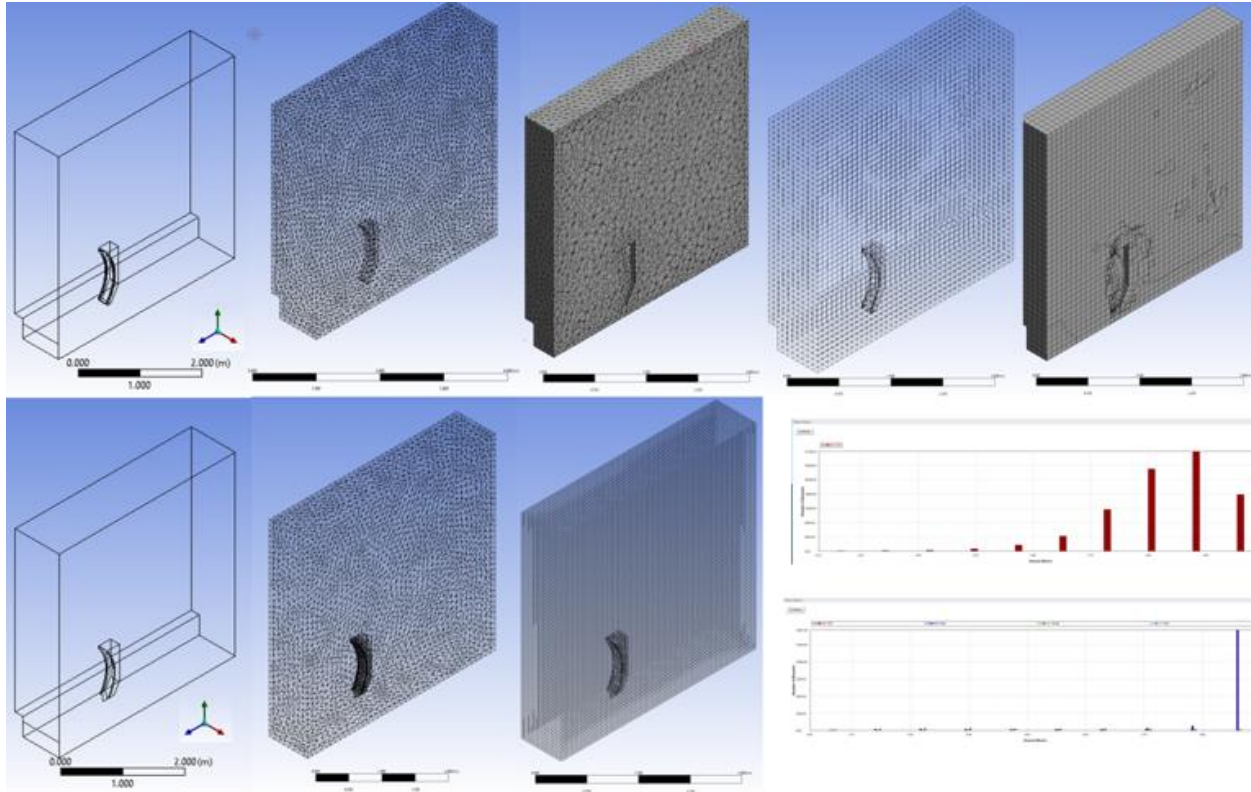
Figure 3.11: Mesh of different 3-D designs and their mesh quality (bottom right)

To that end, the same type of cell topology, tetrahedrons, were used as well as effort to obtain a similar quality of the mesh was made. Geometric differences meant that it was impossible to have the same mesh statistics, but they were all within 1% difference when it came to the number of elements. The specified element size was the same for all. When creating the 3-D mesh from Hexahedrons, seen in top right of Figure 3.11, they did produce higher quality mesh, but the lower quality elements were too low and caused numerical instability that would prevent the simulation from converging.

All five scoop designs, starting with Design.6, were simulated at 100 m/s. Any faster flow was difficult to converge with mesh limitations due to computational resource limitations. Only Design.9 was also modeled successfully to an extent at 300 m/s. The following sections of 3-D modeling go into the details of the results for each design. Qualitative data in the contours to follow are extracted from a plane going across the domain in the Z-axis.

3.3.2.1 Design.6 at 100 m/s

Design.6 is the first to be modeled in 3-D for the purposes of this study, it is a direct model from the 2-D scoop but with a 0.2-meter depth.
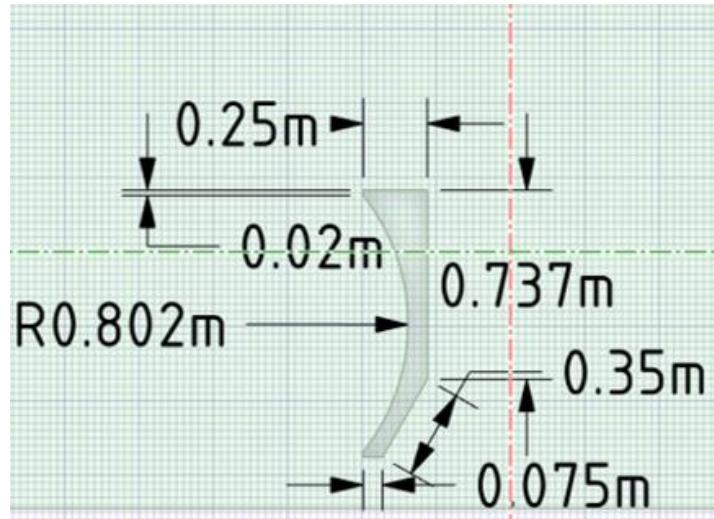
Figure 3.12: Dimensions of the original scoop (Design.6), from which all others originate from.

The dimensions of Design.6 can be seen in Figure 3.12 while the depth of 0.2 meters can be seen in Table 3. 2. Table 3.2 in addition shows the 3-D volume domain in which the simulation is discretized and modeled. Other important parameters are shown such as number of elements and their quality statistics.

Table 3.2: Statistics of Design.6 mesh

Bounding Box	
Length X	1. m
Length Y	4. m
Length Z	4. m
Properties	
Volume	15.688 m³
Centroid X	0.50739 m
Centroid Y	2.0349 m
Centroid Z	-2.0006 m
Statistics	
Nodes	16737
Elements	84379
Mesh Metric	Element Quality
Min	0.22624
Max	0.9995
Average	0.83465
Standard Deviation	9.6624e-002

38

In Table 3.3 a domain statistical breakdown and sections are specified. These are important because it is the documentation of all the objects in the domain and their breakdown. The object breakdown is important to the analysis as the software requires specification of where to measure the force, for example. These objects are the breakdown as specified by the modeler of the different domains, faces, lines, and points inside of the entire domain being modeled.

Table 3.3: Statistics of Design.6 boundaries

Object Name	air_inlet	water_inlet	walls	back_outlet	scoop_walls
State					
Scoping Method					
Geometry	1 Face		6 Faces	1 Face	4 Faces
Send to Solver					
Protected					
Visible					
Program Controlled Inflation					
Type					
Total Selection	1 Face		6 Faces	1 Face	4 Faces
Surface Area	3.6853 m²	0.24272 m²	40. m²	3.928 m²	0.4272 m²

Object Name	scoop_bottom_walls	scoop_front.mid.arc_wall	scoop_front.bottom_wall	scoop_front.top_wall	scoop_front.arc.mid.sides_walls
State			Fully Defined		
Scope					
Scoping Method			Geometry Selection		
Geometry	2 Faces	3 Faces		1 Face	2 Faces
Definition					
Send to Solver			Yes		
Protected			Program Controlled		
Visible			Yes		
Program Controlled Inflation			Exclude		
Statistics					
Type			Manual		
Total Selection	2 Faces	3 Faces		1 Face	2 Faces
Surface Area	8.5e-002 m²	0.21112 m²		5.987e-003 m²	6.1039e-002 m²

In Figure 3.15, we have the volumetric flow rate of water in front, isometric, and side views. It illustrates how he water specifically is engaging with the scoop and how the water is flowing. Critical to this analysis is the inspiration for geometric changes to attempt to channel water flow in a more productive capacity for our purposes, which is to increase drag.
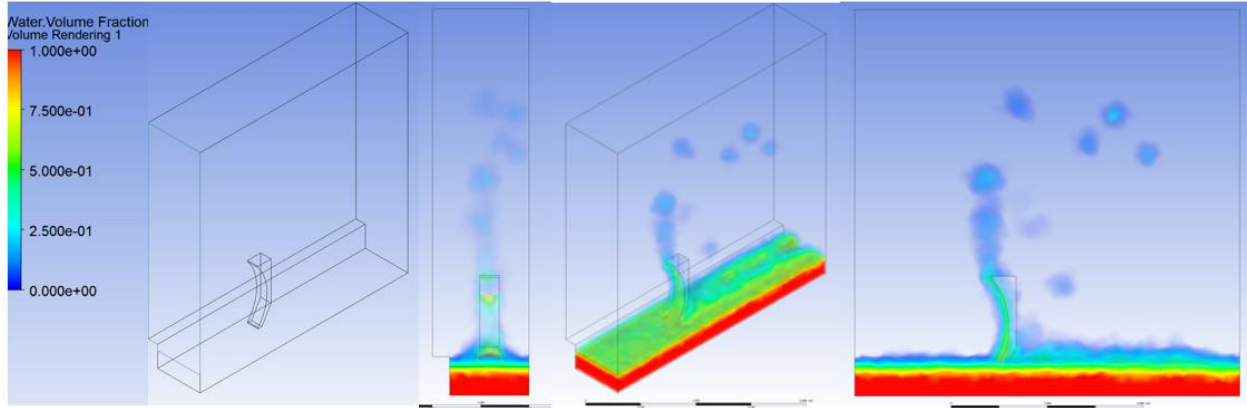
Figure 3.15: Design.6 water volumetric flow rate

In Figure 3.16 we have a quad chart of velocity contours, careful to the interpretation of 3-D results is noticing the orientation of the X, Y, and Z axis. The Z-axis follows the fluid flow direction inversely, but adjustments were made to make them positive in the legend. X axis is the "depth" in the domain and Y axis is the height.

From the velocity quad chart, starting with top left we have magnitude, followed by velocity in Z-axis on the top right, velocity in the X-axis on the bottom left, and finally velocity in the Y-axis on the bottom right. Also, the velocity contours and the pressure are through a plane across the domain, it provides a picture of what is happening around the middle of the domain. As expected, most of the velocity flow is on the Z-axis but there is flow in the X and Y as well that impact overall flow. Pressure is also highly concentrated at the bottom of the scoop where water first engages it.
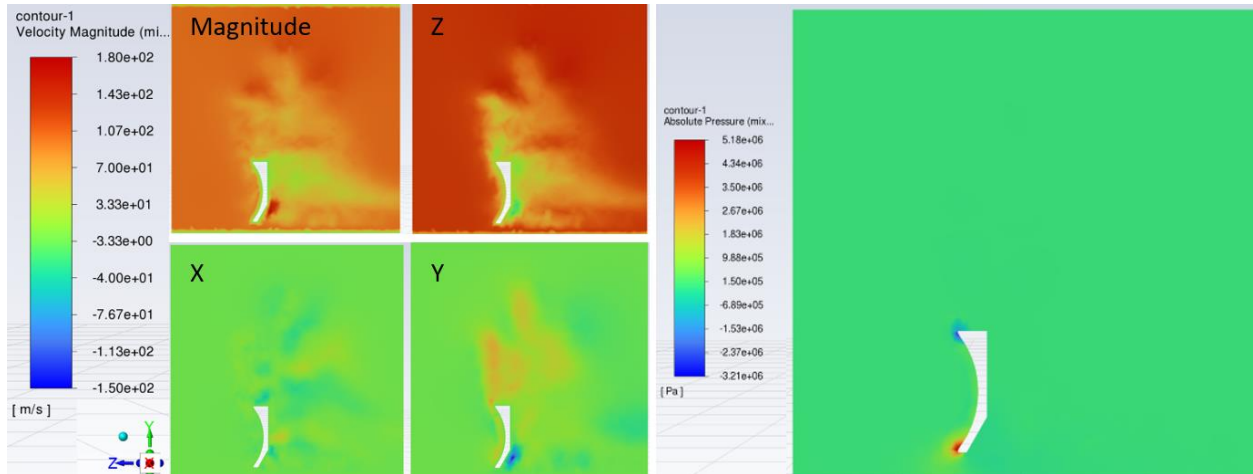
Figure 3.16: Design.6 velocity contours (left) and pressure contour (right)

Turbulent kinetic energy in conjunction with turbulent intensity and vorticity are important in determining amount of turbulence generated and hence drag on the scoop. By viewing the contours, we are able to distinguish where the highest concentration is and make geometric adjustments to improve drag on scoop.
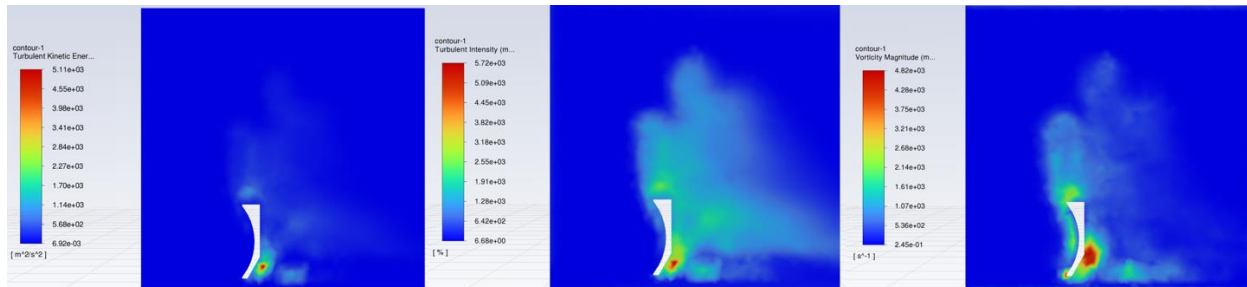
Figure 3.17: Design.6 Turbulent Kinetic Energy (KE) contours (left), Turbulent Intensity contour (center), and Vorticity magnitude contour (right)

The force on our initial 3-D model is 139kN as seen in Plot 3.1. Also, on Plot 3.1 we can see the quantification of the pressure observed in Figure 3.16 and by cross examining them we can distinguish the regions of high pressure and low pressure in the geometry.
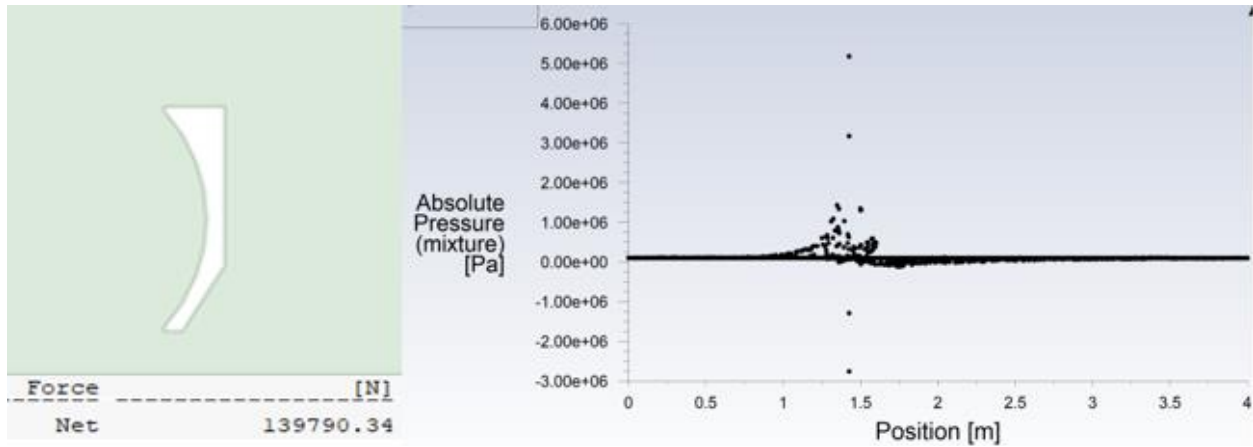
Plot 3.1: Design.6 side view and drag force (left) and absolute pressure plot (right)

Similar to comparing pressure plot with its contour, an analysis of vorticity, velocity, turbulent kinetic energy, and turbulent intensity plots in Plot 3.2 can be made with Figure 3.16 and Figure 3.17. Knowing that the scoop is at the 1.425-meter mark and goes to the 1.675 meter mark we can conclude the peaks in turbulence are occurring past the arc of the scoop and that a lot of the water flow is being lost to the sides of the scoop. Having this information we can proceed to a new design, Design.7.
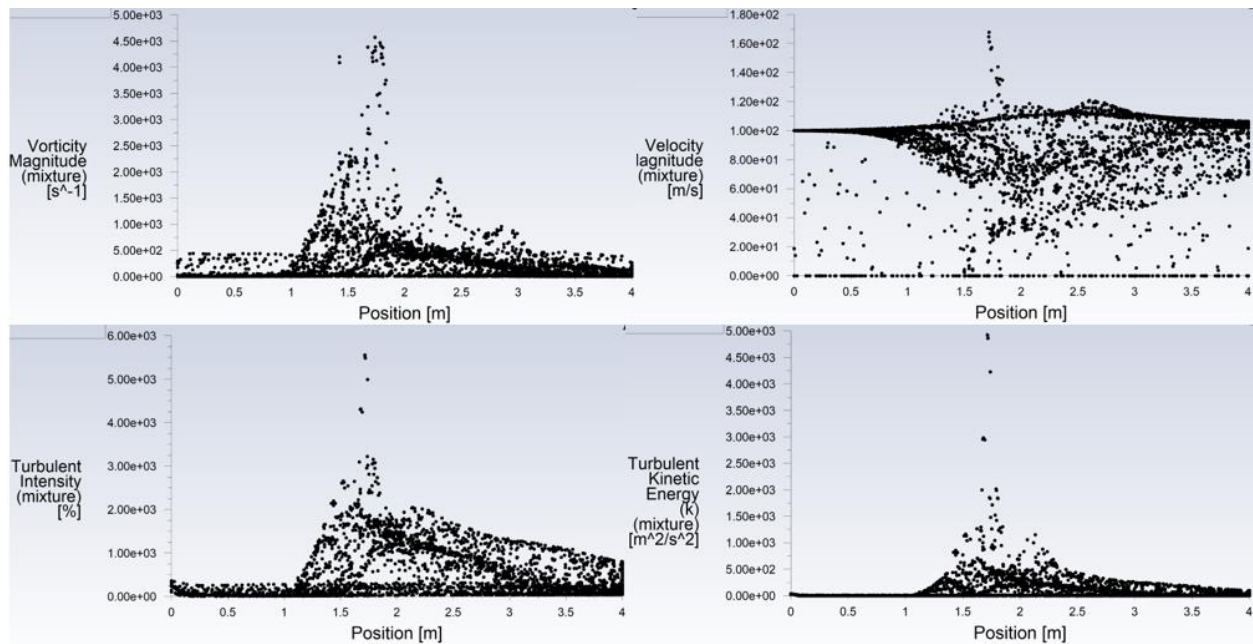
Plot 3.2: Design.6 vorticity magnitude (top left), velocity magnitude (top right), turbulent intensity (bottom left), and turbulent kinetic energy (bottom right)

3.3.2.2 Design.7 at 100 m/s

In Design.7 we can take lessons learned from Design.6 and design into the future, understanding that as contours become part of the analysis they should be standardized into Design.7 and onwards. Proceeding from the analysis conclusion of Design.6, "guard rails" on the front arc of the scoop are integrated to hopefully guide the water flow through the scoop and generate greater drag.

In Figure 3.18 from the green ovals, we can see exactly how these guard rails will be integrated and how thick they will be. The only changes made from Design.6 to Design.7 is 0.3-meter guard rails on both sides of the front arc of the scoop. The scoop retains the small flat surface at the top and bottom of the scoop.

Adding these guard rails, however, introduces greater geometric complexity when it comes to discretizing the volume domain, therefore reducing the quality of the mesh slightly and decreasing the quality of the lowest quality element. For statistics on mesh see Table 3.4
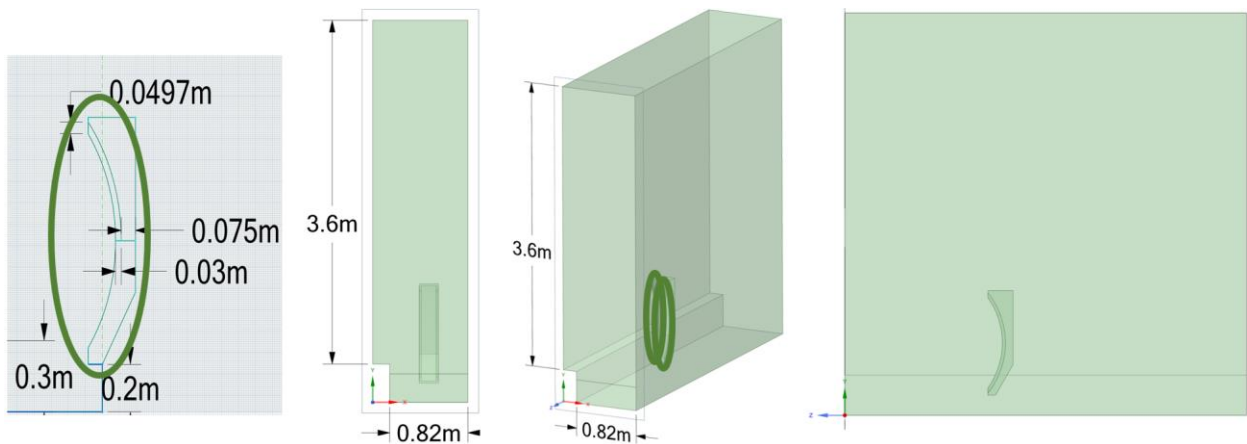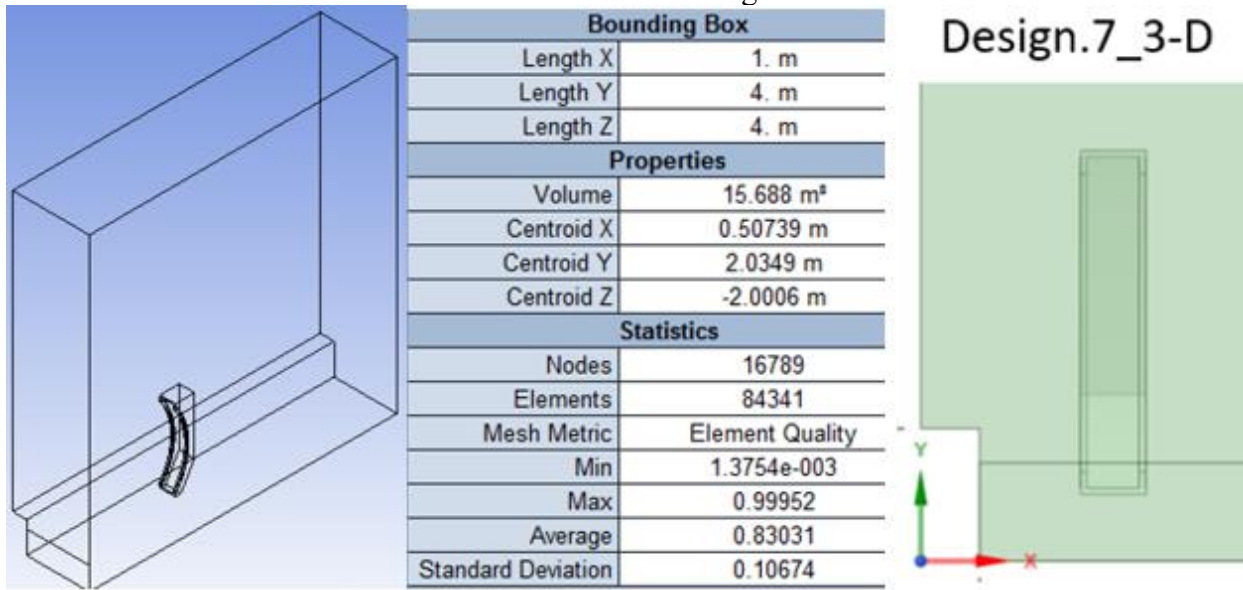
Figure 3.18: Design.7 geometry changes and views from changes made from Design.6

Table 3.4: Statistics of Design.7 mesh

Bounding Box	
Length X	1. m
Length Y	4. m
Length Z	4. m
Properties	
Volume	15.688 m³
Centroid X	0.50739 m
Centroid Y	2.0349 m
Centroid Z	-2.0006 m
Statistics	
Nodes	16789
Elements	84341
Mesh Metric	Element Quality
Min	1.3754e-003
Max	0.99952
Average	0.83031
Standard Deviation	0.10674

Design.7_3-D

Just as in Design.6 identifying important objects is important for analysis, see table 3.5 for breakdown of Design.7 objects in the domain. For the most part just like in Design.6 emphasis is made on the front of the scoop.

Table 3.5: Statistics of Design.7 boundaries

Object Name	air_inlet	water_inlet	walls	back_outlet	scoop_walls
State					
Scoping Method					
Geometry	1 Face	6 Faces	1 Face	4 Faces	
Send to Solver					
Protected					
Visible					
Program Controlled Inflation					
Type					
Total Selection	1 Face	6 Faces	1 Face	4 Faces	
Surface Area	3.6853 m²	0.24272 m²	40. m²	3.928 m²	0.4272 m²

Object Name	scoop_bottom_walls	scoop_front.mid.arc_wall	scoop_front.bottom_wall	scoop_front.top_wall	scoop_front.arc.mid.sides_walls
State		Fully Defined			
Scope					
Scoping Method		Geometry Selection			
Geometry	2 Faces	3 Faces		1 Face	2 Faces
Definition					
Send to Solver		Yes			
Protected		Program Controlled			
Visible		Yes			
Program Controlled Inflation		Exclude			
Statistics					
Type		Manual			
Total Selection	2 Faces	3 Faces		1 Face	2 Faces
Surface Area	8.5e-002 m²	0.21112 m²		5.987e-003 m²	6.1039e-002 m²

Learning from Design.6 for Design.7 data was specifically designed with contour and plot integration in mind. As seen in Figure 3.19, pressure contour and plot are now together and at the same dimensions (plot encompassing the domain range) to better view parameter behavior on the domain plane. As in Design.6 there are pressure spikes at the front of the scoop where water contacts the scoop initially. Low pressure areas are on top of the scoop but are now also more defined behind the scoop. Comparing pressure plots of Design.6 and Design.7, it is already evident that the force will be much larger in Design.7. In Design.7 plot peak pressure registered is more than 30% higher than in Design.6.

For contours to follow in addition to all being coupled with their respective plots, the legend is adjusted to be the same going forward into Design.8, Design.9, and Design.10. This will facilitate qualitative and quantitative comparisons between the results of each design, making it easier to identify improvements.
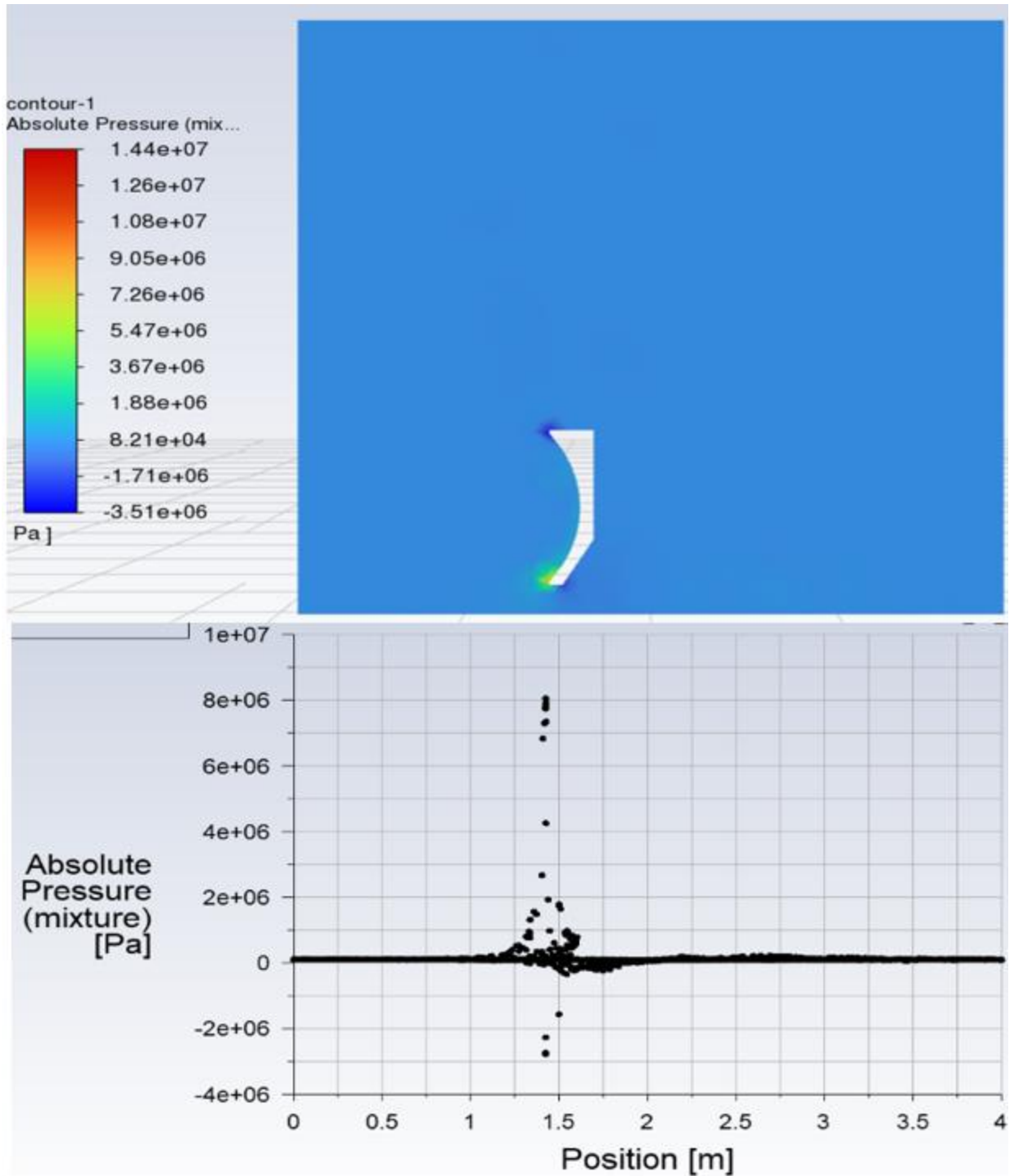
Figure 3.19: Design.7 absolute pressure contour (top) and plot (bottom)

For Velocity magnitude, looking at Figure 3.20, there is higher velocities than in Design.6. It is important to remember however that velocity points are mixed water and air. A better picture

will be formed from analyzing velocity and vorticity fields in X, Y, and Z axis and not just magnitude. Magnitude velocity and vorticity however gives a good indication of what is expected and how the flow has changed from the guard rails addition. For vorticity, Figure 3.21, the control of the flow seems to have concentrated it around the scoop instead of further along the domain.

Turbulent kinetic energy (Figure 3.22) and turbulent intensity (Figure 3.23) are difficult to compare since contours and plots are not the same, but they are higher in Design.6. This could be due to the mixture of air and water in the data. Turbulent kinetic energy (TKE) and turbulent intensity (TI) will be most important in analysis behind the scoop as the turbulent flow contacts scoop attachments such as the pusher sled. Priority parameters for the scoop will be pressure and force.

In Figure 3.24 we can observe water volumetric flow rate and force in time. The red line in the bottom right force plot indicates the moment water contacts the scoop. From the water contour there is much higher water concentration on the arc of the scoop than in Design.6 that can only be attributed to the guard rails. A significant increase in drag force is also demonstrated at 195kN or about 40% increase.

For Design.7 much more data plots and contours were created to extract more detail on the flow. Details that were not extracted in Design.6 such as vorticity plots are in all axes (Plot 3.5 and 3.6), velocity plots in all axes (Plot 3.3 and 3.4), and finally a force plot as it related to the height of the scoop (Plot 3.7). This data will be used to make more detailed comparisons with following designs.
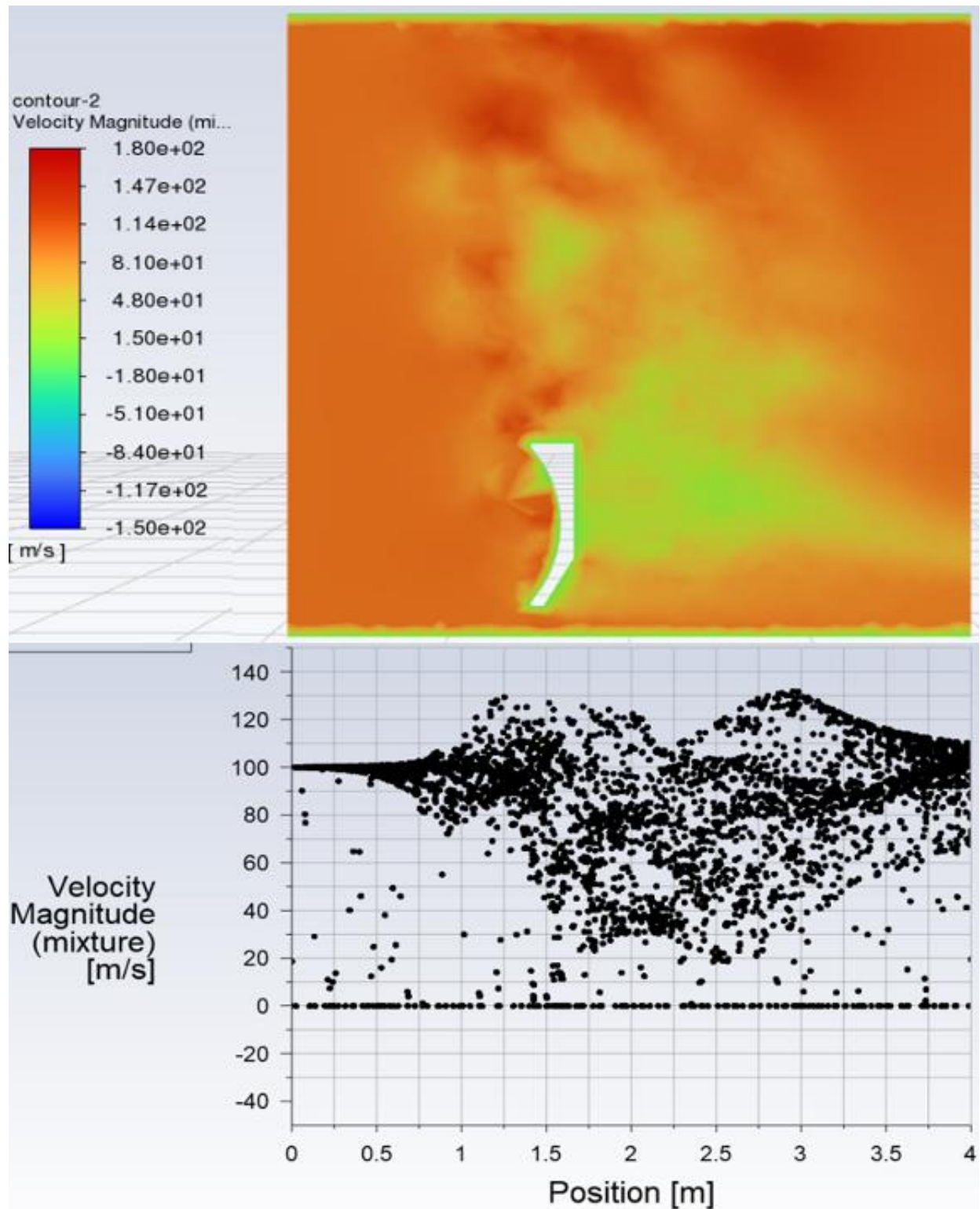
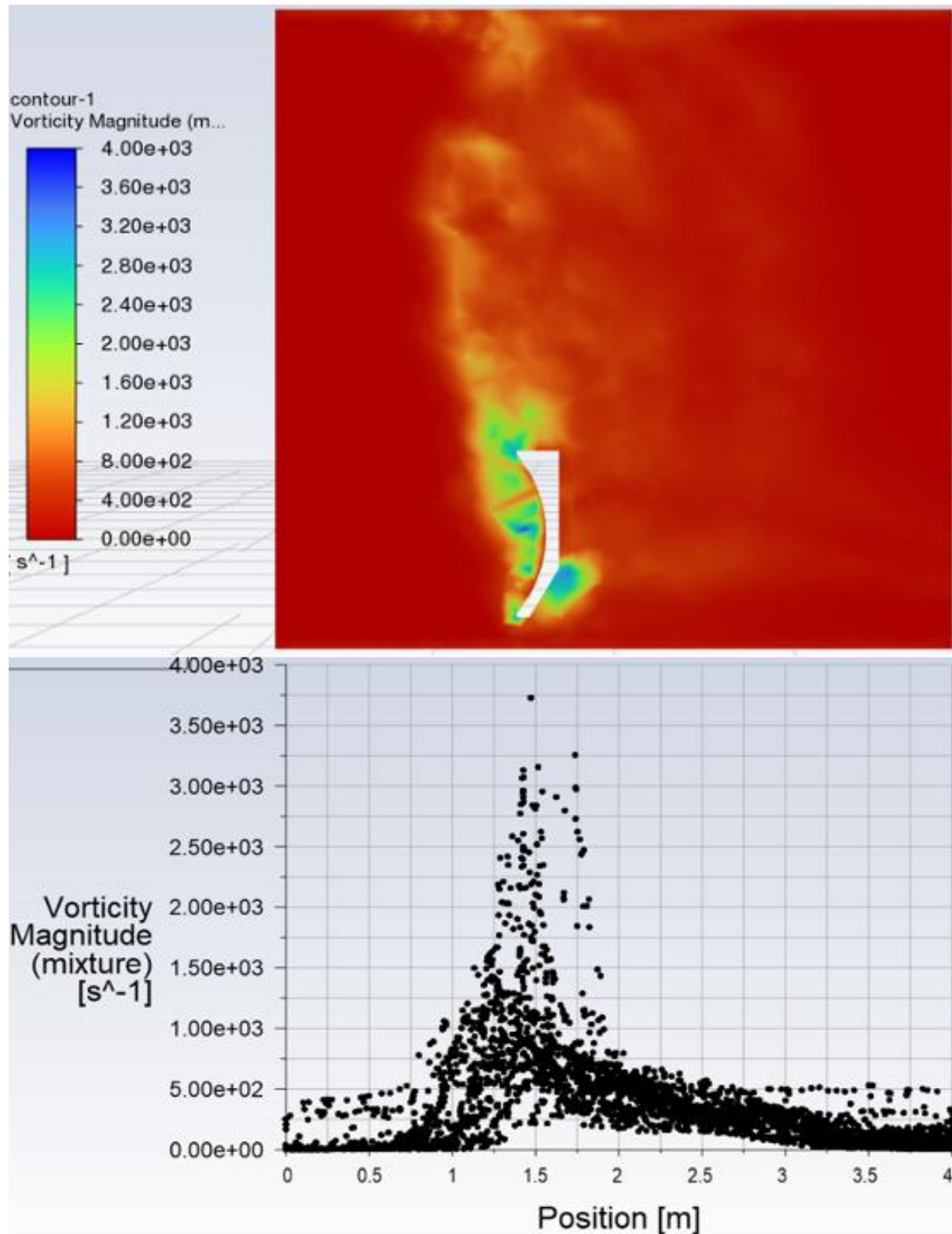Figure 3.20: Design.7 velocity magnitude contour (top) and plot (bottom)

Figure 3.21: Design.7 vorticity magnitude contour (top) and plot (bottom)
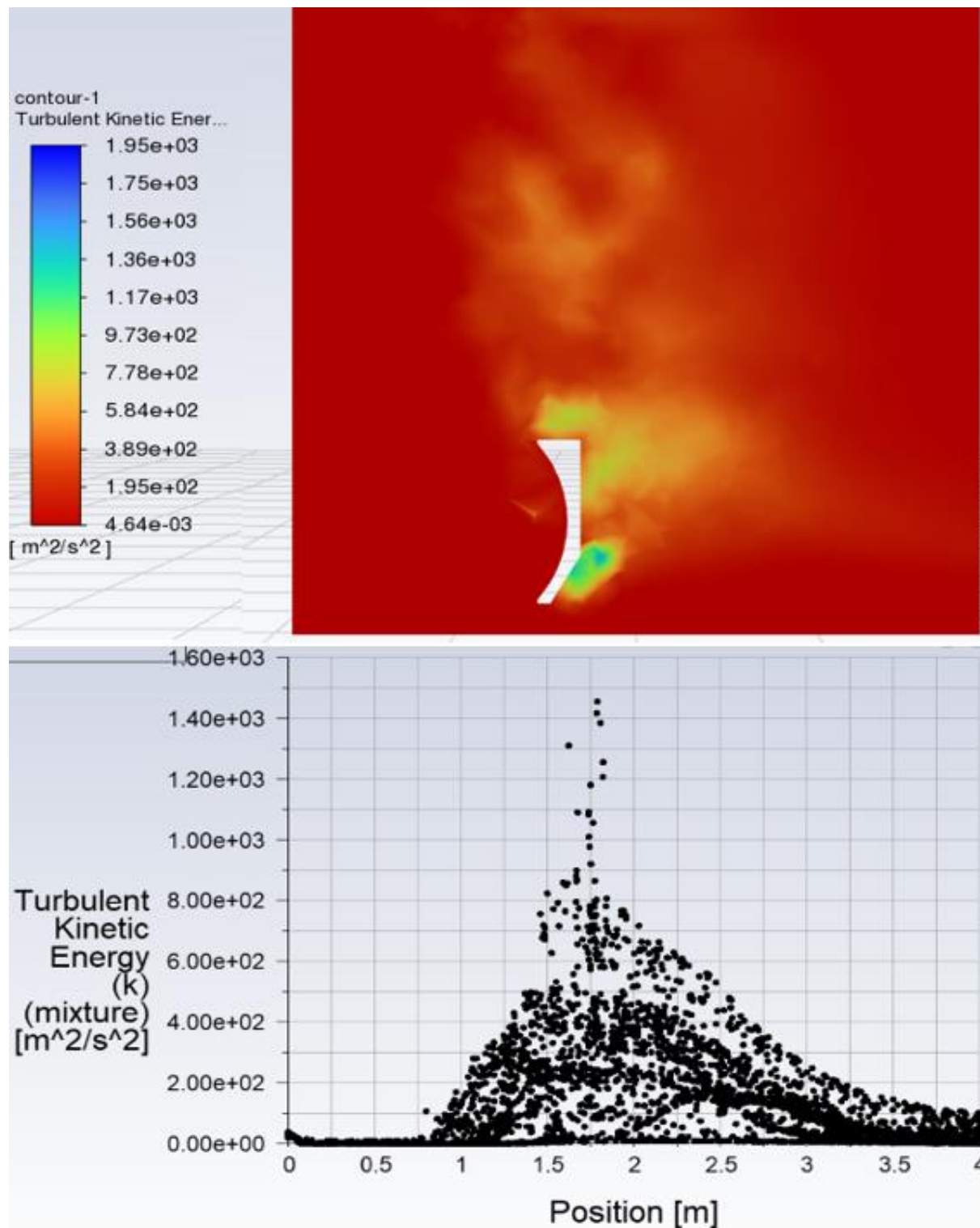
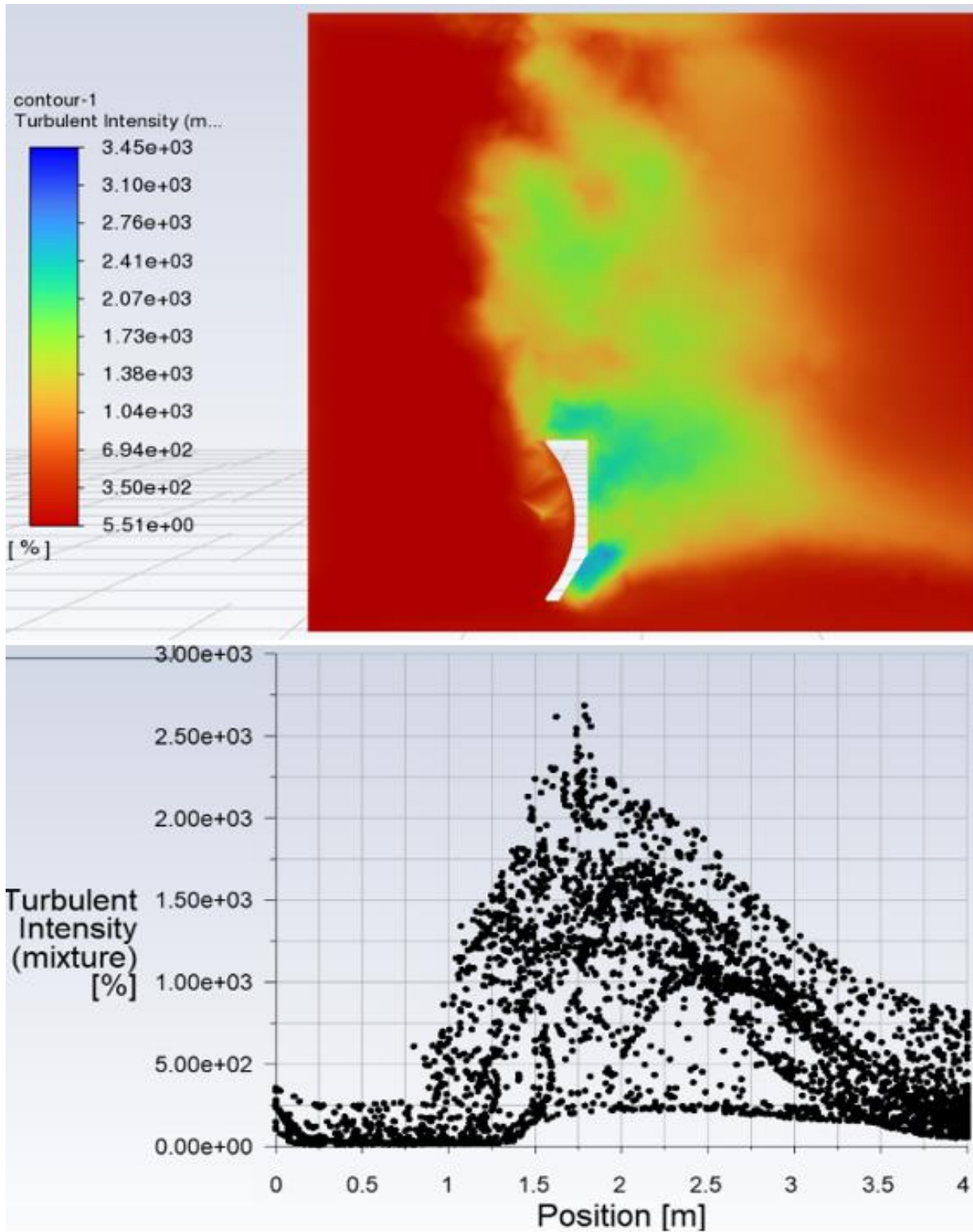Figure 3.22: Design.7 turbulent kinetic energy contour (top) and plot (bottom)

Figure 3.23: Design.7 turbulent intensity contour (top) and plot (bottom)

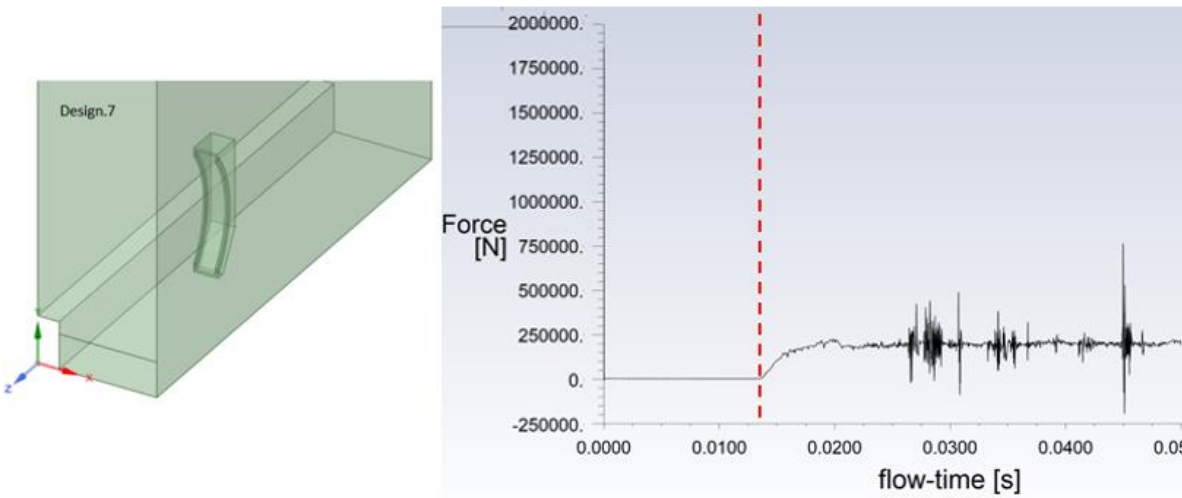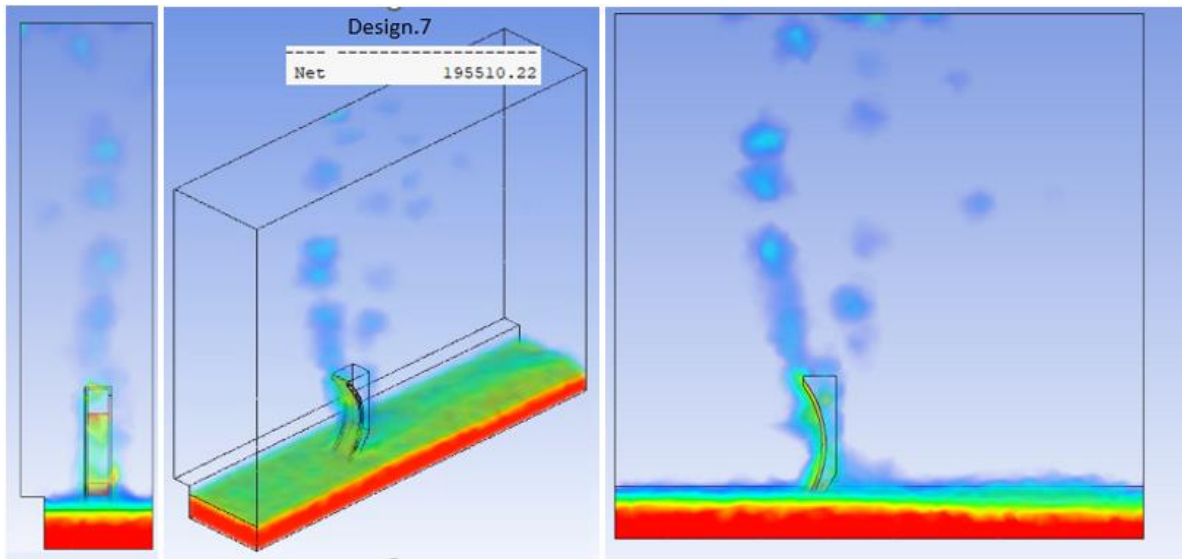Figure 3.24: Design.7 water volumetric flow rate (top), isometric view (bottom left), and drag force plot (bottom right)
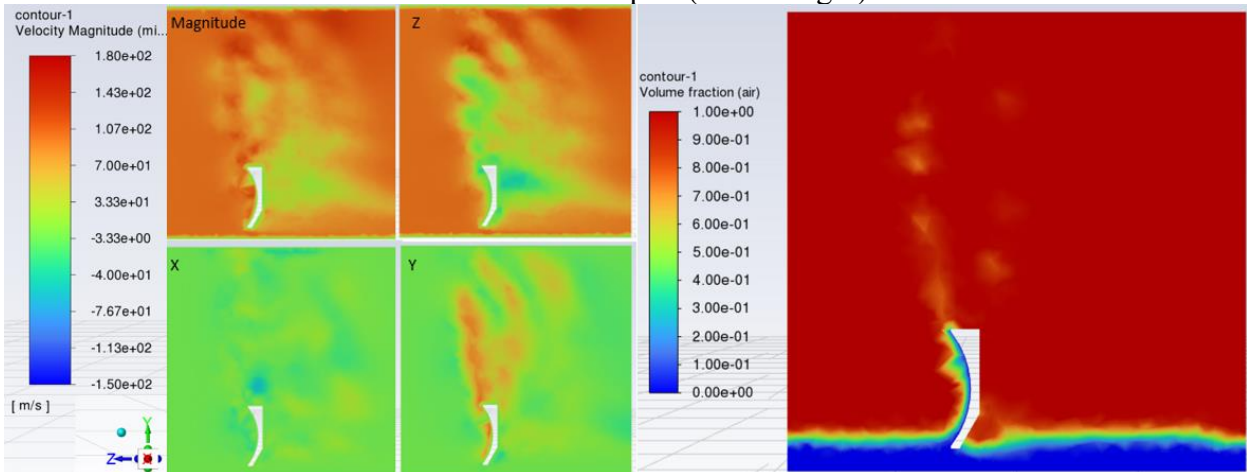
Figure 3.25: Design.7 velocity magnitude and Z, X, and Y axis (left). Volume fraction of air in a plane through the middle of the domain (right)
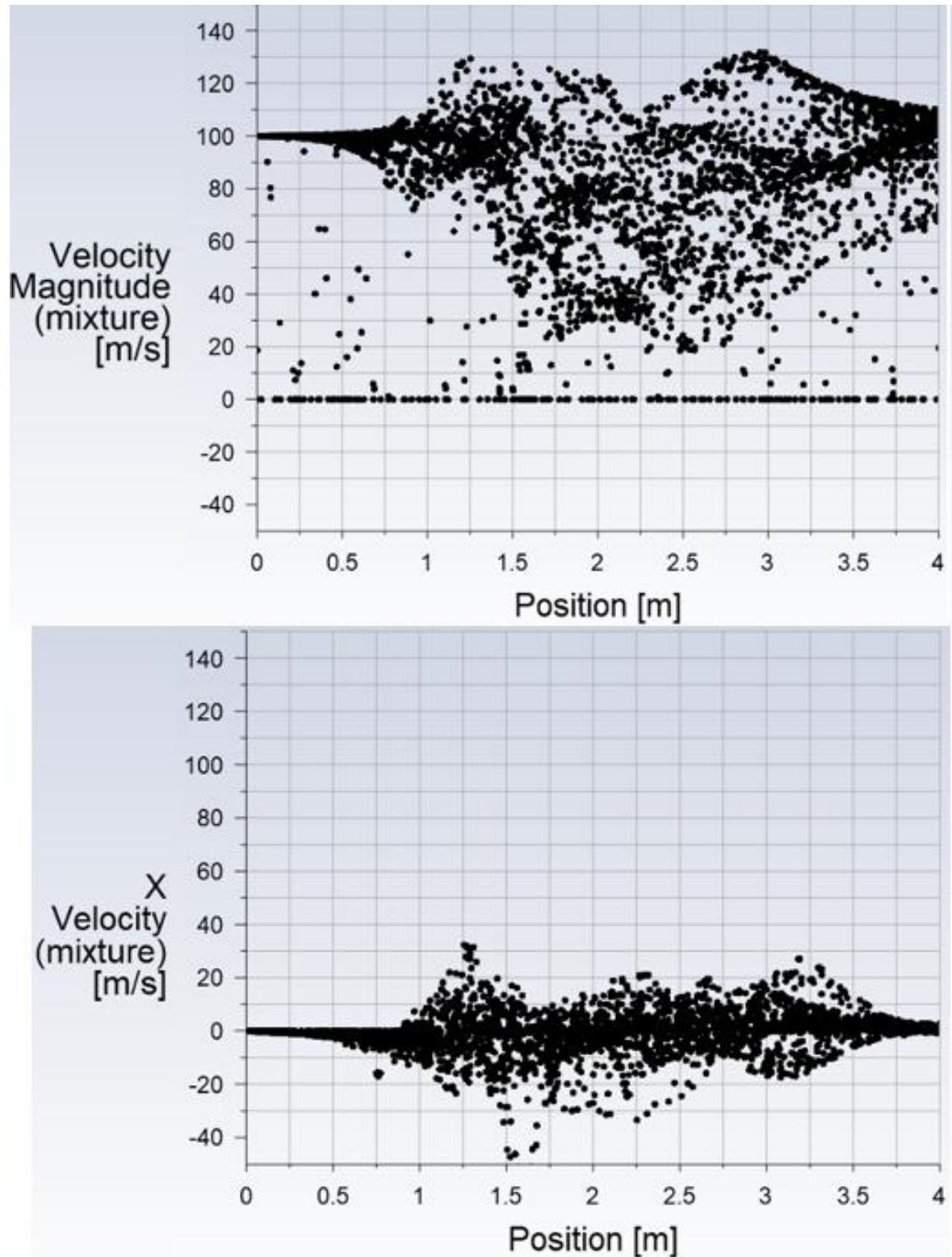
Plot 3.3: Design.7 velocity magnitude (top) and velocity in X-axis (bottom)
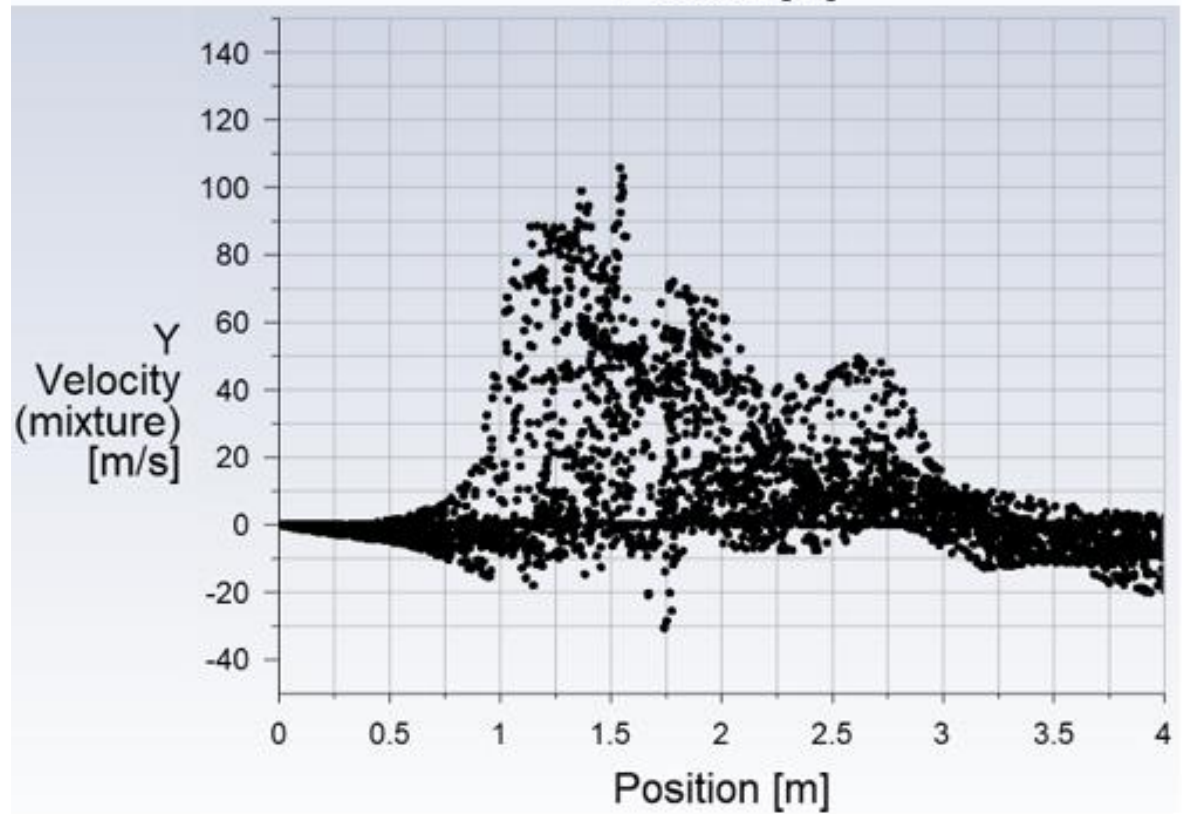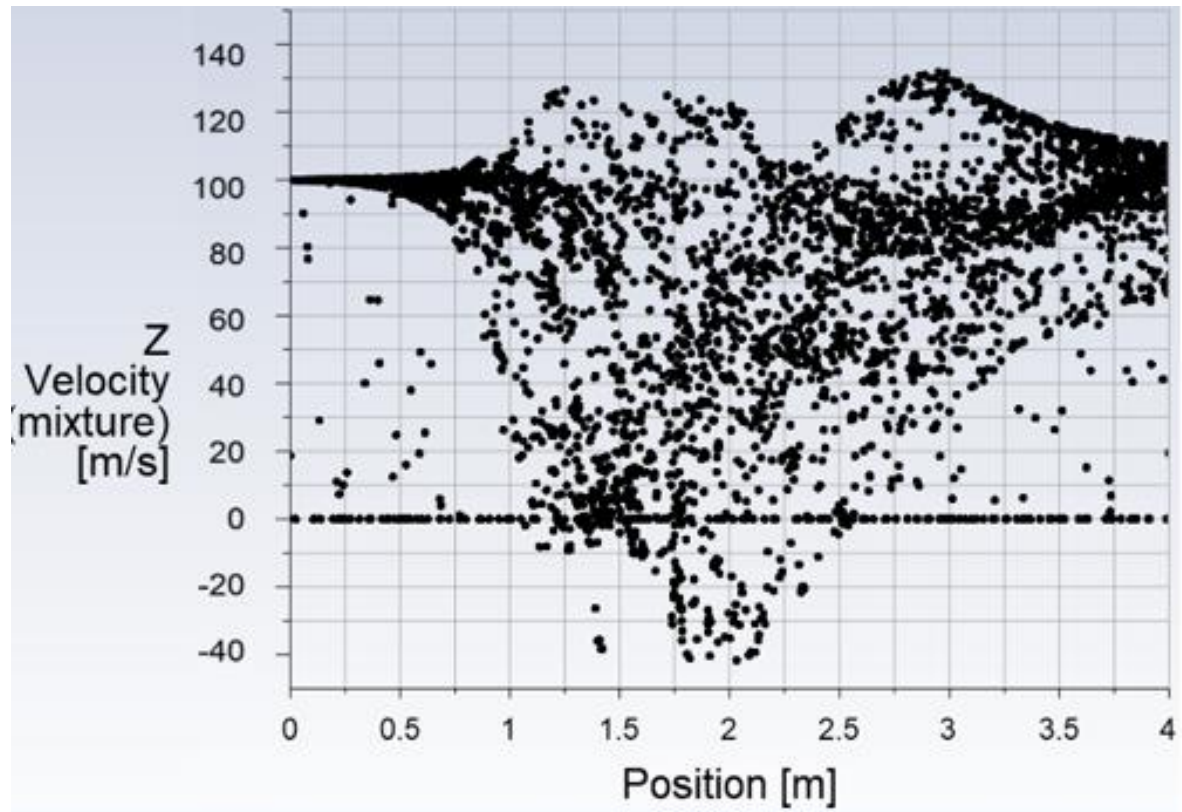
Plot 3.4: Design.7 velocity in Z-axis (top) and velocity in Y-axis (bottom)
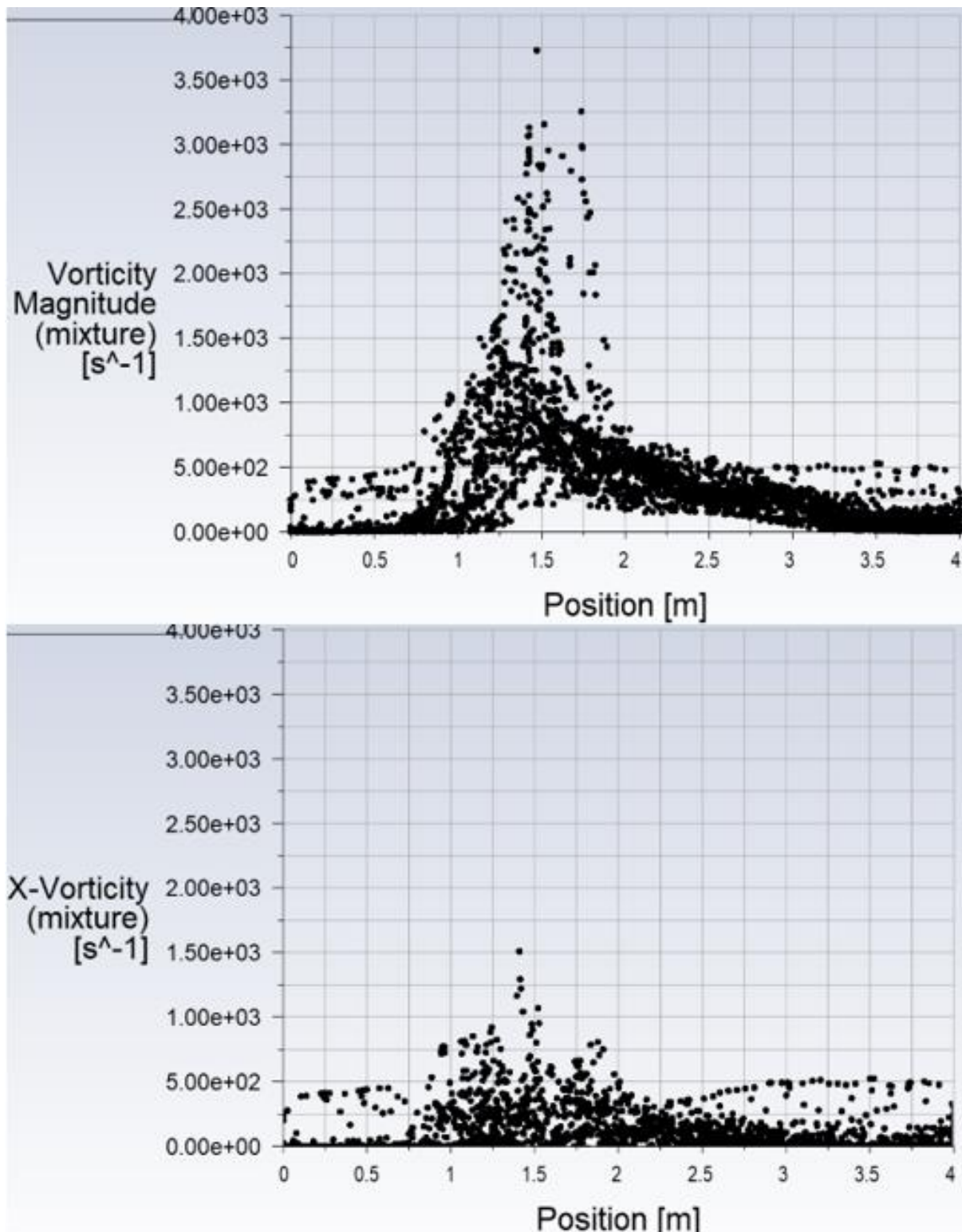
Plot 3.5: Design.7 vorticity magnitude (top) and vorticity in X-axis (bottom)
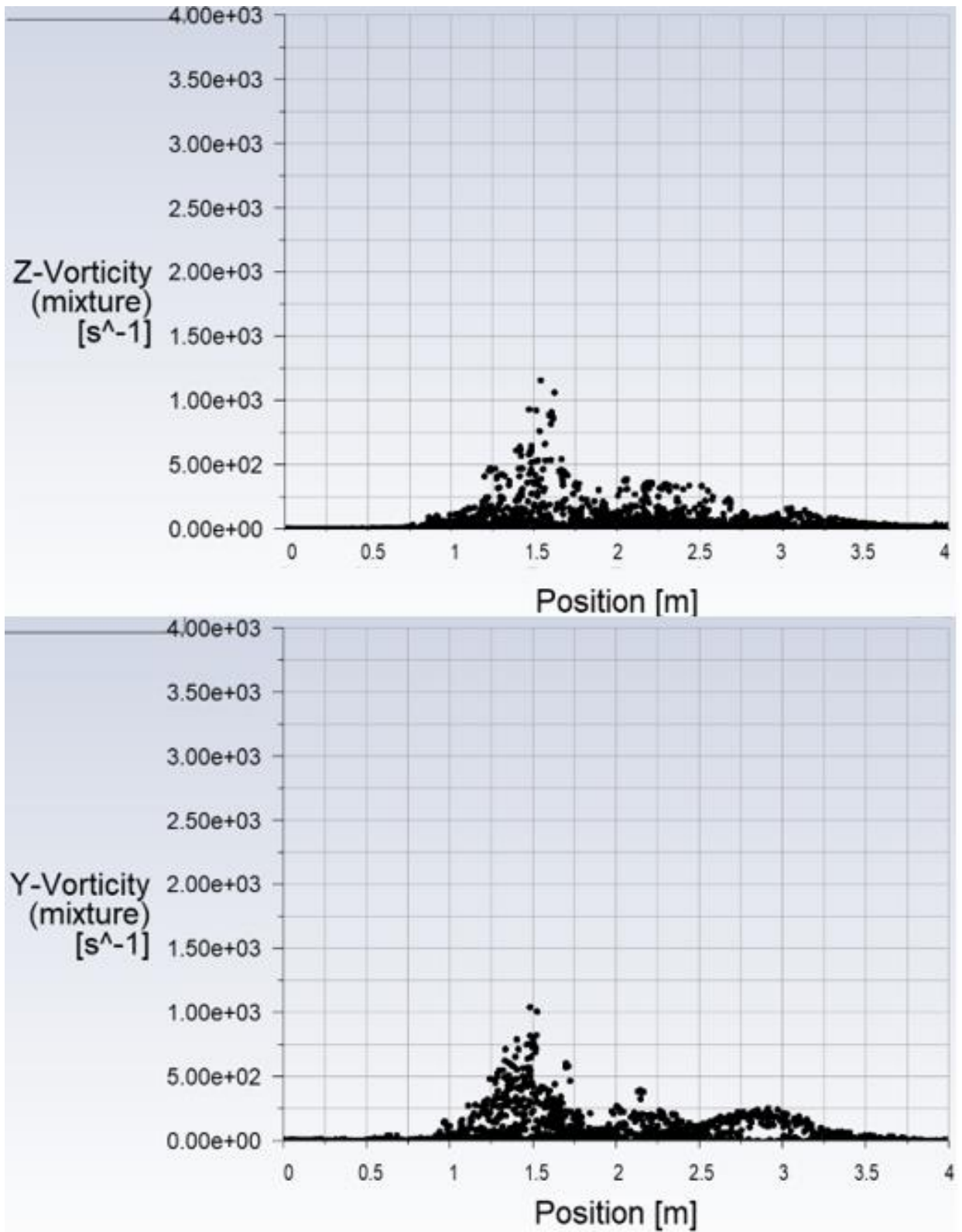
Plot 3.6: Design.7 vorticity in Z-axis (top) and vorticity in Y-axis (bottom)
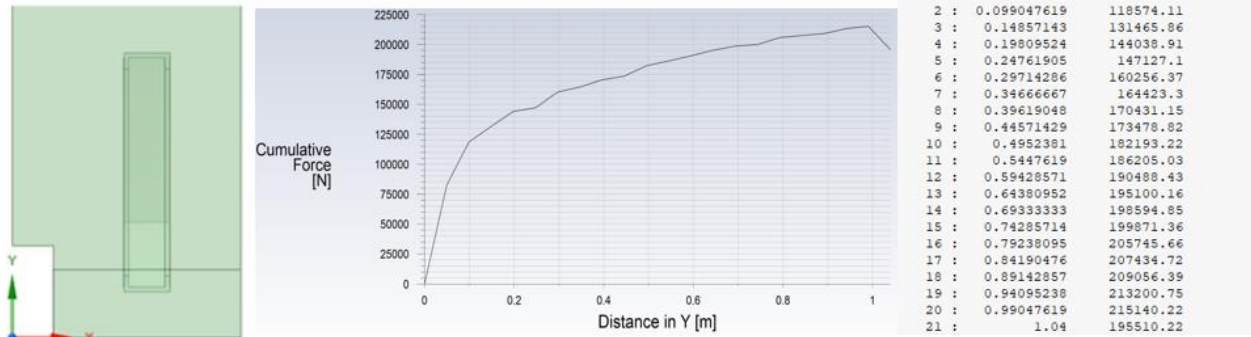
Plot 3.7: Design.7 drag force by scoop height

Doing an analytical calculation to estimate the force for Design.7 gets 200kN compared to computational of 195kN

Force (by hand) = 2.0e5 N/m   Force (2D model) = 1.95e5 N/m

For Design.8 the top and bottom flat areas will be removed. There will probably be a loss of drag as water fails to make direct contact with perpendicular surface but how much and how much will it also affect fluid flow, vorticity, and velocity. From Design.7, having guard rails is a qualitative improvement of over 40% in force.

3.3.2.3 Design.8 at 100 m/s

Design.8 will also have guard rails, but the top and bottom small flat surfaces will be smoothened over with the arc of the scoop. In Figure 3.26 the red circles show exactly the changes from Design.7. On Table 3.6 the illustration to the far left the changes is more evident. Average element quality is also consistent with Design.6 and Design.7. Improvement on lowest element quality is improved without the small flat surfaces, Table 3.6.
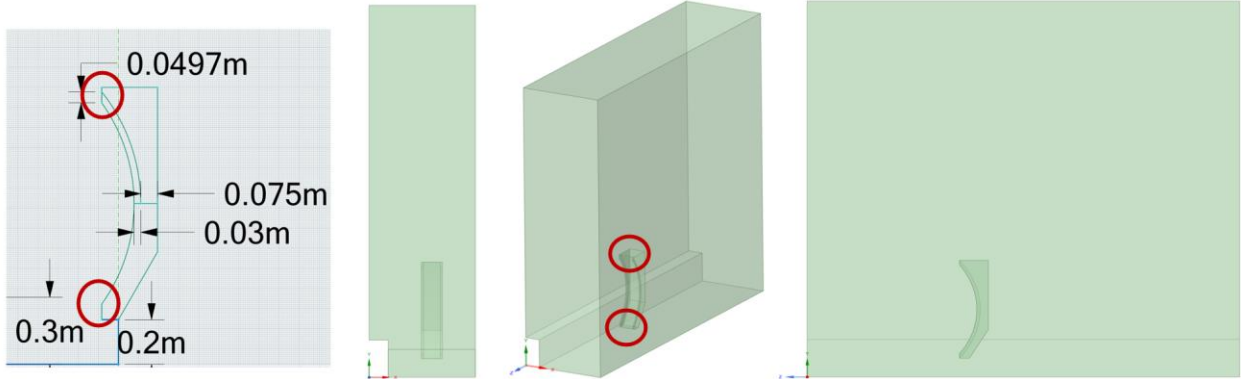
Figure 3.26: Design.8 geometry changes and views from changes made from Design.7

Table 3.6: Statistics of Design.8 mesh

Bounding Box	
Length X	1. m
Length Y	4. m
Length Z	4. m
Properties	
Volume	15.688 m³
Centroid X	0.50739 m
Centroid Y	2.0349 m
Centroid Z	-2.0006 m
Statistics	
Nodes	16737
Elements	84379
Mesh Metric	Element Quality
Min	0.22624
Max	0.9995
Average	0.83465
Standard Deviation	9.6624e-002

Design.8_3-D

From the changes made pressure at the top and bottom of the front scoop were reduced more than 50% (Figure 3.27), going lower than even Design.6. The velocity contour in Figure 3.28 provides early insight of flow deflected forward except for back bottom of the scoop where vorticity is also at its highest, Figure 3.29. Prior in Design.7 vorticity was also at its peak around the front arc and front top.

In concurrence with vorticity turbulent kinetic energy noticeably lower, Figure 3.30, but turbulent intensity behind the scoop was increased, Figure 3.31. Smooth flow up the scoop has removed the turbulence generated from the flat surfaces previously.

Table 3.7: Statistics of Design.8 boundaries

Object Name	air_inlet	water_inlet	walls	back_outlet	scoop_back.bottom_walls	scoop_back.top_walls	walls	scoop_front.mid.arc_walls
State	Fully Defined							
Scope								
Scoping Method	Geometry Selection							
Geometry	1 Face	6 Faces	1 Face		2 Faces			3 Faces
Definition								
Send to Solver	Yes							
Protected	Program Controlled							
Visible	Yes							
Program Controlled Inflation	Exclude							
Statistics								
Type	Manual							
Total Selection	1 Face	6 Faces	1 Face		2 Faces			3 Faces
Surface Area	3.682 m²	0.246 m²	40. m²	3.928 m²	8.8298e-002 m²	0.20068 m²	0.295 m²	0.2216 m²
Suppressed	0							
Used by Mesh Worksheet	No							

Object Name	scoop_front.mid.arc.sides_walls	scoop_front.bottom_walls	scoop_front.top_walls
State			
Scoping Method			
Geometry	2 Faces		
Send to Solver			
Protected			
Visible			
Program Controlled Inflation			
Type			
Total Selection	2 Faces		
Surface Area	6.4259e-002 m²	1.9027e-003 m²	
Suppressed			
Used by Mesh Worksheet			

From Figure 3.32, force on the scoop is 179kN, a drop of about 8.3% from Design.7. A drop in energy can be attributed to the channeling of water upwards without perpendicular surfaces to disrupt flow and cause higher turbulence. The lower turbulence may also cause increased flow separation that could affect flow interaction behind the scoop.

Getting more detail from vorticity in Figure 3.34 the guards on the arc seem to cause vorticity in the X axis more than in Y and Z velocity changes are mostly in the Z and Y however, Figure 3.33, Plot 3.8, and Plot 3.9.
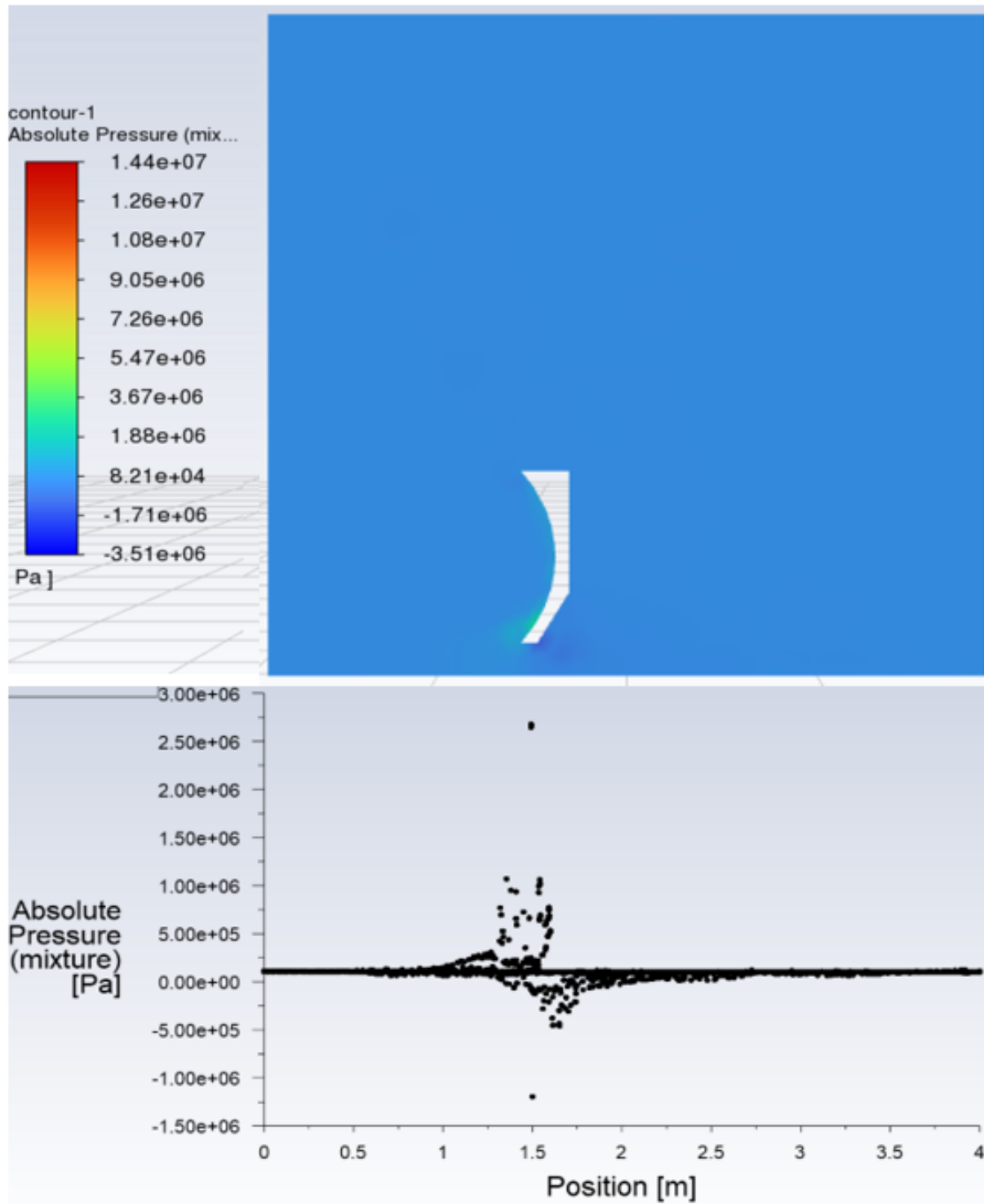
Figure 3.27: Design.8 absolute pressure contour (top) and plot (bottom)
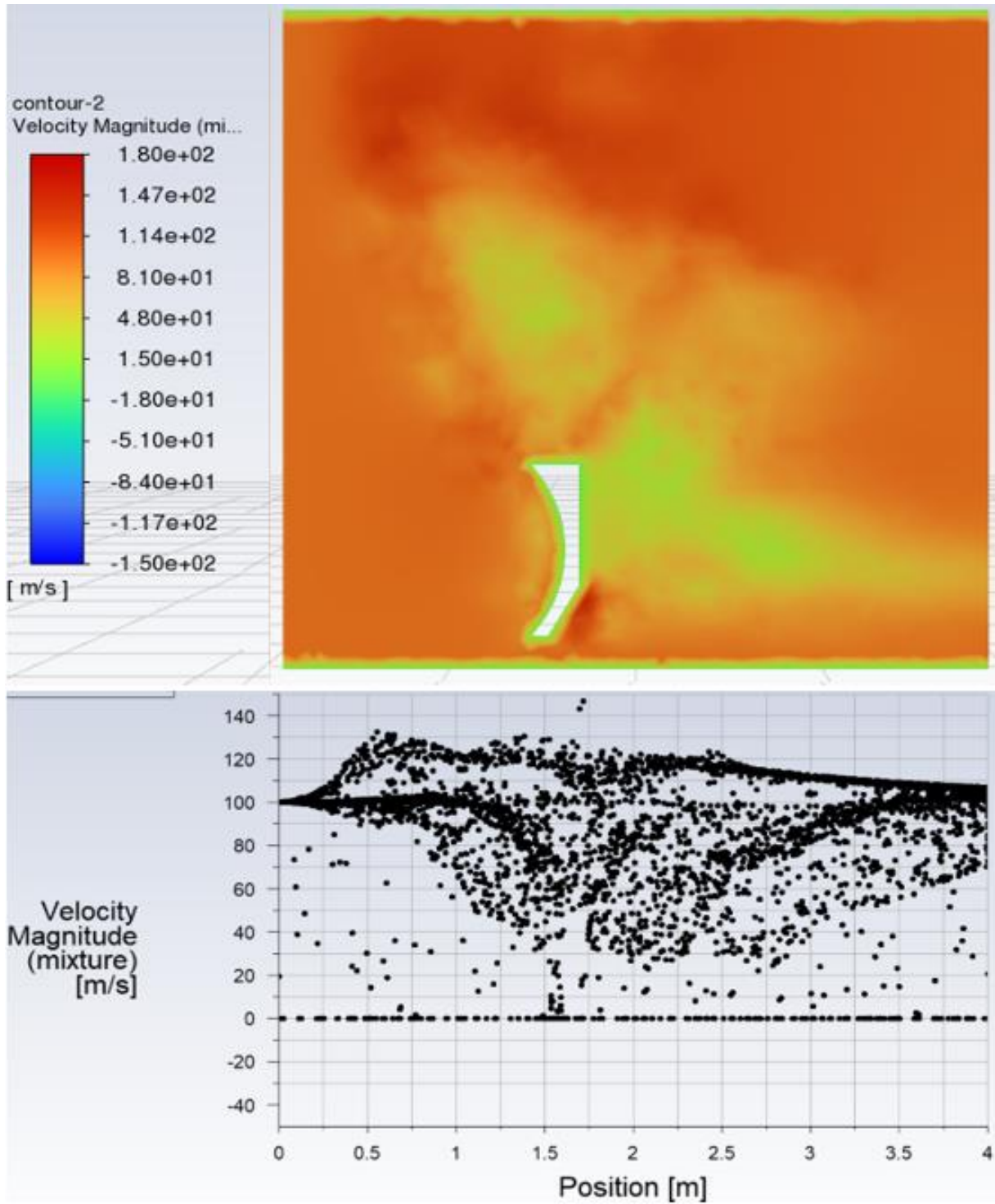
Figure 3.28: Design.8 velocity magnitude contour (top) and plot (bottom)
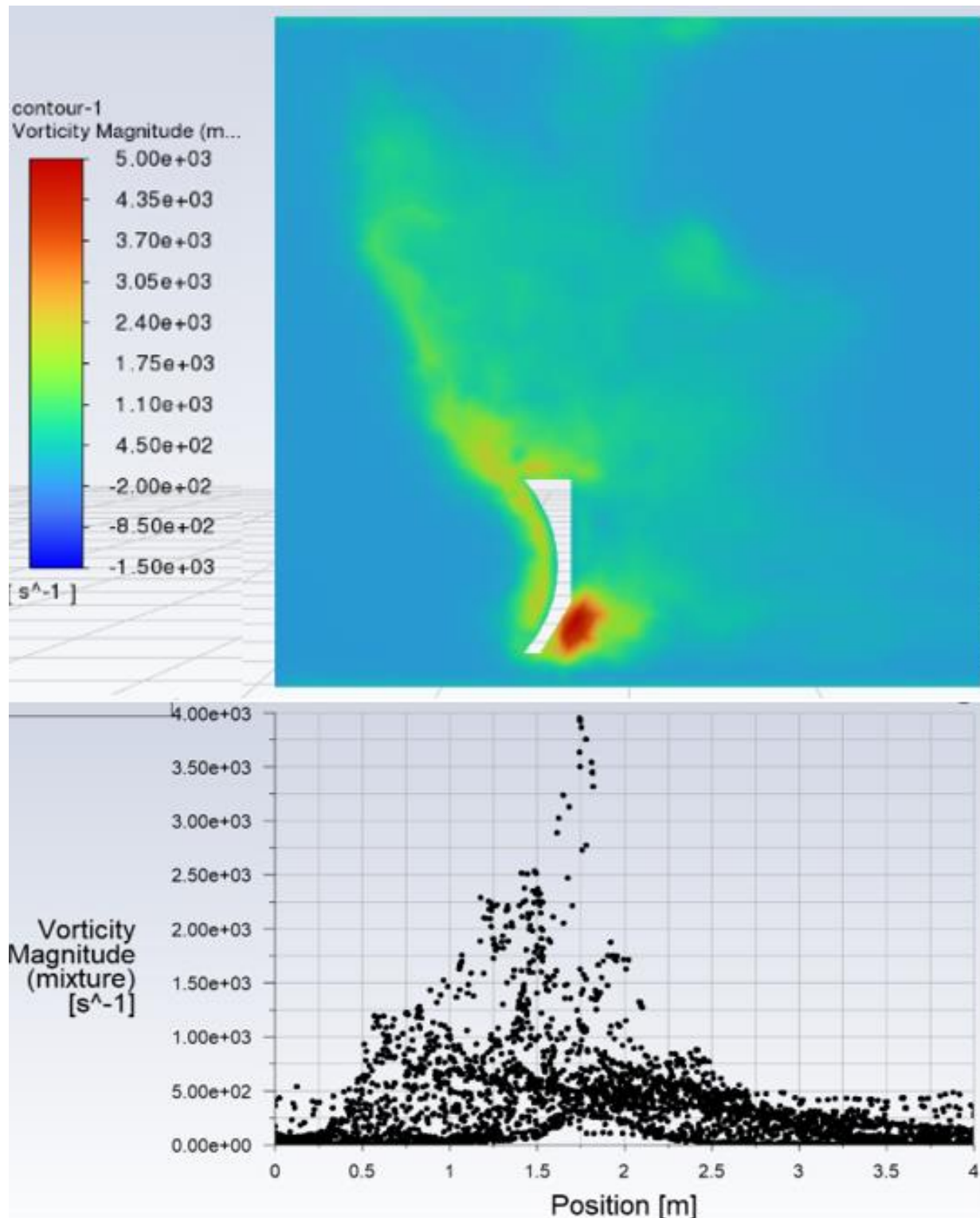
Figure 3.29: Design.8 vorticity magnitude contour (top) and plot (bottom)
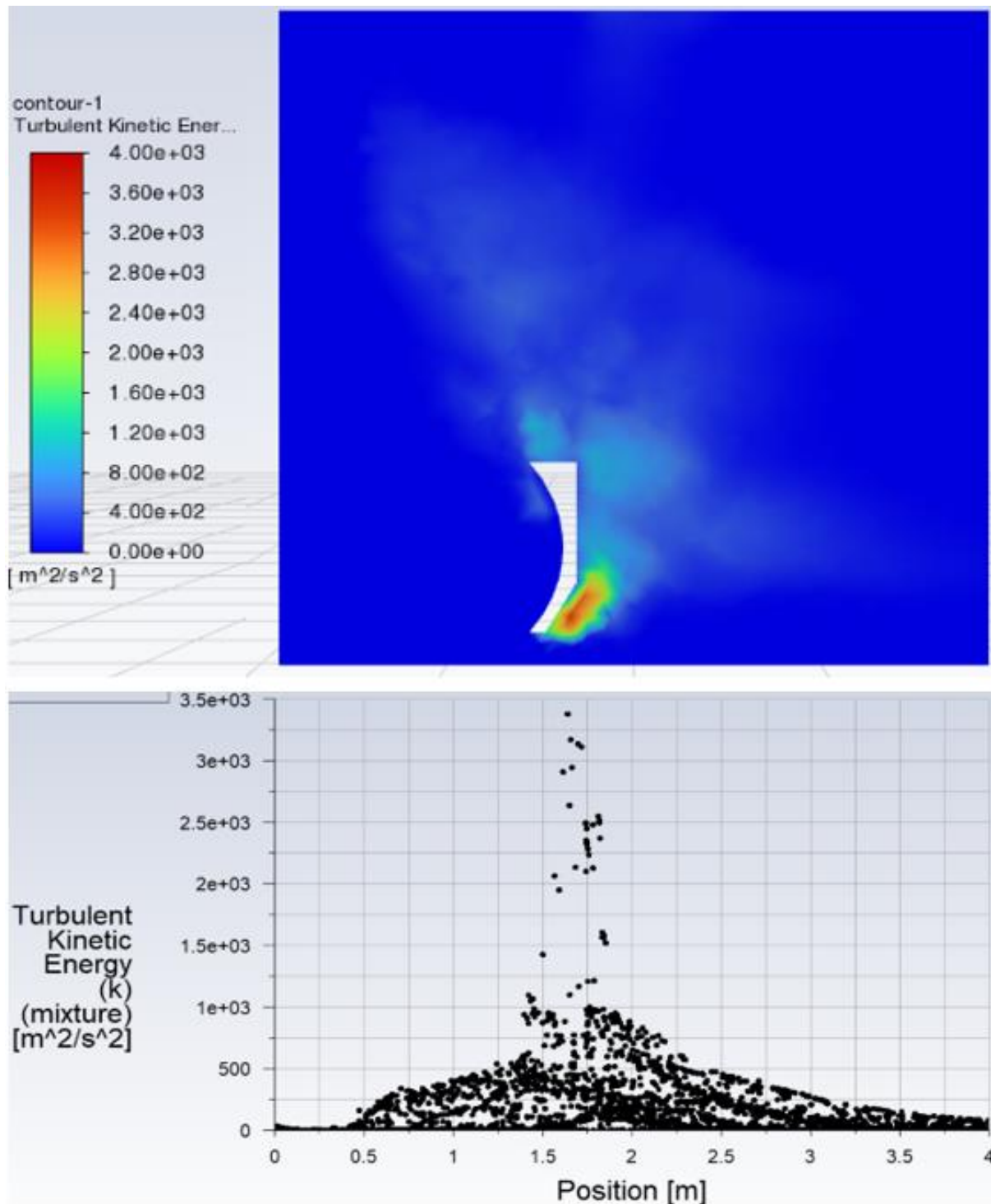
Figure 3.30: Design.8 turbulent kinetic energy contour (top) and plot (bottom)
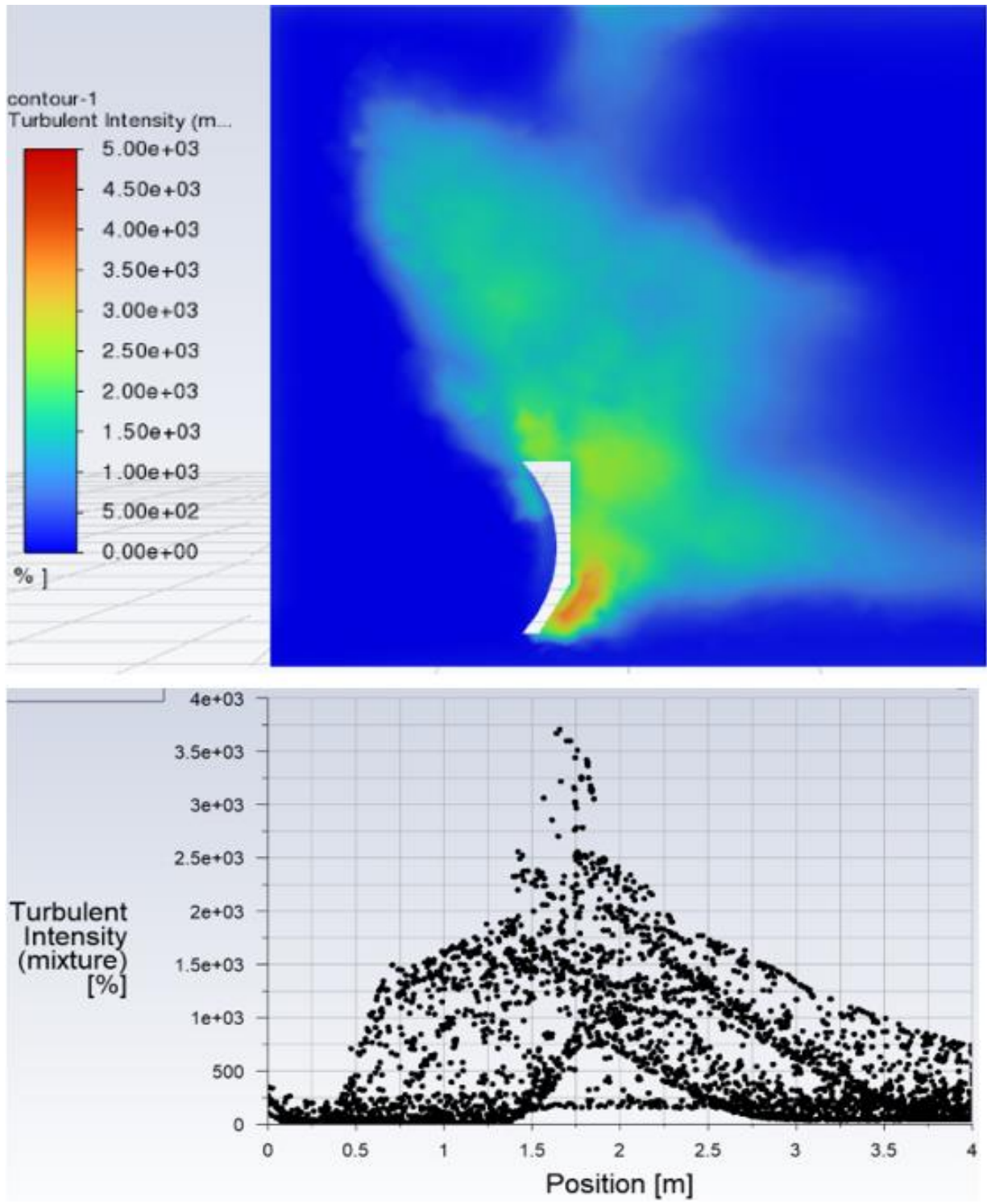
Figure 3.31: Design.8 turbulent intensity contour (top) and plot (bottom)
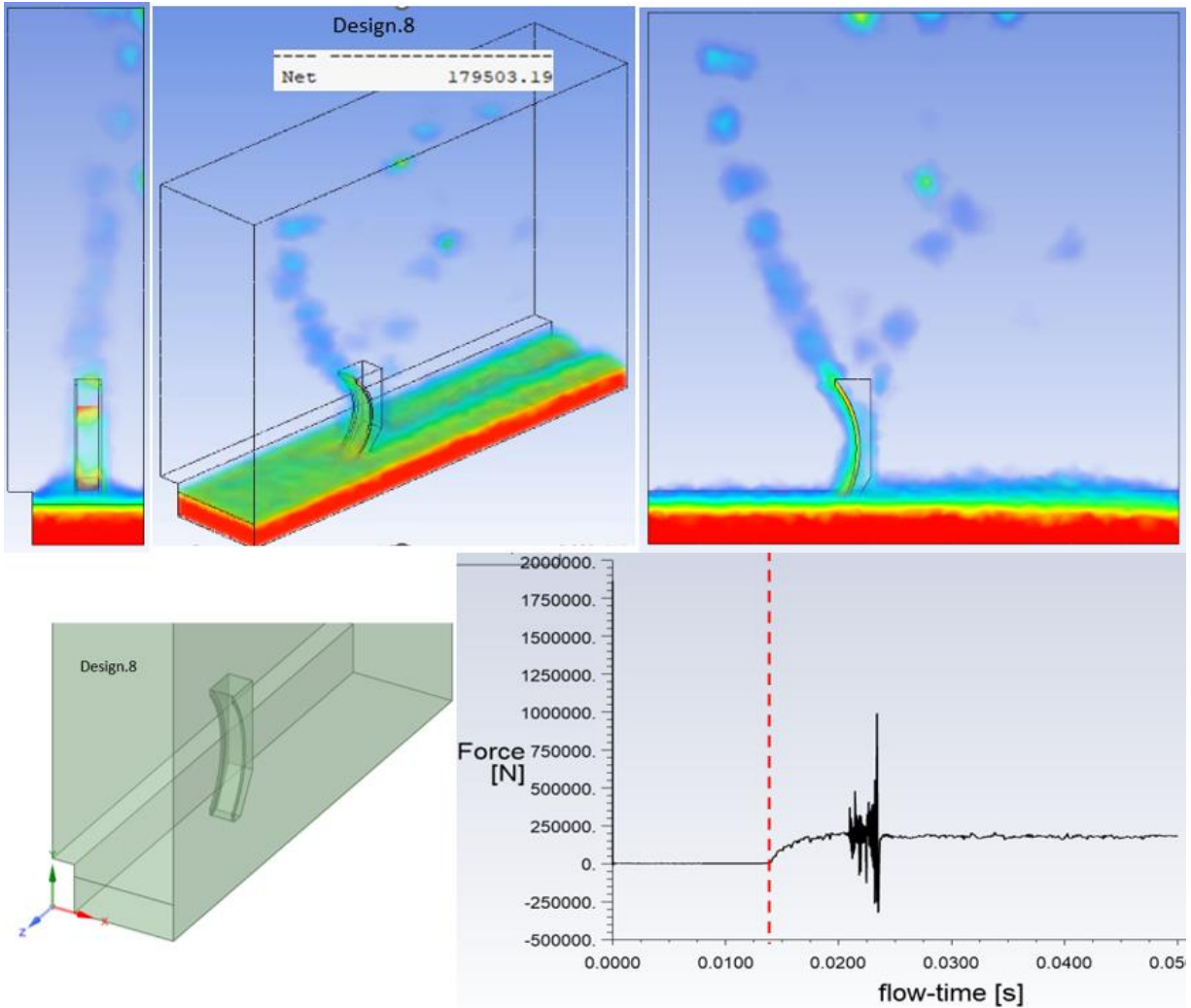
Figure 3.32: Design.8 water volumetric flow rate (top), isometric view (bottom left), and drag force plot (bottom right)
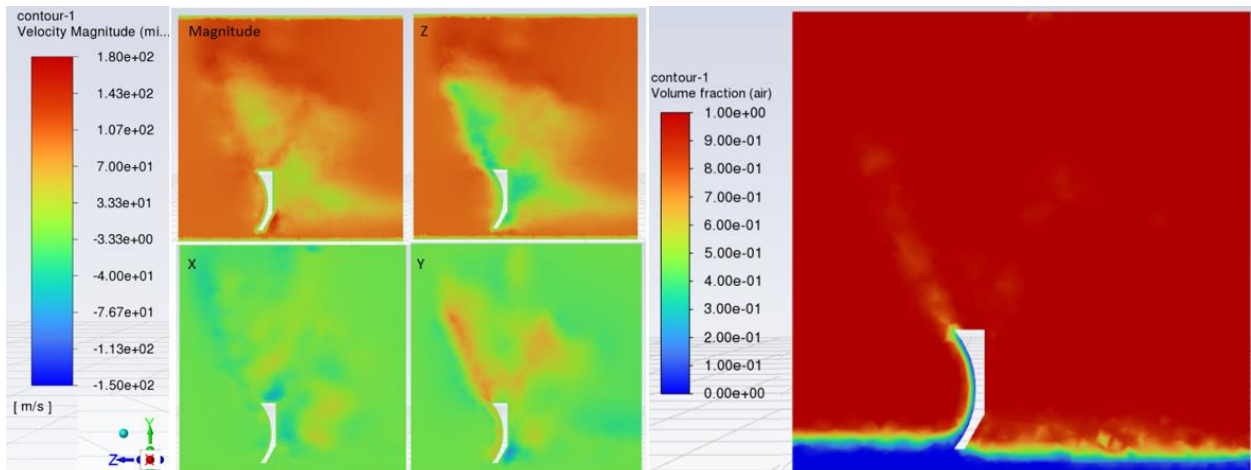
Figure 3.33: Design.8 velocity magnitude and in Z, X, and Y axis (left). Volume fraction of air in a plane through the middle of the domain (right)

65
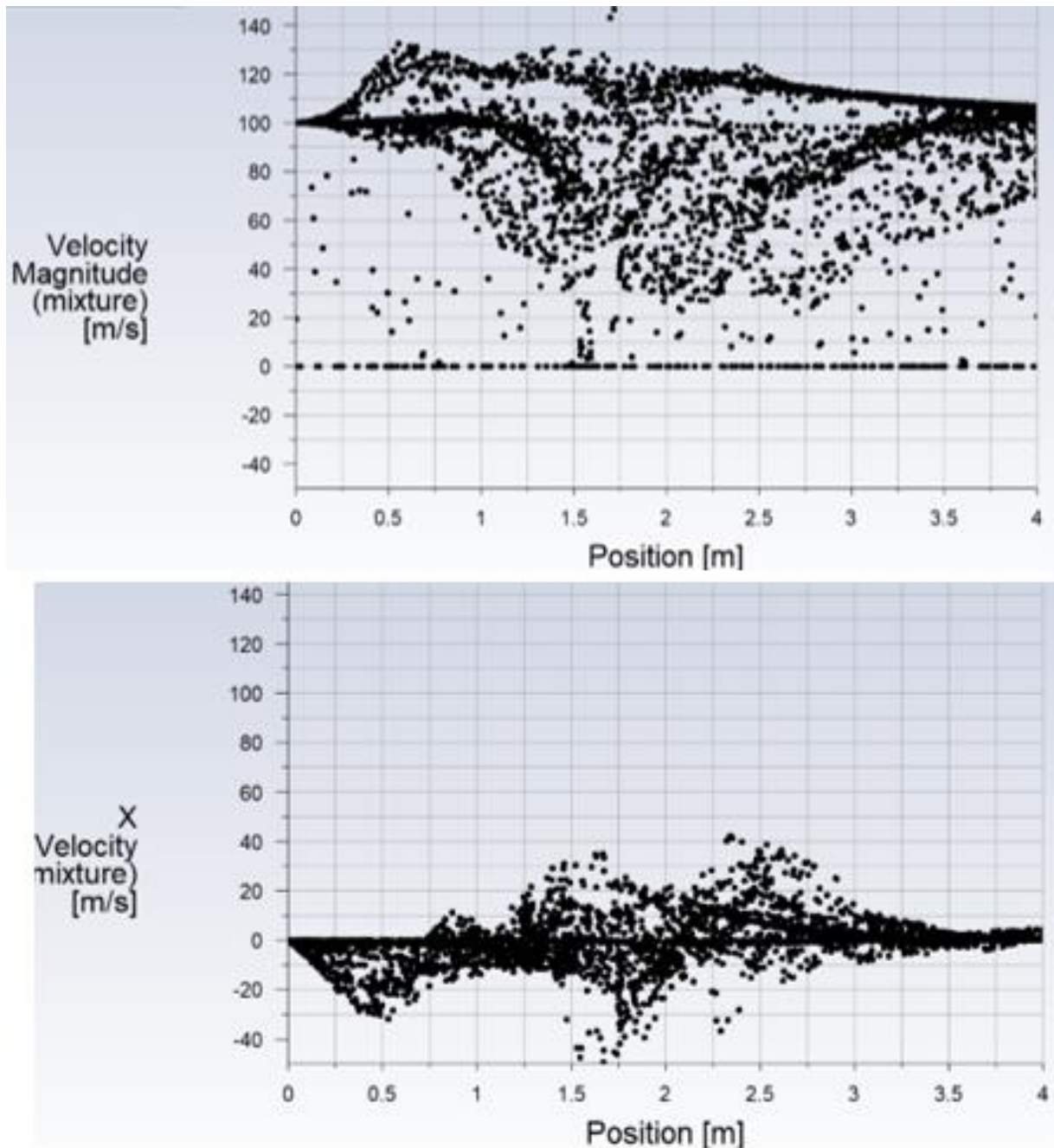
Plot 3.8: Design.8 velocity magnitude (top) and velocity in X-axis (bottom)
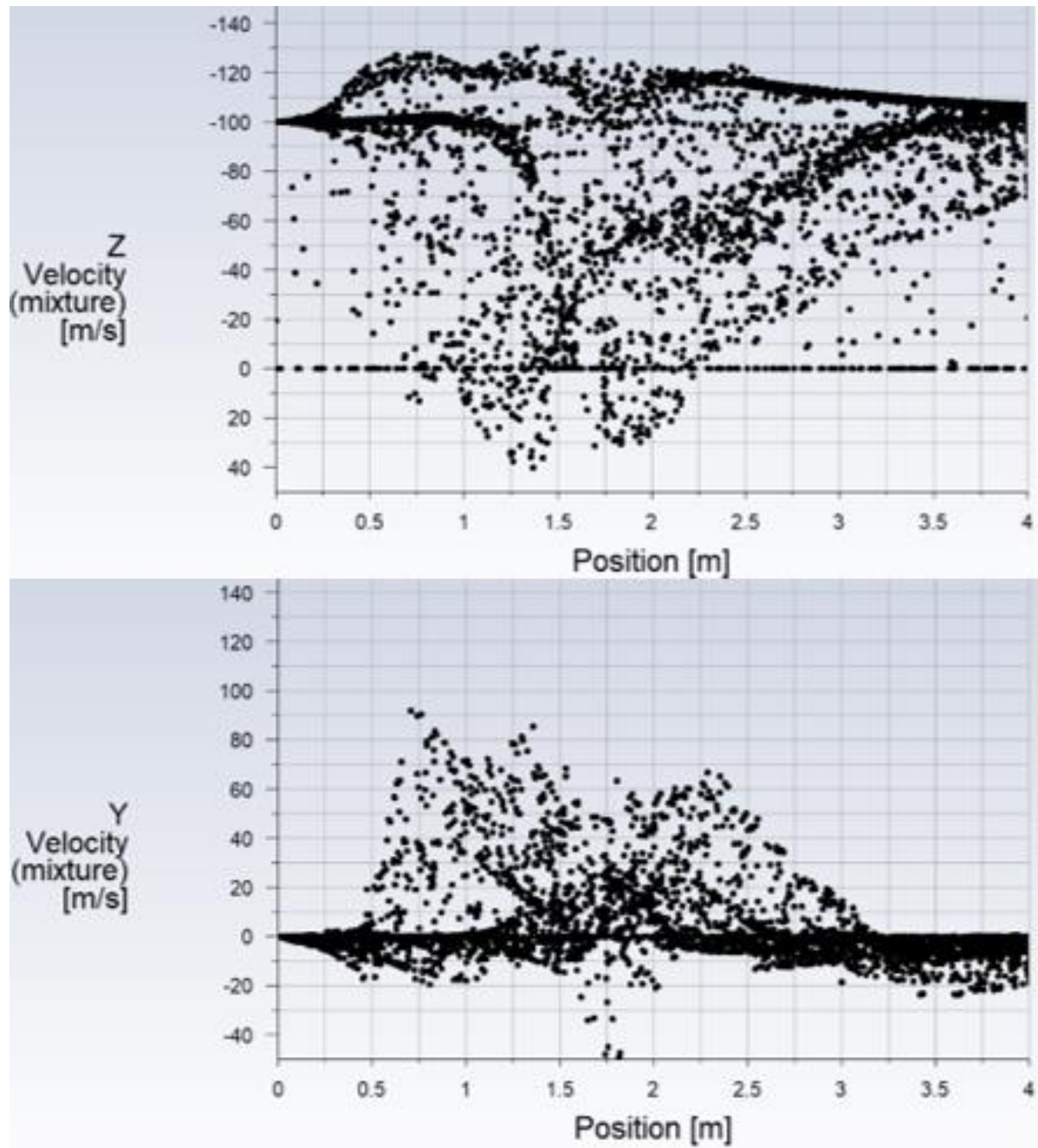
Plot 3.9: Design.8 velocity in Z-axis (top) and velocity in Y-axis (bottom)
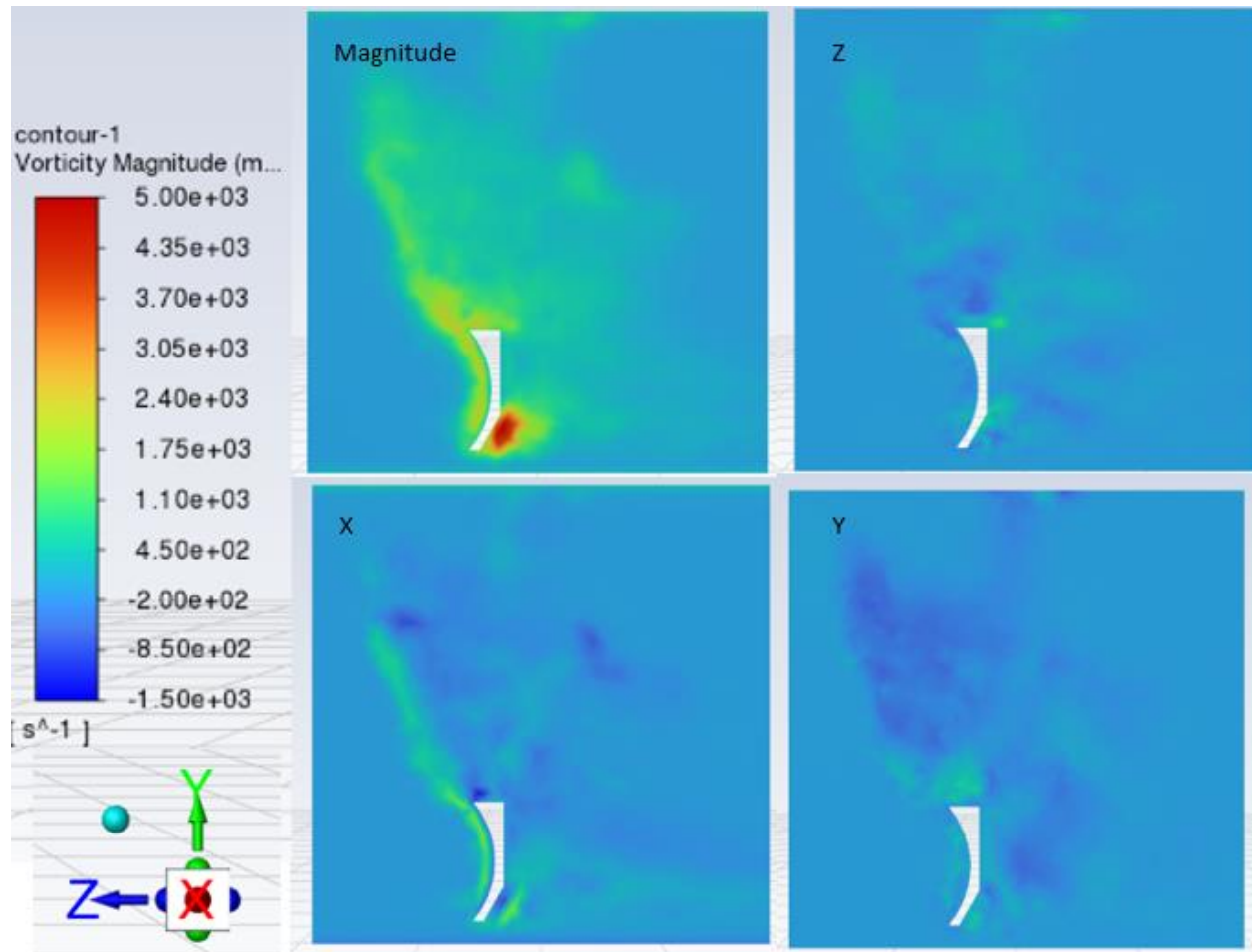
Figure 3.34: Design.8 vorticity magnitude and in Z, X, and Y axis (left). Volume fraction of air in a plane through the middle of the domain (right)
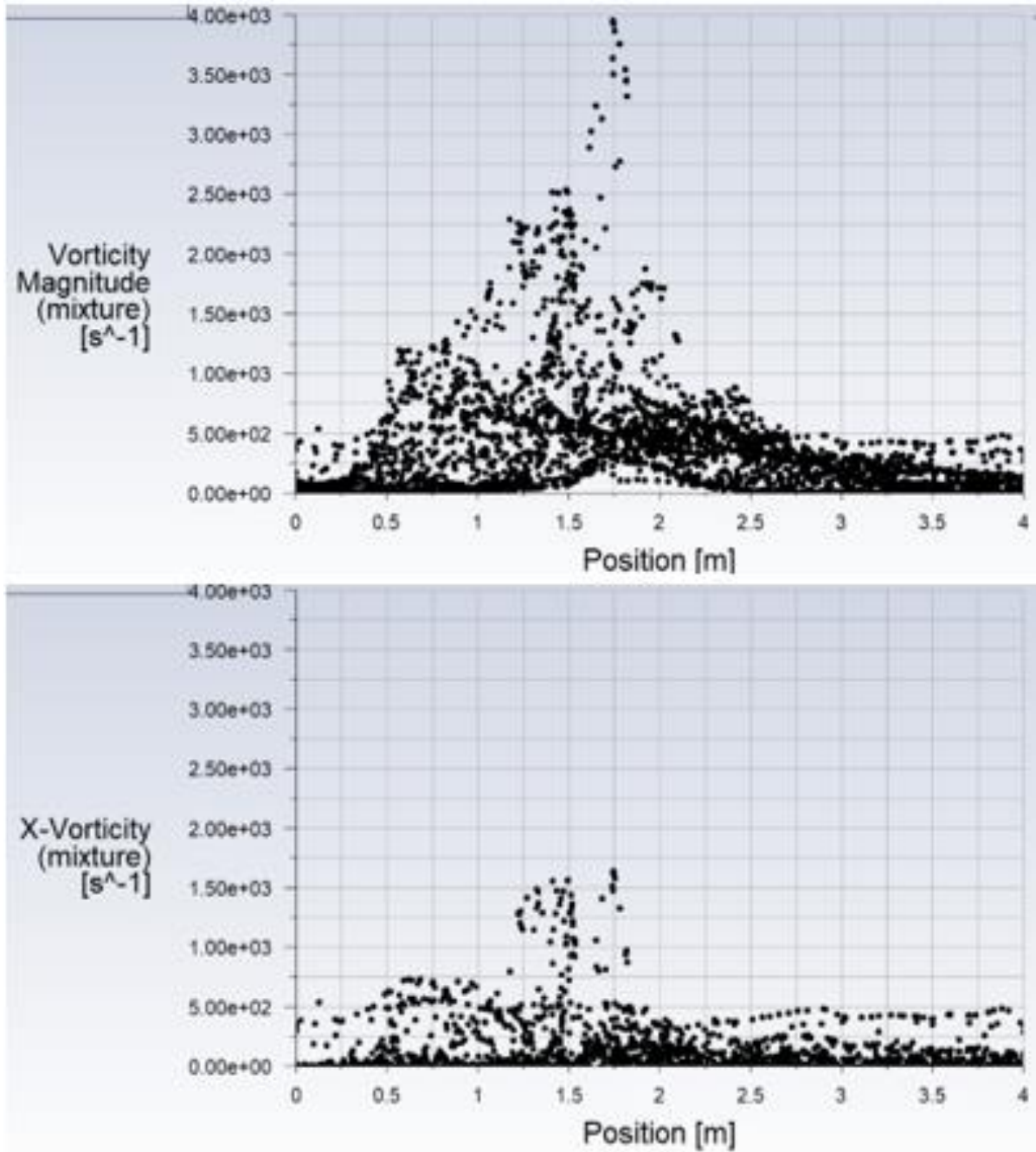
Plot 3.10: Design.8 vorticity magnitude (top) and vorticity in X-axis (bottom)
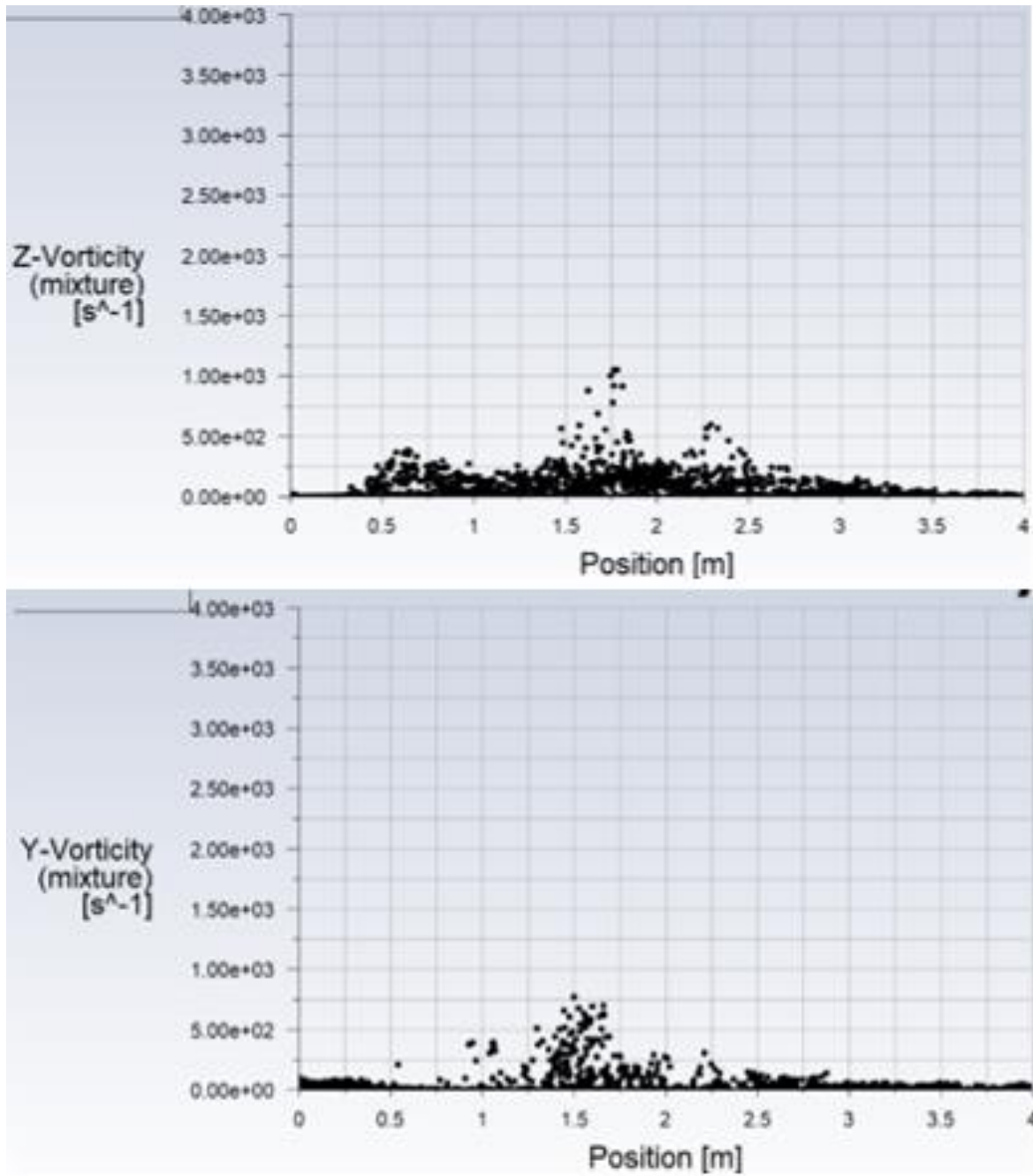
Plot 3.11: Design.8 vorticity in Z-axis (top) and vorticity in Y-axis (bottom)
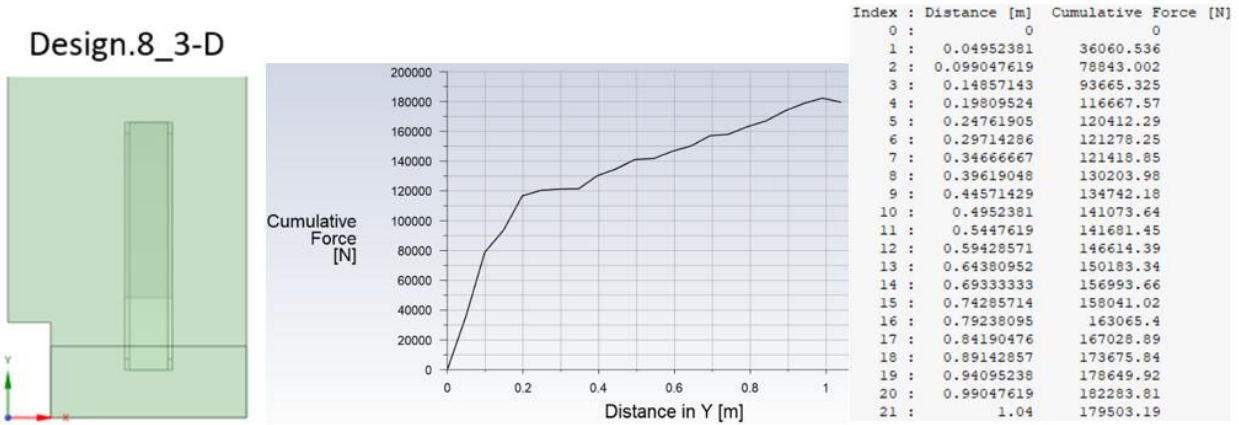
Plot 3.12: Design.8 drag force by scoop height

Aggregating the results for Design.8, scoop has less drag and turbulence with sharper increases in velocity vectors on the Z and Y axis. Analyzing Plot 3.12 decline of force observed in Plot 3.7 for Design.7 is not as marked. Although Design.7 experiences more drag the next geometric change will focus on the back top of the scoop.

3.3.2.4 Design.9 at 100 m/s

For Design.9 the top of the back of the scoop will have a 60-degree divergence, Figure 3.35. The objective is to analyze how the geometric angled opening affects pressure gradients and therefore flow behind the scoop. Additional benefits would include less mass as a scoop and therefore weight which means scoop and sled could accelerate faster.
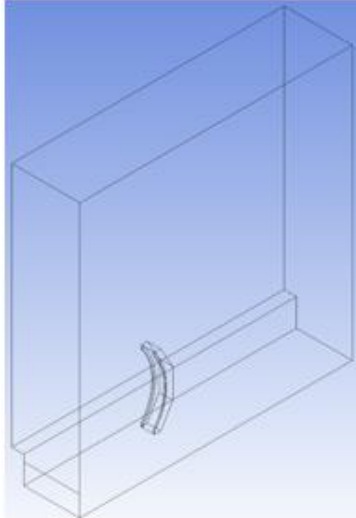
Figure 3.35: Design.9 geometry changes and views from changes made from Design.8

71

Table 3.8: Statistics of Design.9 mesh

Bounding Box	
Length X	1. m
Length Y	4. m
Length Z	4. m
Properties	
Volume	15.693 m³
Centroid X	0.50742 m
Centroid Y	2.0346 m
Centroid Z	-2.0005 m
Statistics	
Nodes	16655
Elements	83929
Mesh Metric	None

Design.9_3-D
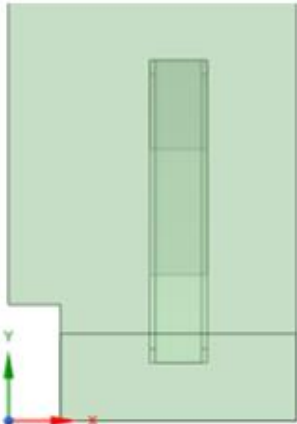
Table 3.9: Statistics of Design.9 boundaries

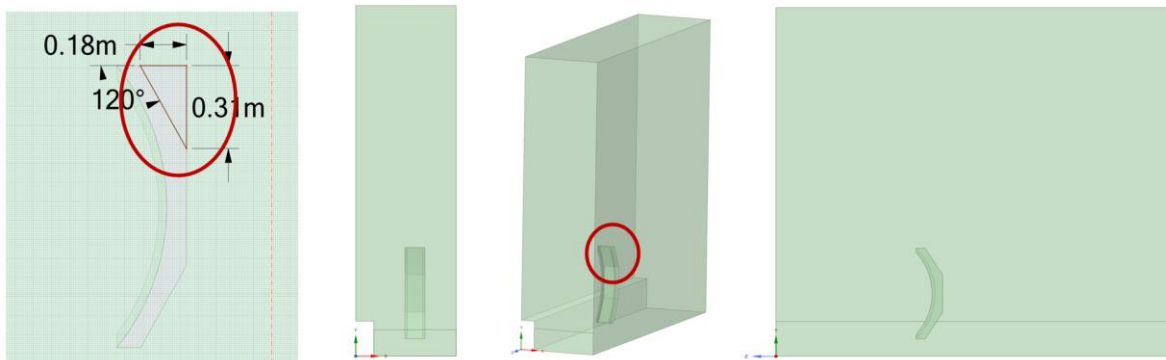| Object Name	air_inlet	water_inlet	walls	back_outlet	scoop_back.top_walls
State					
Scoping Method					
Geometry	1 Face	6 Faces	1 Face	3 Faces	
Send to Solver					
Protected					
Visible					
Program Controlled Inflation					
Type					
Total Selection	1 Face	6 Faces	1 Face	3 Faces	
Surface Area	3.682 m²	0.246 m²	40. m²	3.928 m²	0.17484 m²
Suppressed					
Used by Mesh Worksheet					

Object Name	scoop_back.bottom_walls	scoop_front.mid.arcs_walls	scoop_front.bottom_wall	scoop_front.top_walls	scoop_front.arc.mid.sides_walls	scoop_walls
State		Fully Defined				
Scope						
Scoping Method		Geometry Selection				
Geometry	2 Faces	3 Faces		2 Faces		
Definition						
Send to Solver		Yes				
Protected		Program Controlled				
Visible		Yes				
Program Controlled Inflation		Exclude				
Statistics						
Type		Manual				
Total Selection	2 Faces	3 Faces		2 Faces		
Surface Area	8.8298e-002 m²	0.2216 m²	1.9027e-003 m²	6.4259e-002 m²		0.24105 m²
Suppressed		0				
Used by Mesh Worksheet		No				

As with the other Design.7 and Design.8, there are tables for mesh statistics are. These tables are Table 3.8 and Table 3.9.

With the first contour and plot, Figure 3.36, clear changes in gradient pressure fields are qualified and quantified. Negative pressure point behind the scoop is less comparatively. This is likely due to less flow separation caused by our change.
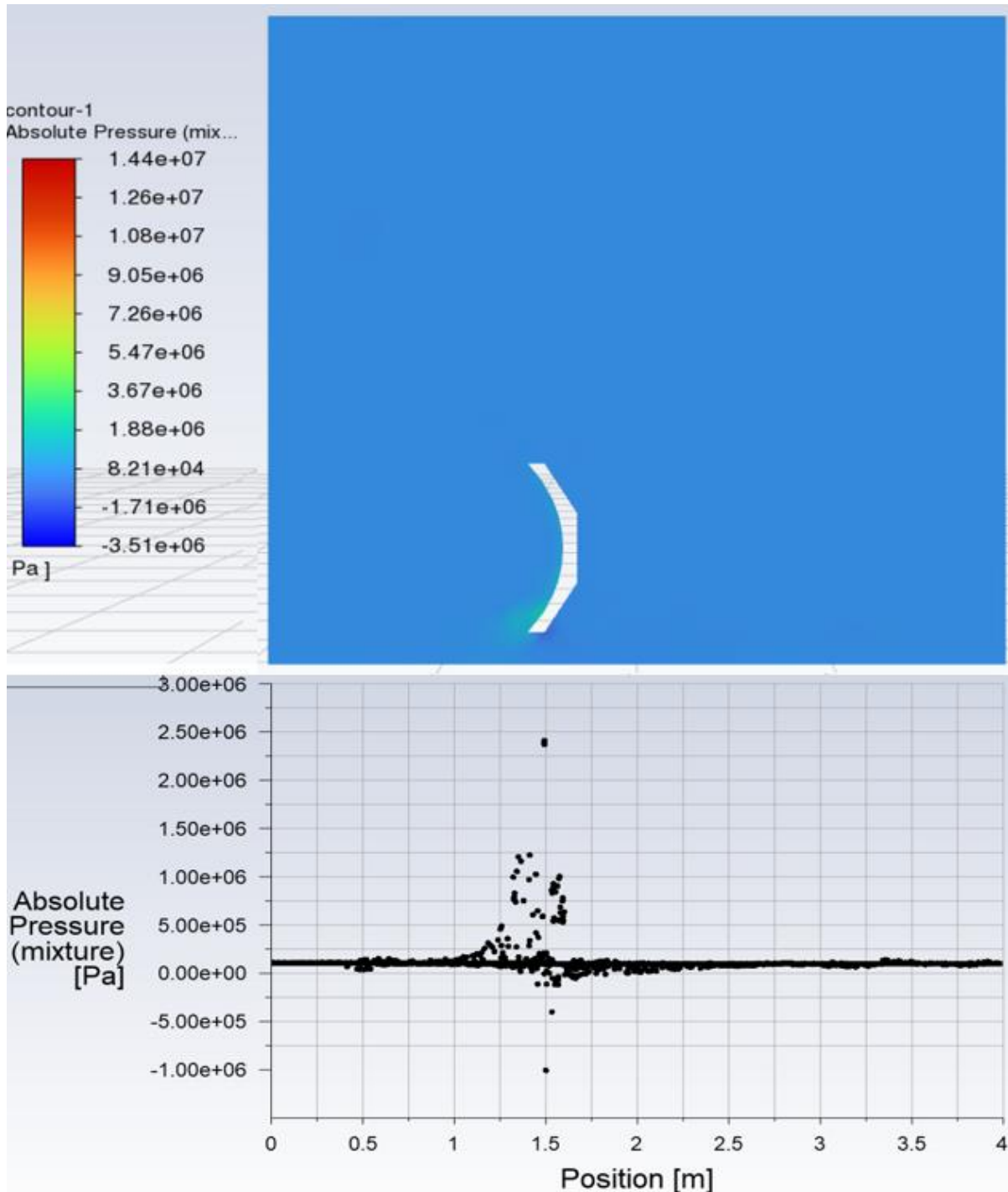
Figure 3.36: Design.9 absolute pressure contour (top) and plot (bottom)

Velocity distribution as a magnitude also is more evenly distributed behind the scoop, there are no longer as clear spikes in velocity points as in Design.8.
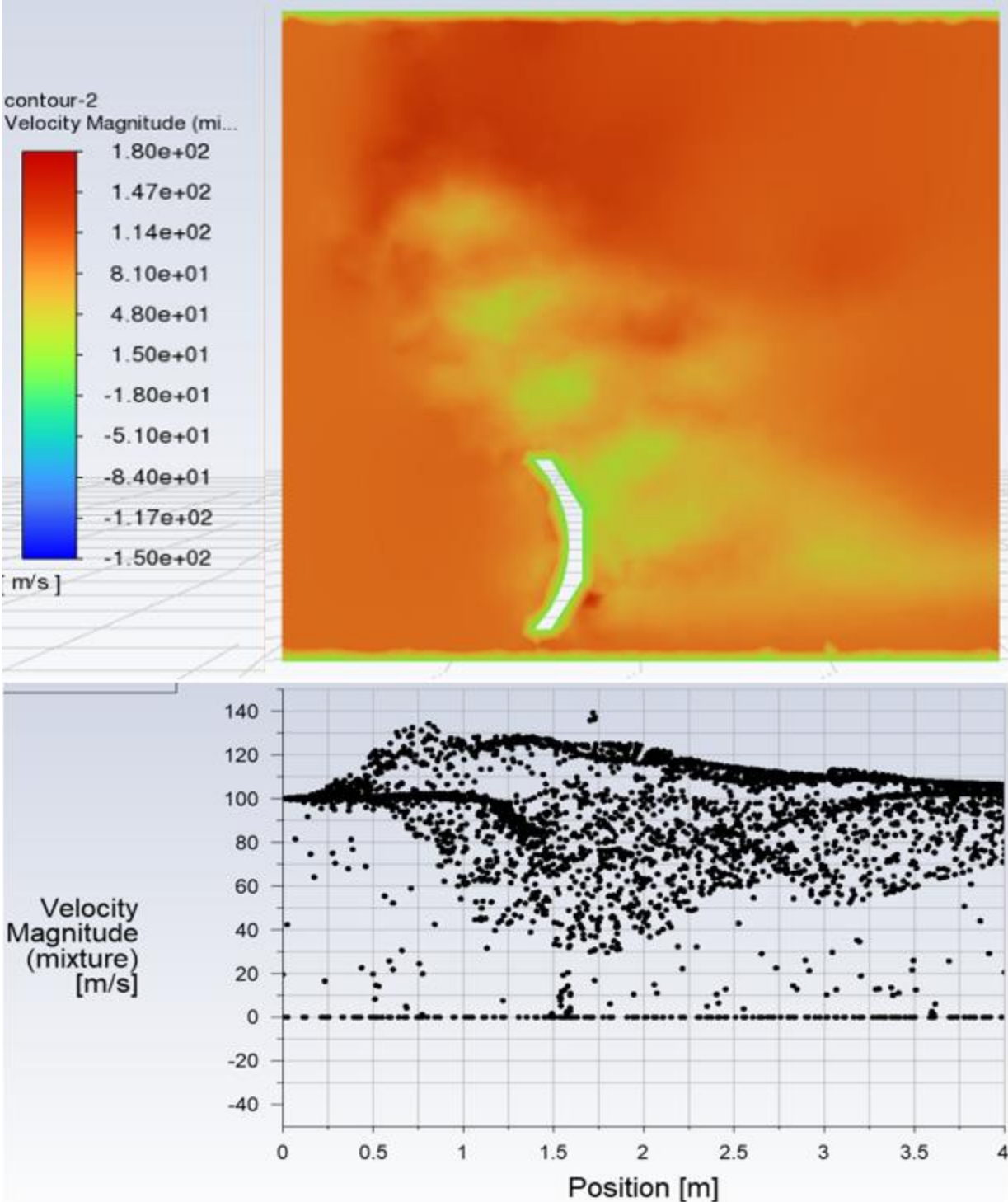
Figure 3.37: Design.9 velocity magnitude contour (top) and plot (bottom)
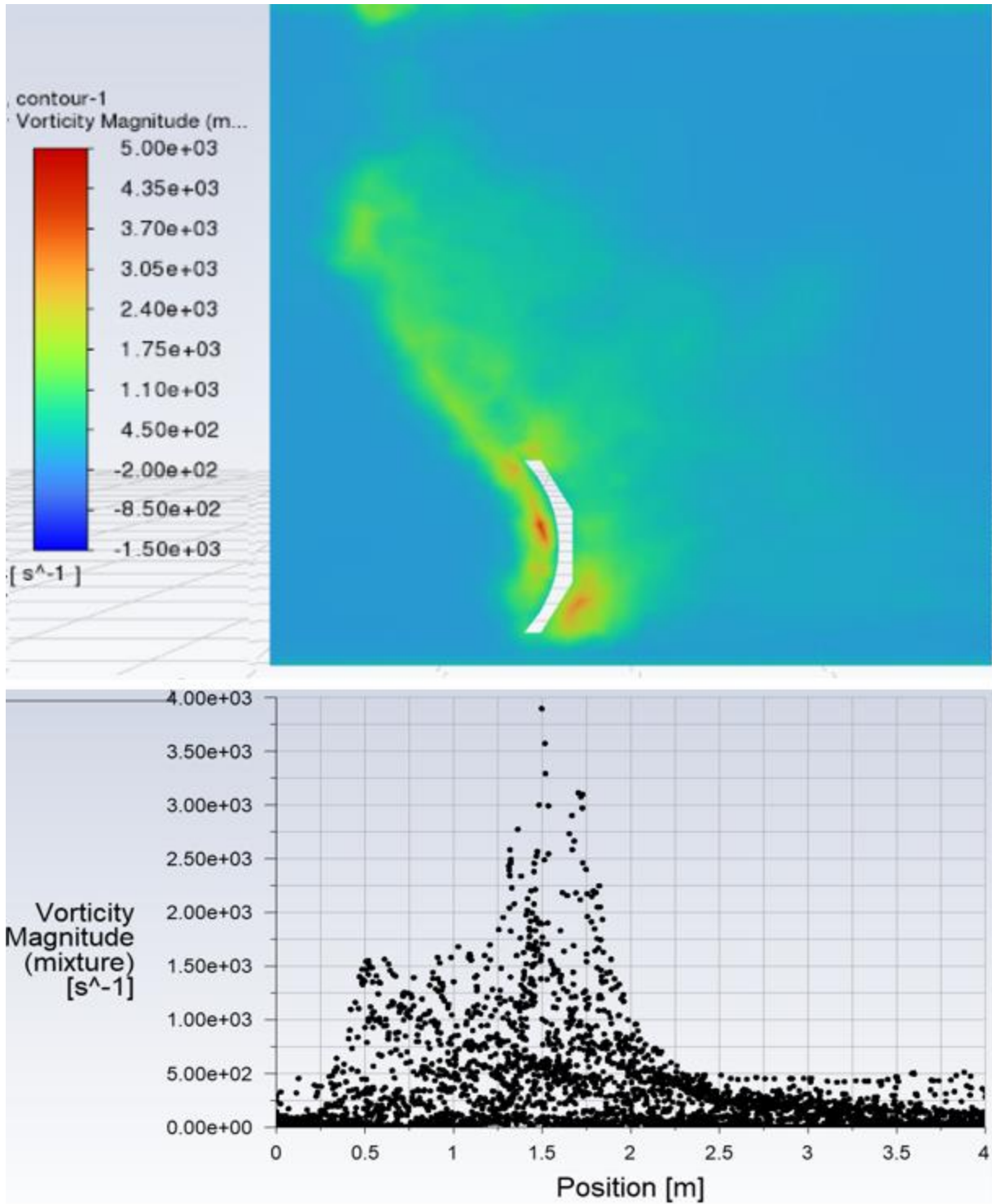
Figure 3.38: Design.9 vorticity magnitude contour (top) and plot (bottom)

Vorticity much like velocity has also been reduced behind the scoop, Figure 3.38. Previously highest points of vorticity by a noticeable margin were behind the bottom of the scoop.
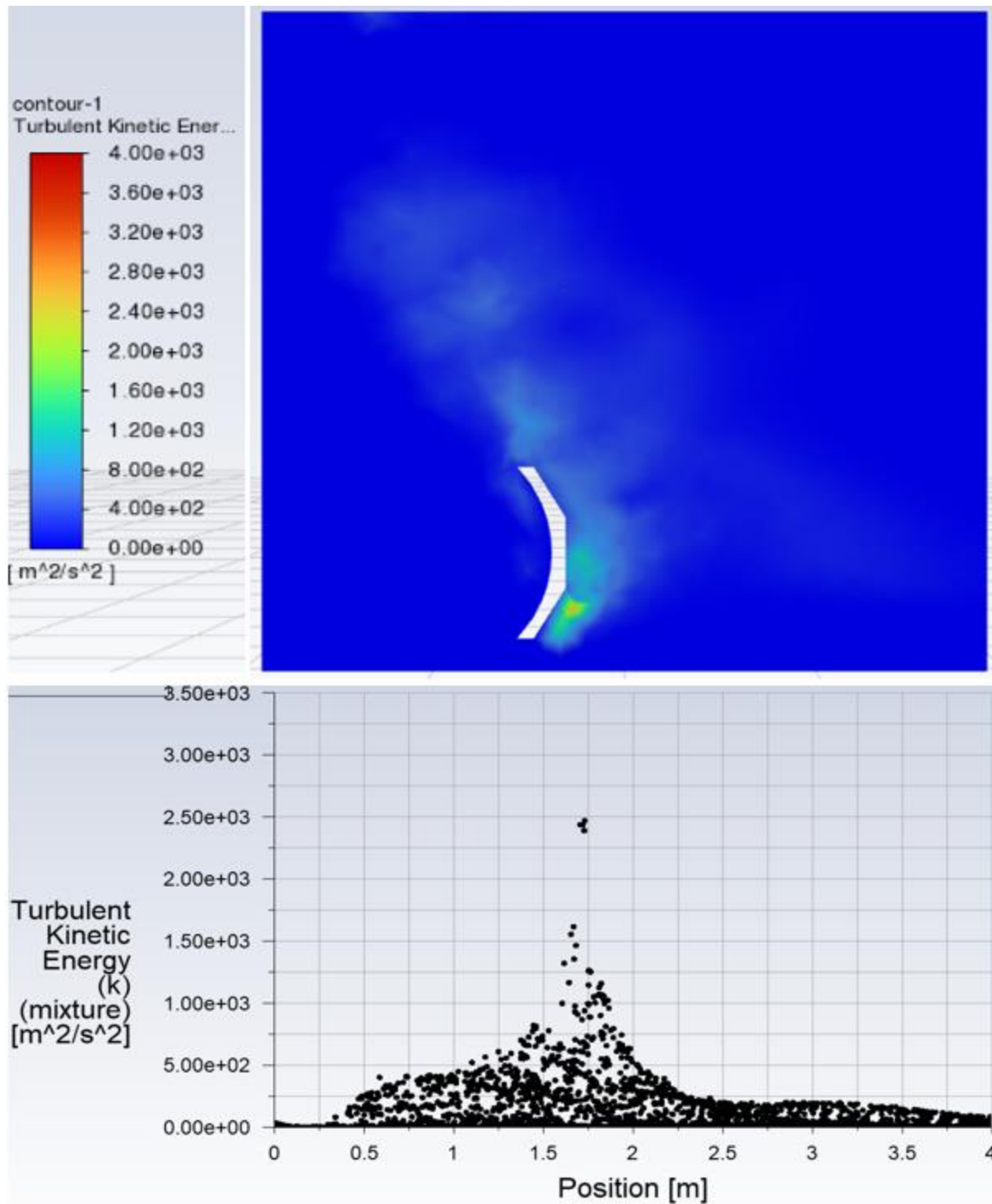
Figure 3.39: Design.9 turbulent kinetic energy contour (top) and plot (bottom)

In resemblance with velocity and vorticity, turbulent kinetic energy seems tamer, Figure 3.39, although still with a focus on the bottom of the scoop which is expected.
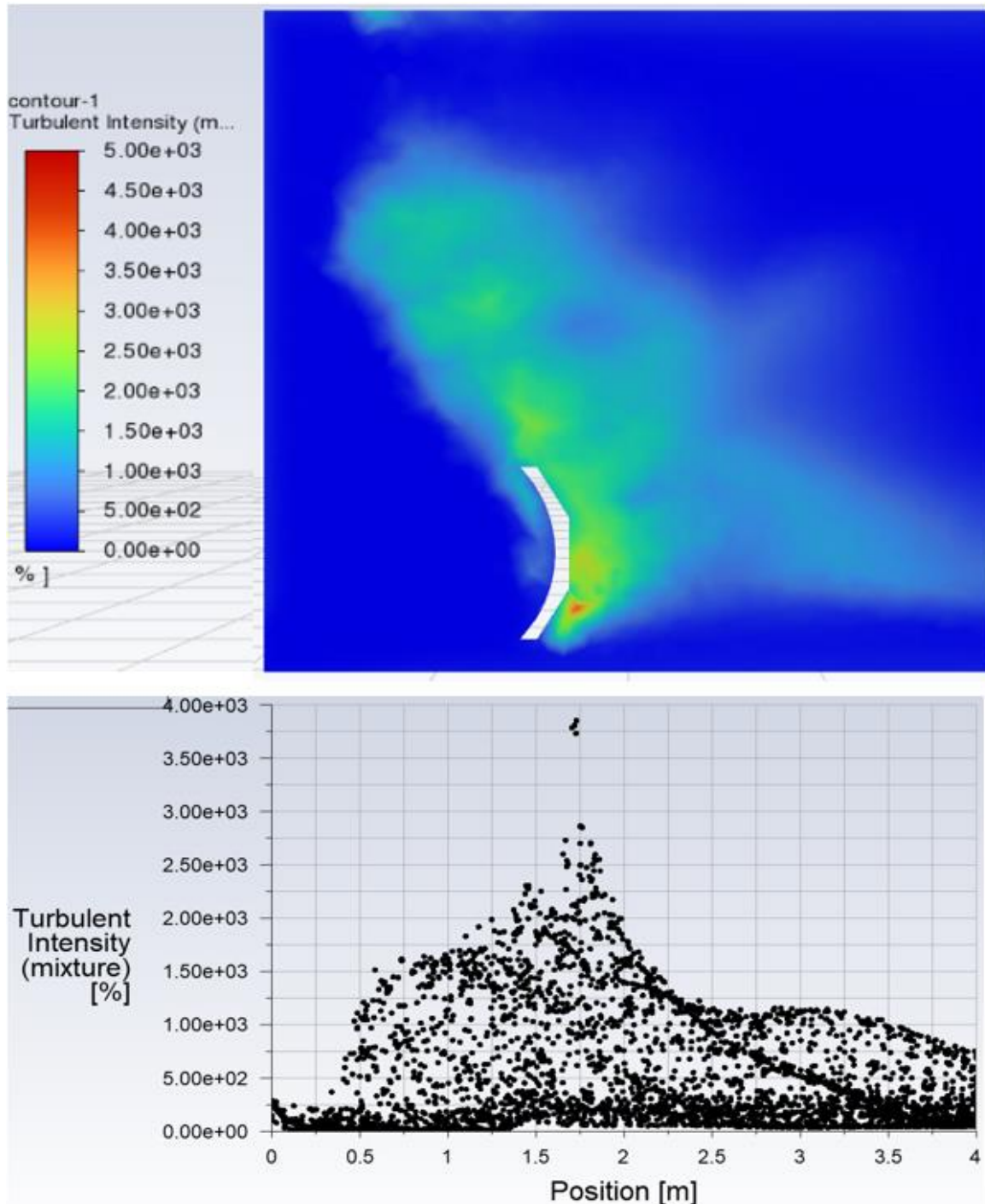
Figure 3.40: Design.9 turbulent intensity contour (top) and plot (bottom)

There is a sharp decline in the unsteadiness as shown in Figure 3.40 compared to previous designs with flat top scoop across. From about the 1.7-meter position to 2-meter position there is a sharp decline of turbulent intensity not seen in the others.
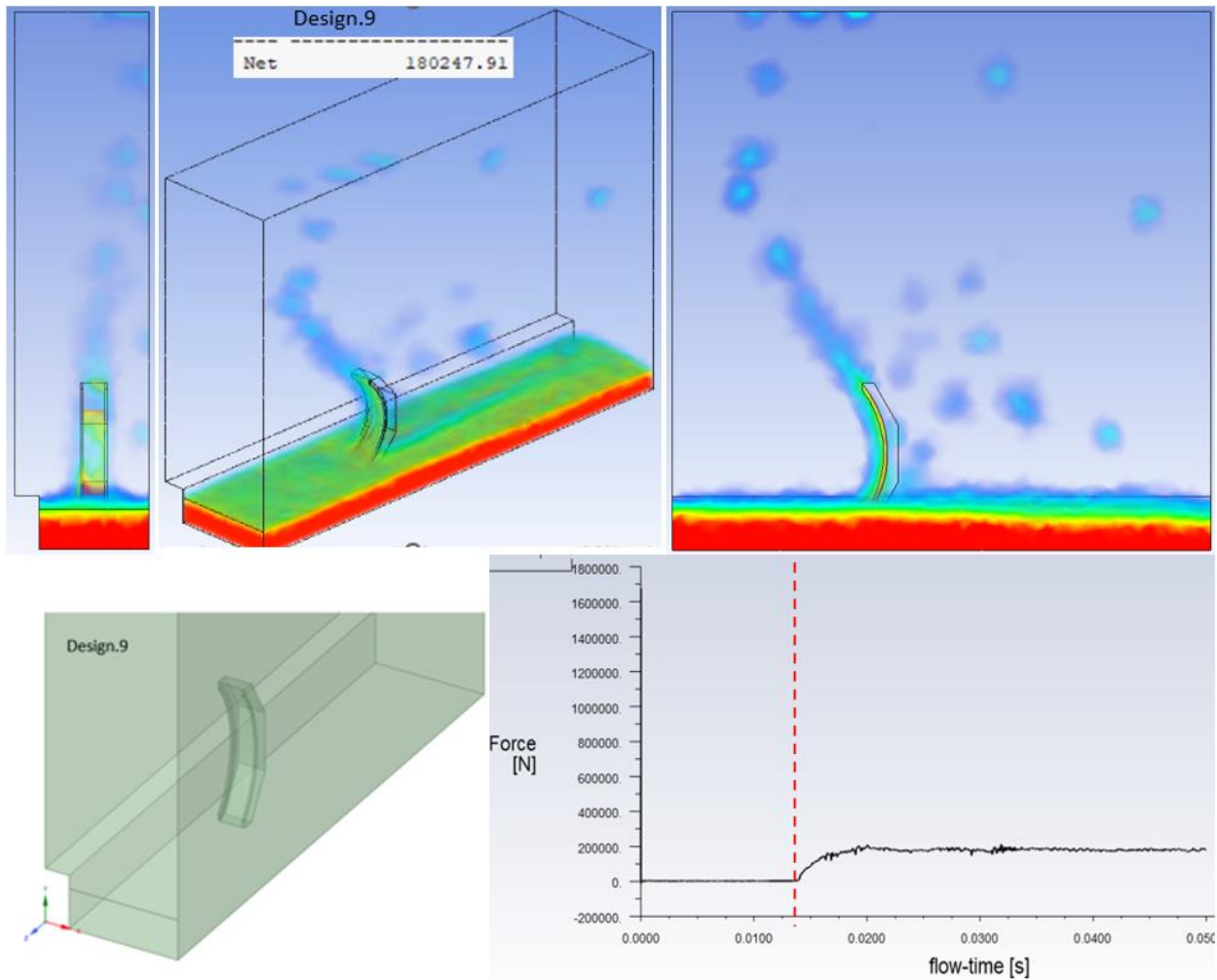
Figure 3.41: Design.9 water volumetric flow rate (top), isometric view (bottom left), and drag force plot (bottom right)
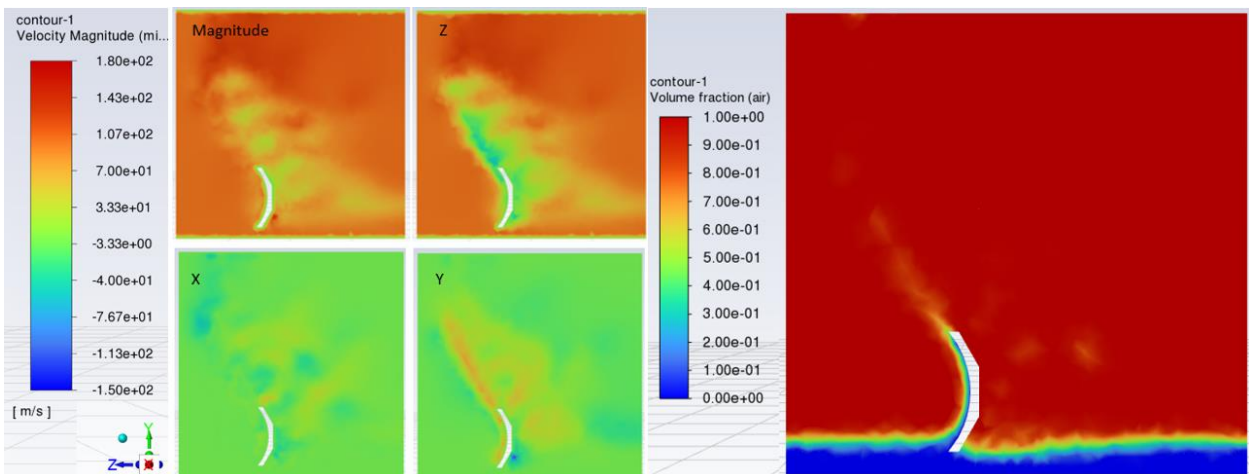
Figure 3.42: Design.9 velocity magnitude and in Z, X, and Y axis (left). Volume fraction of air in a plane through the middle of the domain (right)
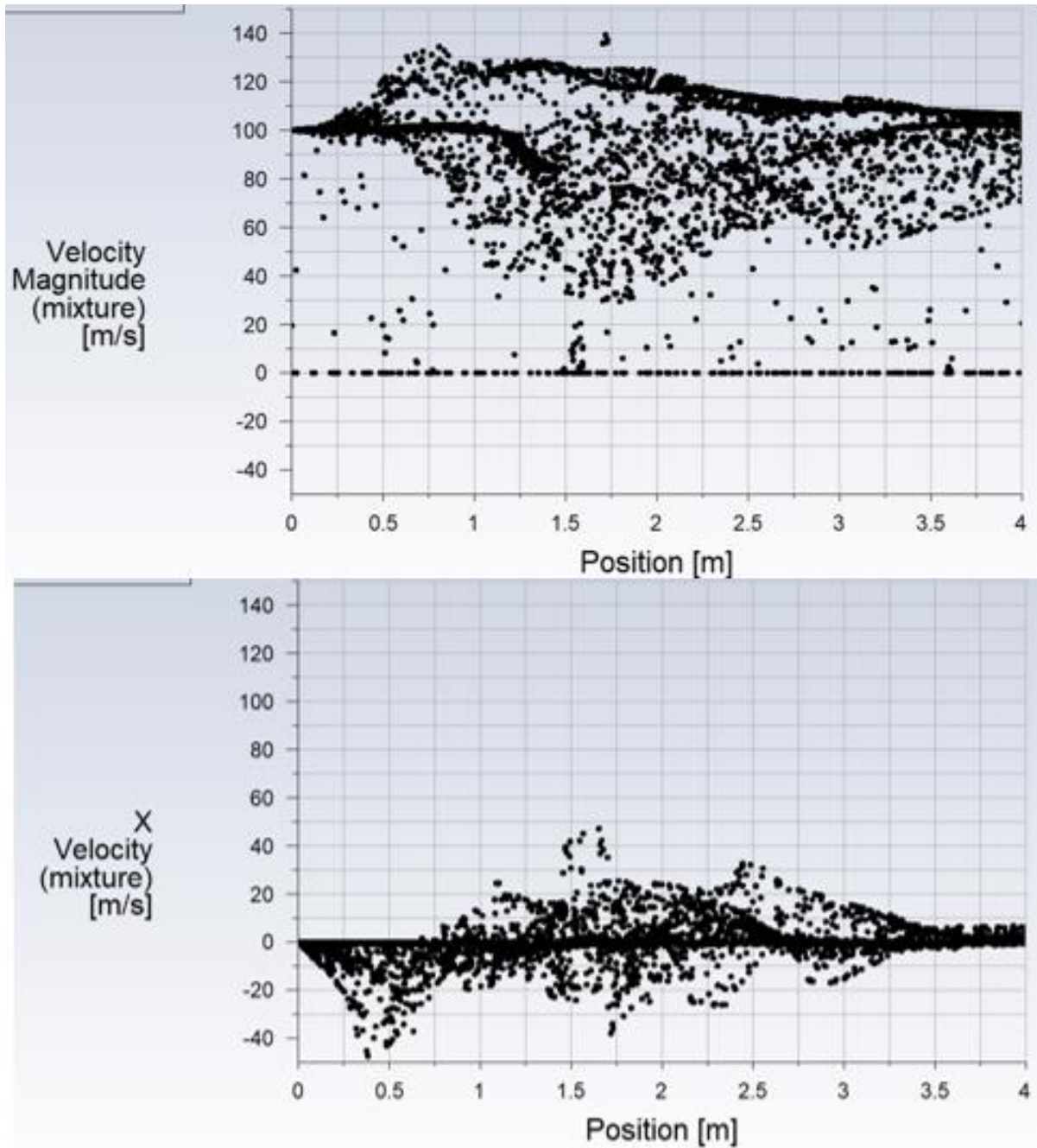
Plot 3.13: Design.9 velocity magnitude (top) and velocity in X-axis (bottom)
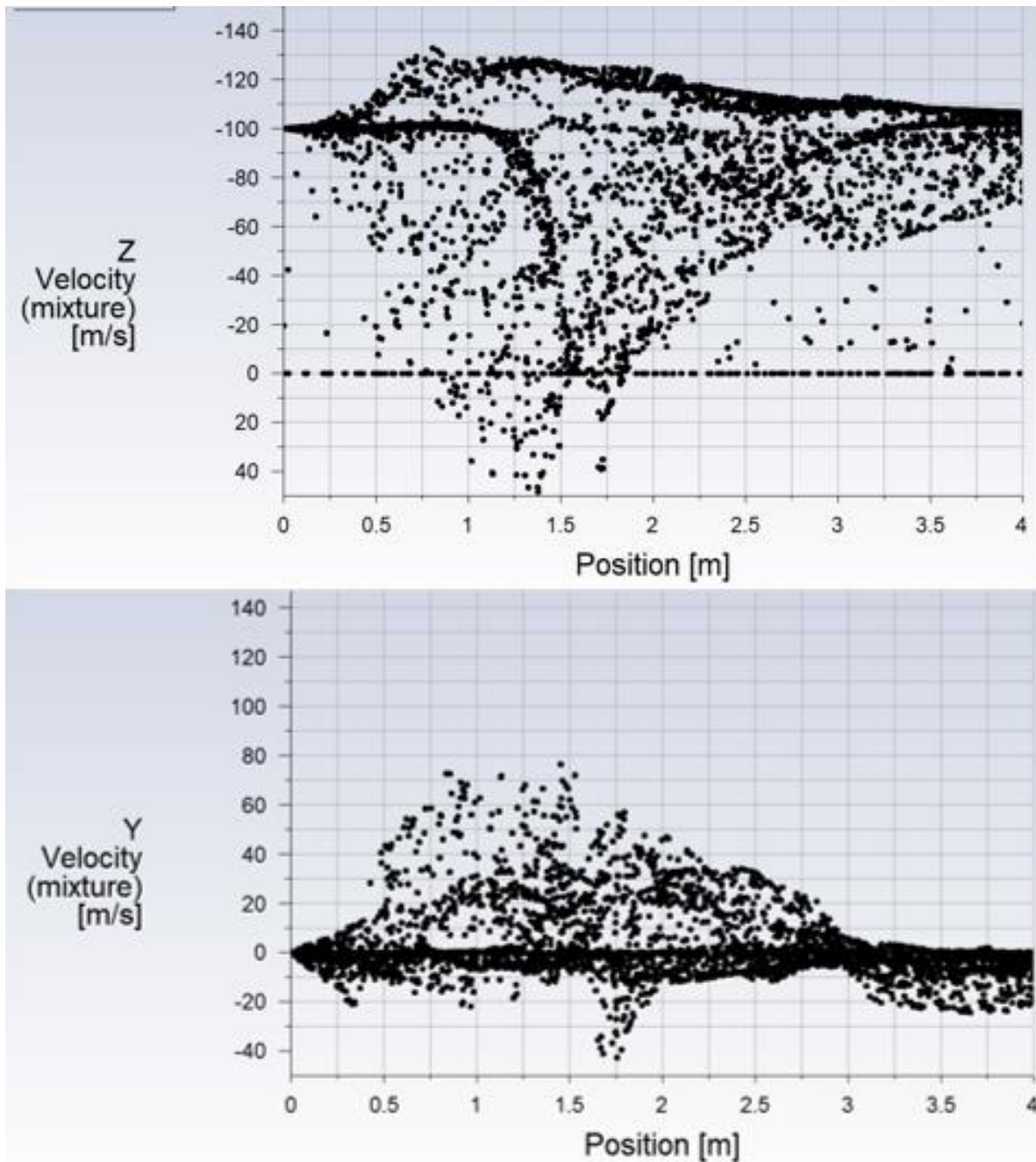
Plot 3.14: Design.9 velocity in Z-axis (top) and velocity in Y-axis (bottom)
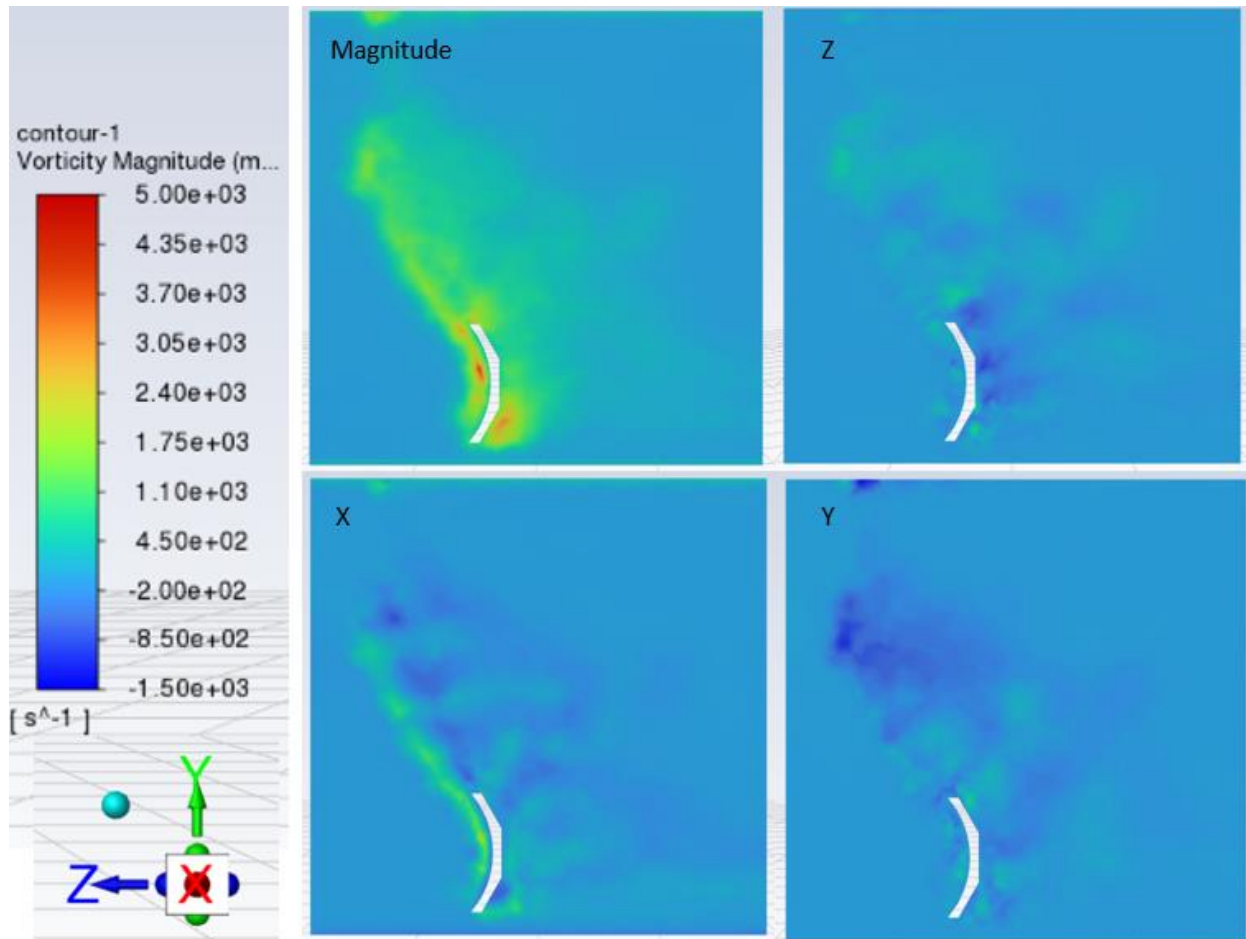
Figure 3.43: Design.9 vorticity magnitude and in Z, X, and Y axis (left). Volume fraction of air in a plane through the middle of the domain (right)
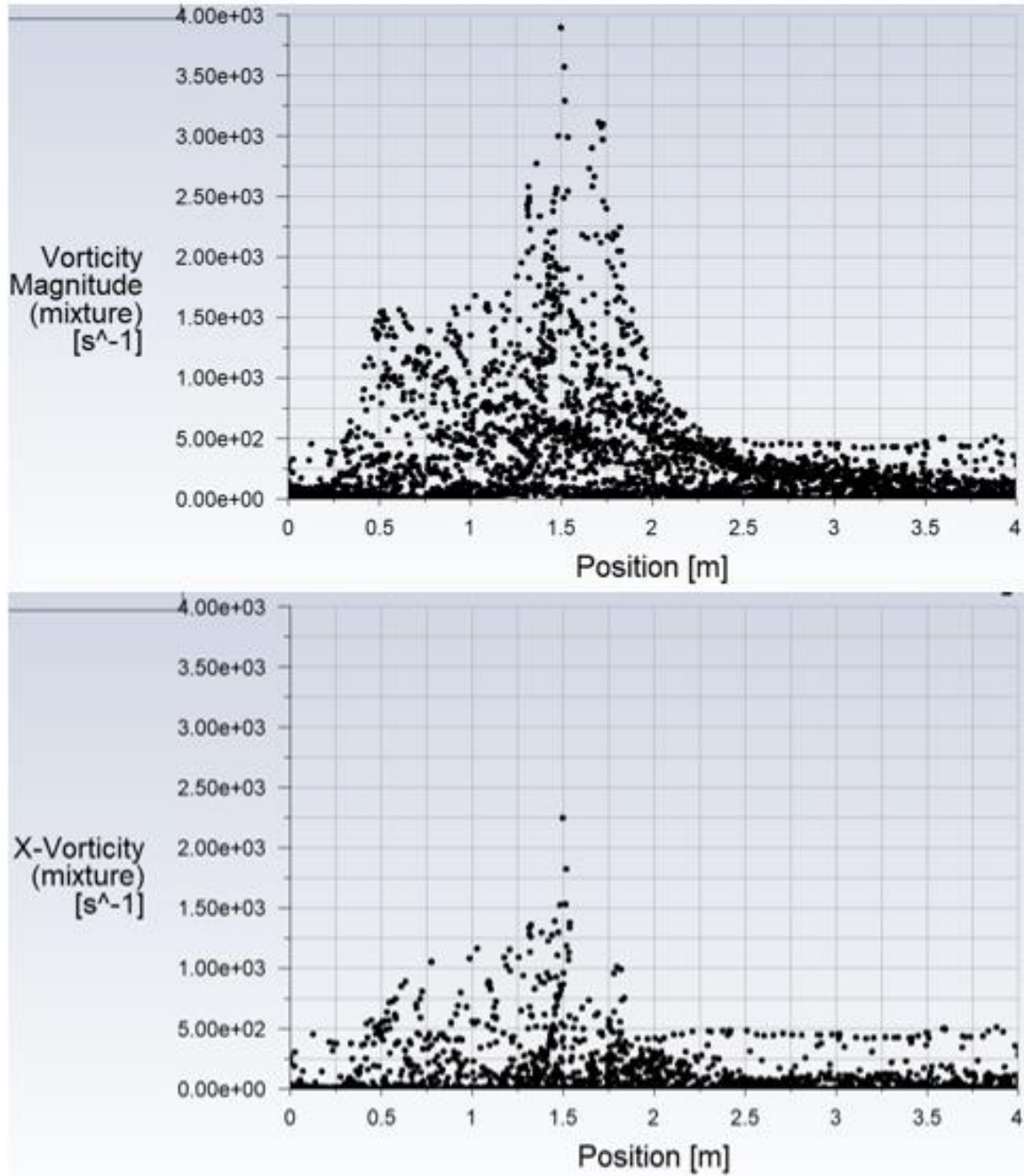
Plot 3.15: Design.9 vorticity magnitude (top) and vorticity in X-axis (bottom)
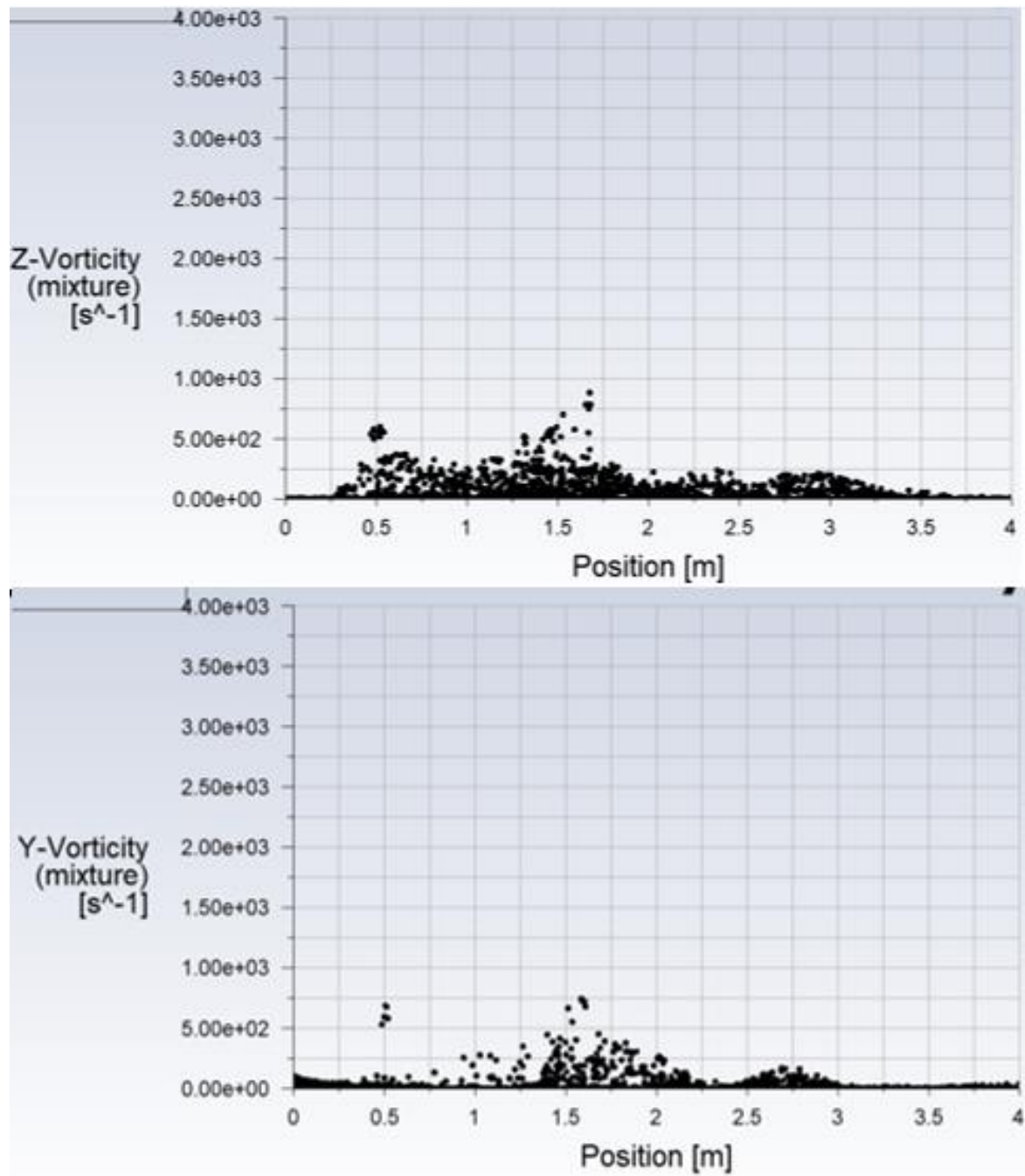
Plot 3.16: Design.9 vorticity in Z-axis (top) and vorticity in Y-axis (bottom)
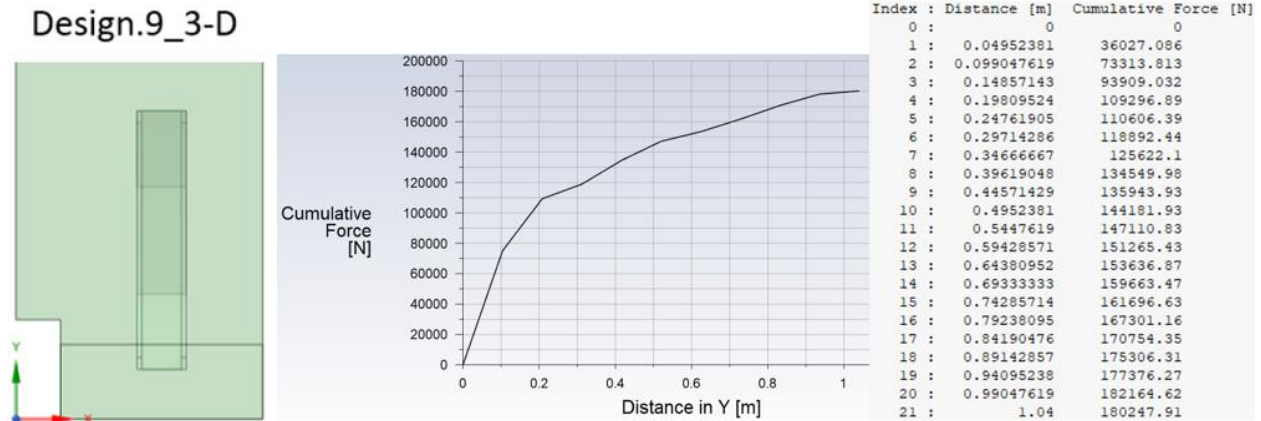
Plot 3.17: Design.9 drag force by scoop height

Force on the scoop was about 180kN, so about the same as Design.8. The marked difference between the two is the flow behavior behind and past the scoop. As pusher sled is completely integrated along with the scoop it will be an important consideration. Looking at the water volumetric flow rate in Figure 3.41 the flow of the water is substantially different from Design.7 and Design.8. Vorticity is lower in all axis, Figure 3.43, Plot 3.15, and Plot 3.16. In the force distribution by height in Plot 3.17 it can also be observed that that there is no longer a drop in Force in the last 0.05 meters.

3.3.2.5 Design.10 at 100 m/s

For Design.10 the flow at the bottom front of the scoop is studied by cutting it into a "v". Additionally, the top back part of the scoop is once again flat as in Design.8. These changes are for two reasons.

1) Though it is known that the drag force will be reduced due to less contact area with the water, quantifying it and knowing by how much is important in the design of an optimal scoop in which tradeoffs will be made.

2) The scoop is just part of the pusher sled, observing and understanding how it will affect the fluid flow behind it is important to consider water braking in context of the entire sled.

The top back part of the scoop seems to cause a drop of force on the scoop, further testing it will validate the hypothesis.
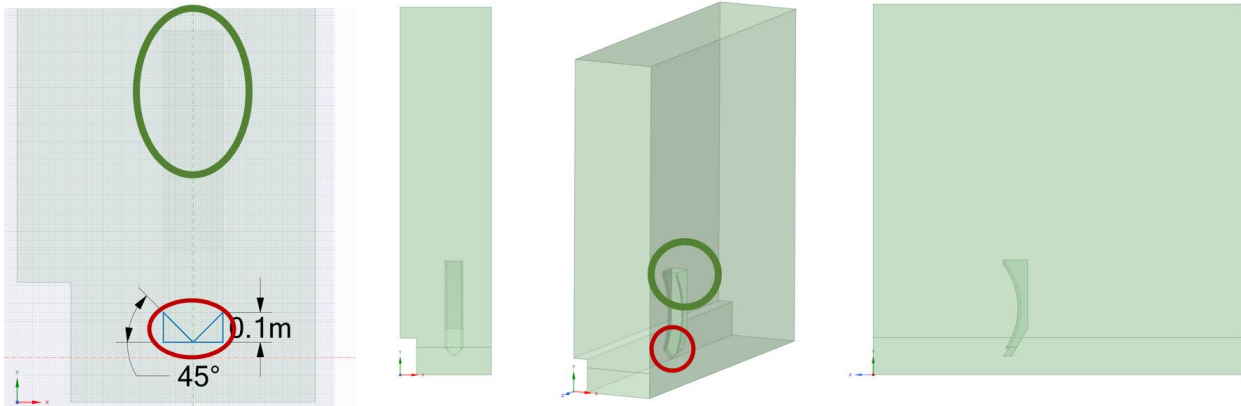
Figure 3.44: Design10 geometry changes and views from changes made from Design.9

As seen in Figure 3.44, the "v" cut in the front bottom of the scoop will be at 45-degree angles. As in previous sections mesh and design statistics are provided in Table 3.10 and Table 3.11.

Table 3.10: Statistics of Design.9 mesh

Bounding Box	
Length X	1. m
Length Y	4. m
Length Z	4. m
Properties	
Volume	15.689 m³
Centroid X	0.50739 m
Centroid Y	2.0348 m
Centroid Z	-2.0006 m
Statistics	
Nodes	16682
Elements	84052
Mesh Metric	None
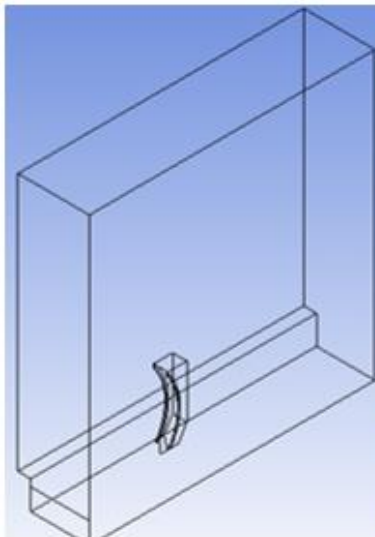
Design.10_3-D
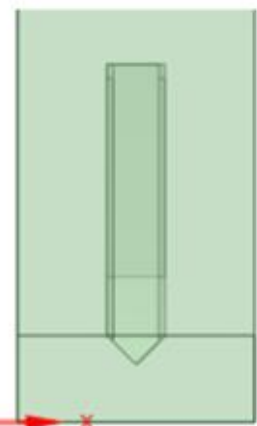
Table 3.11: Statistics of Design.10 boundaries

Object Name	air_inlet	water_inlet	walls	back_outlet	scoop_walls
State					
Scoping Method					
Geometry	1 Face		6 Faces	1 Face	2 Faces
Send to Solver					
Protected					
Visible					
Program Controlled Inflation					
Type					
Total Selection	1 Face		6 Faces	1 Face	2 Faces
Surface Area	3.682 m²	0.246 m²	40. m²	3.928 m²	0.27261 m²
Suppressed					
Used by Mesh Worksheet					

Object Name	scoop_front.mid.arcs_walls	scoop_back.bottom_walls	scoop_back.top_walls	scoop_front.arc.mid.sides_walls	scoop_front.top_walls
State	Fully Defined				
Scope					
Scoping Method	Geometry Selection				
Geometry	3 Faces			2 Faces	
Definition					
Send to Solver	Yes				
Protected	Program Controlled				
Visible	Yes				
Program Controlled Inflation	Exclude				
Statistics					
Type	Manual				
Total Selection	3 Faces			2 Faces	
Surface Area	0.21145 m²	8.3761e-002 m²	0.20068 m²	6.0031e-002 m²	1.9027e-003 m²
Suppressed	0				
Used by Mesh Worksheet	No				

Initial look at pressure data, Figure 3.45, confirms expected drop from geometric change of reducing the contact area between the scoop and water. In every metric from Figure 3.46 to Figure 3.48 there is a clear qualitative and quantitative reduction. The only exception is turbulent intensity in Figure 3.49. Design.10 from the data has more unsteadiness behind the scoop.
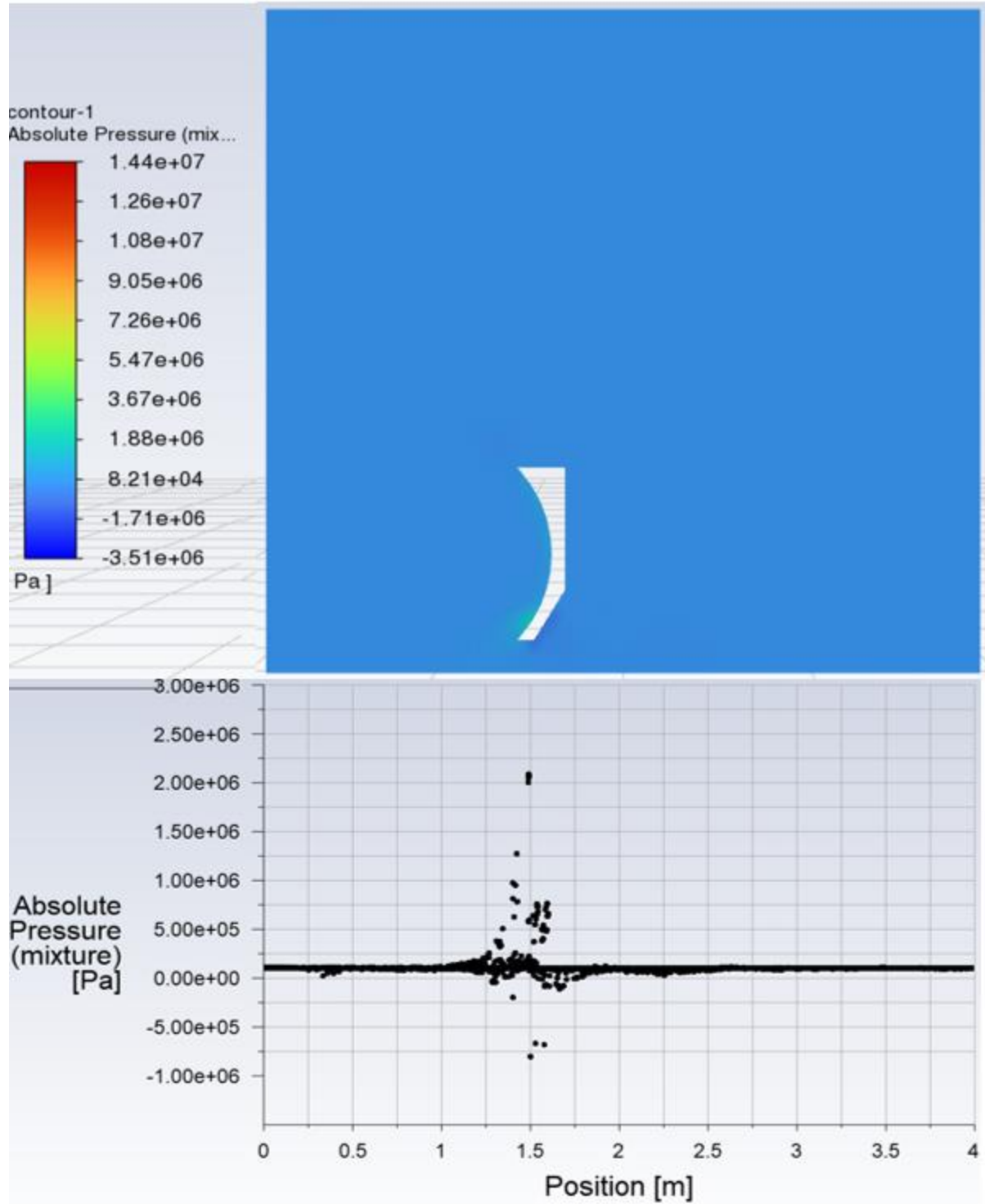
Figure 3.45: Design.10 absolute pressure contour (top) and plot (bottom)
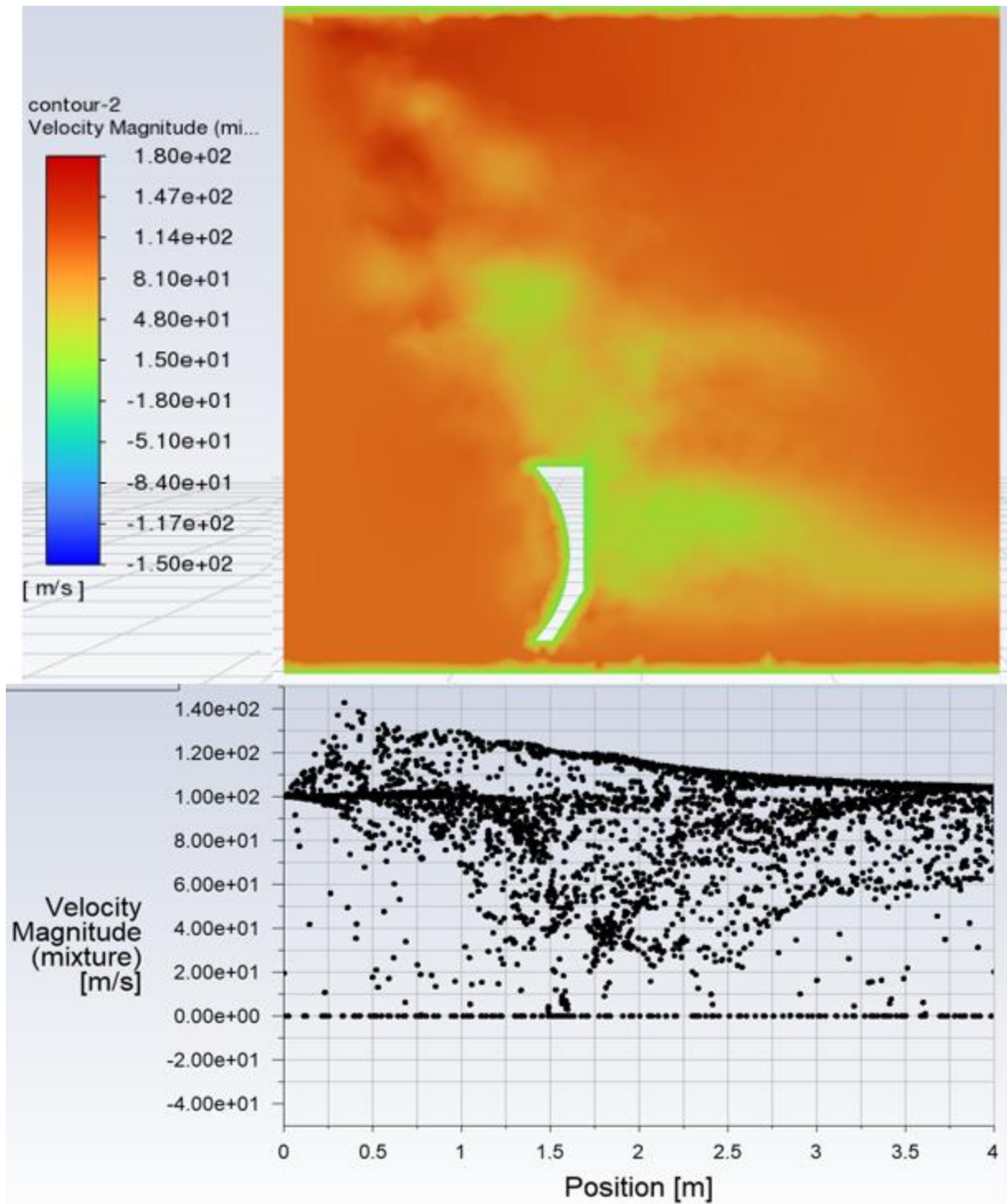
Figure 3.46: Design.10 velocity magnitude contour (top) and plot (bottom)
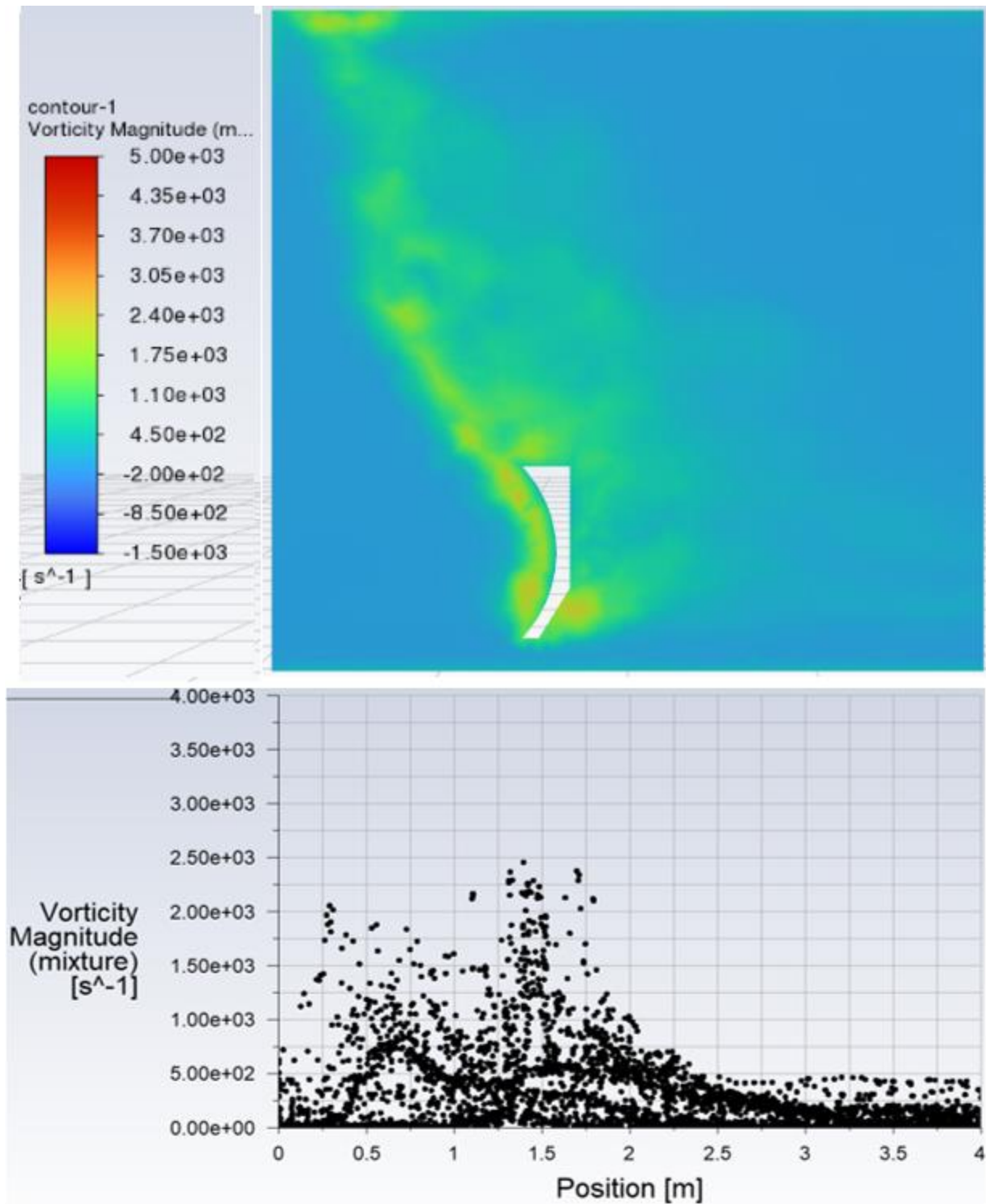
Figure 3.47: Design.10 vorticity magnitude contour (top) and plot (bottom)
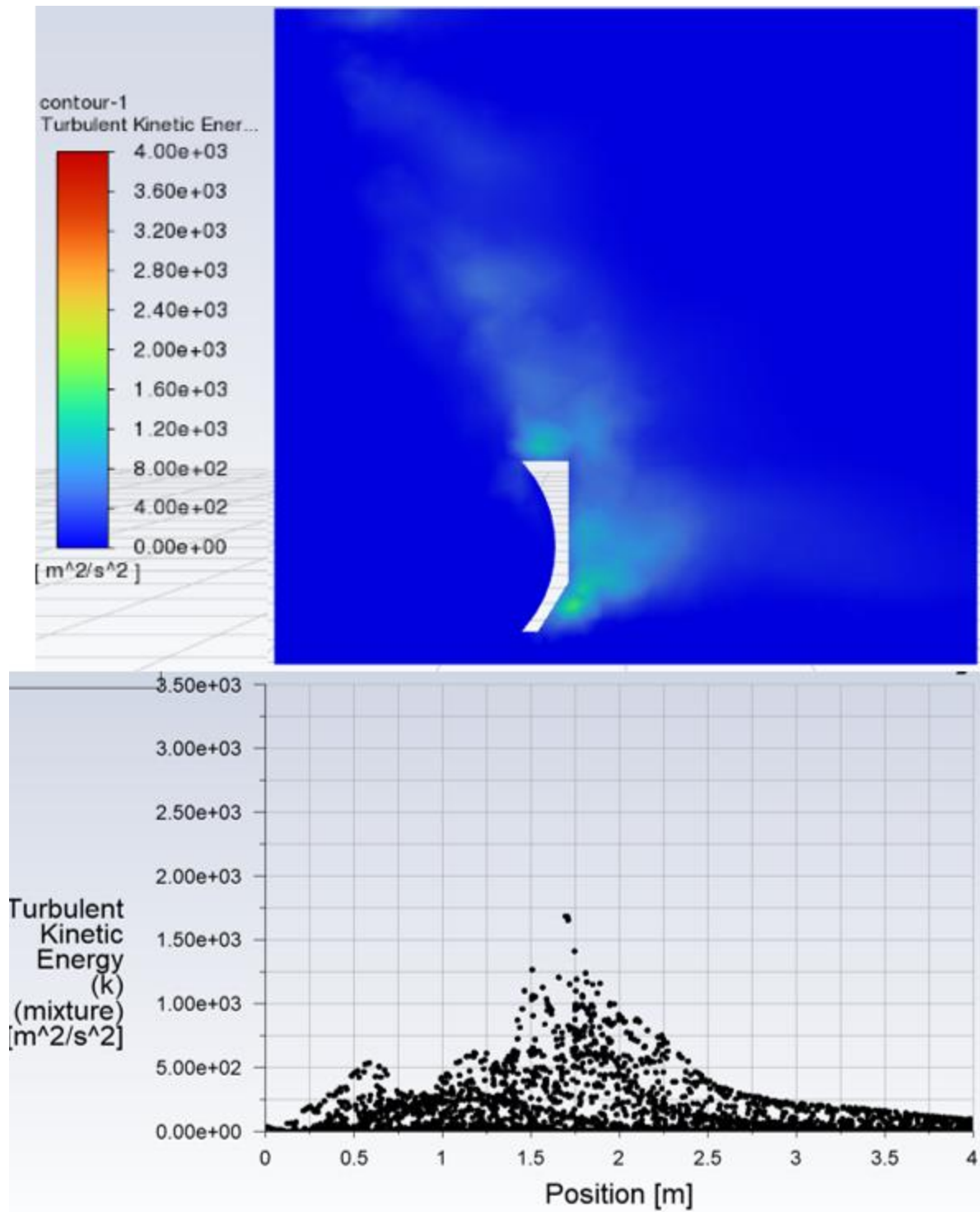
Figure 3.48: Design.10 turbulent kinetic energy contour (top) and plot (bottom)

90
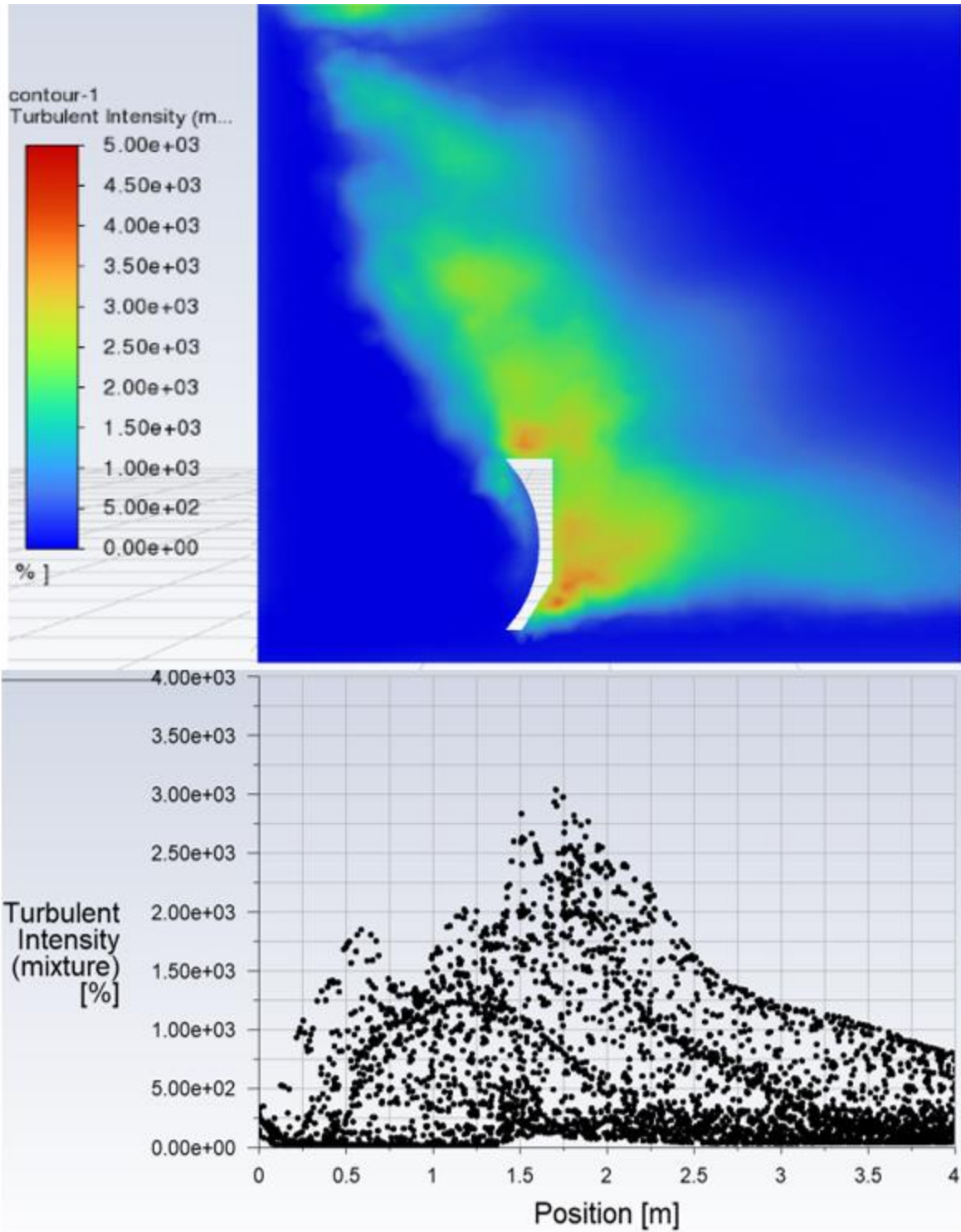
Figure 3.49: Design.10 turbulent intensity contour (top) and plot (bottom)
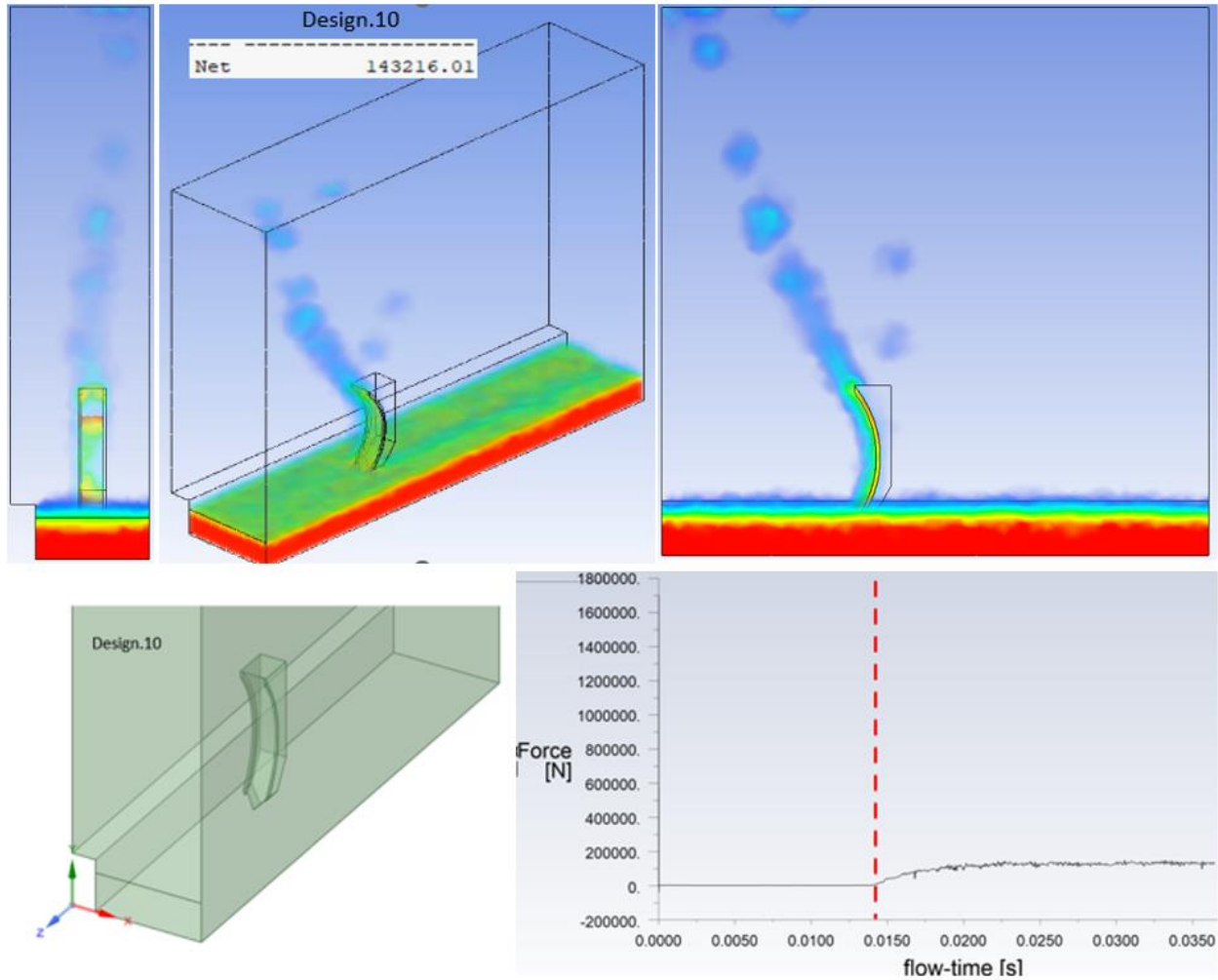
Figure 3.50: Design.10 water volumetric flow rate (top), isometric view (bottom left), and drag force plot (bottom right)
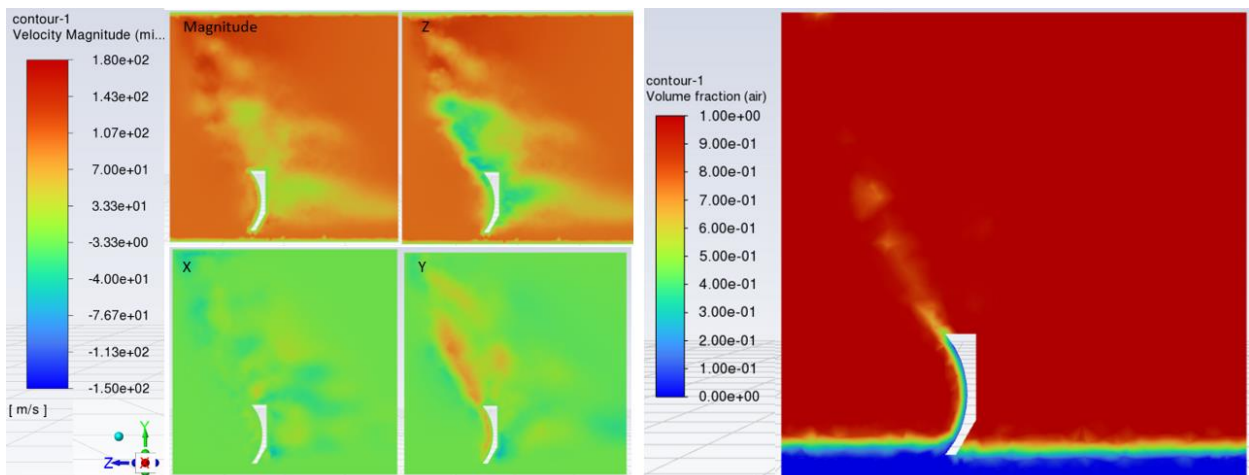
Figure 3.51: Design.10 velocity magnitude and in Z, X, and Y axis (left). Volume fraction of air in a plane through the middle of the domain (right)

92
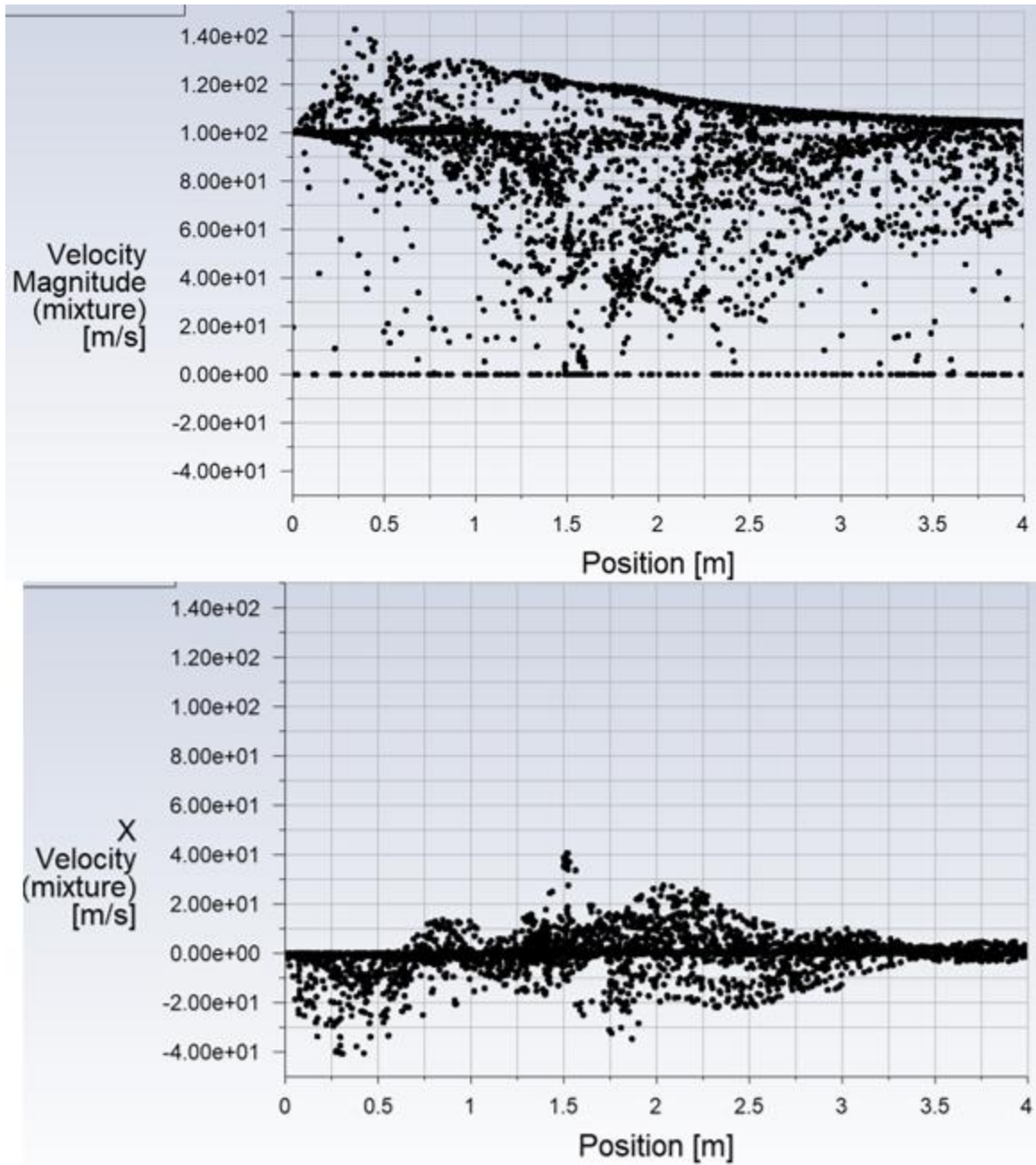
Plot 3.18: Design.10 velocity magnitude (top) and velocity in X-axis (bottom)
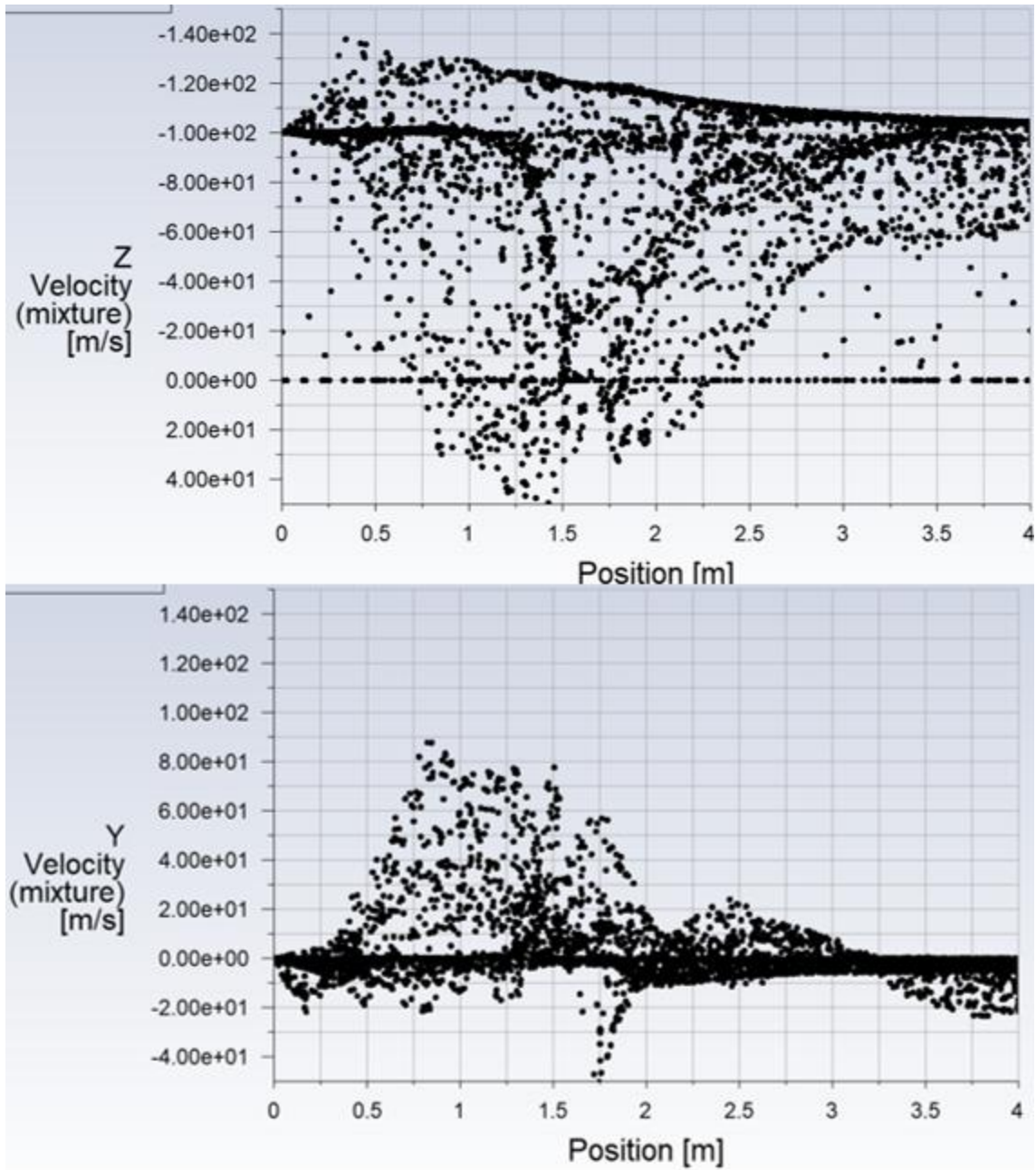
Plot 3.19: Design.10 velocity in Z-axis (top) and velocity in Y-axis (bottom)
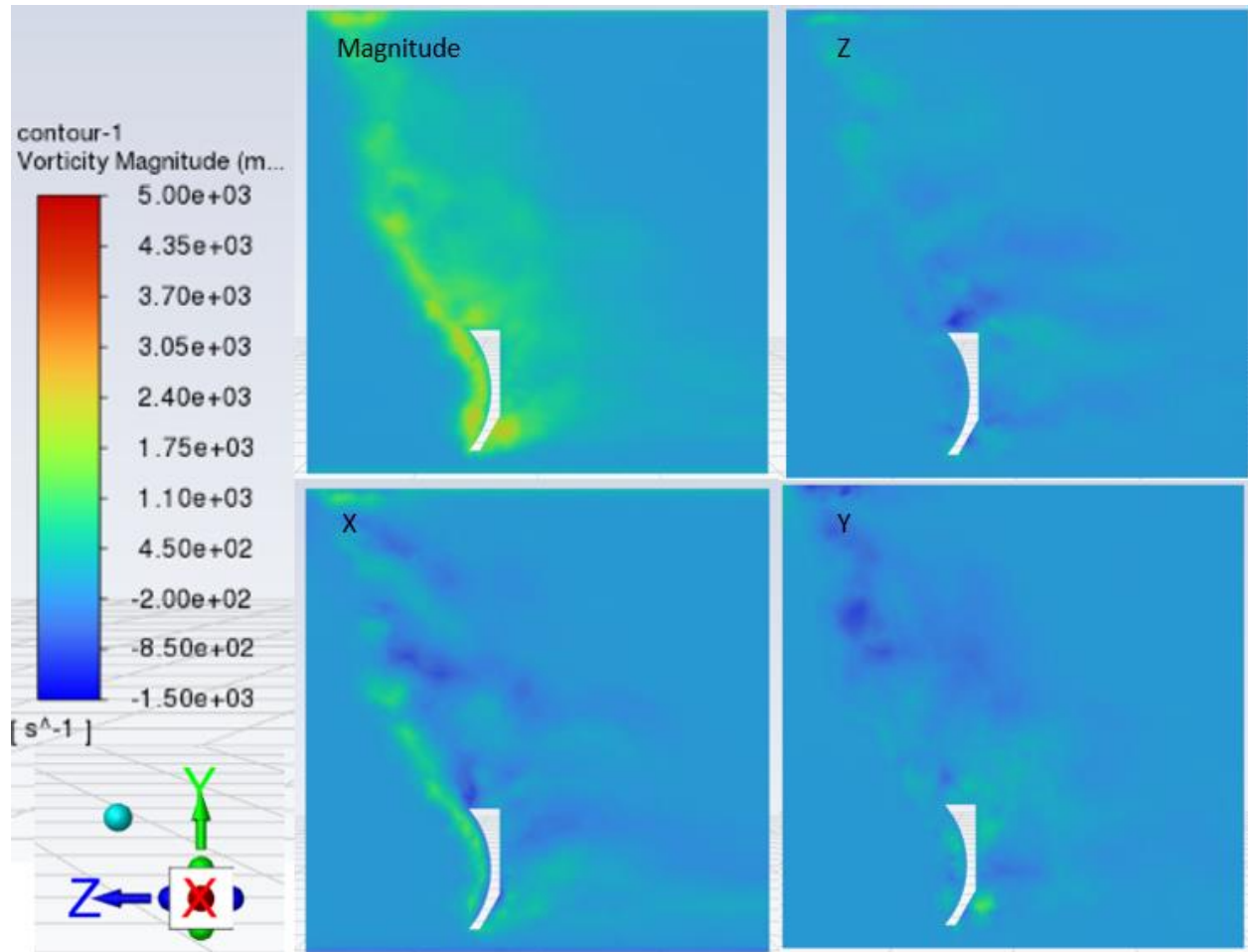
Figure 3.52: Design.10 vorticity magnitude and in Z, X, and Y axis (left). Volume fraction of air in a plane through the middle of the domain (right)
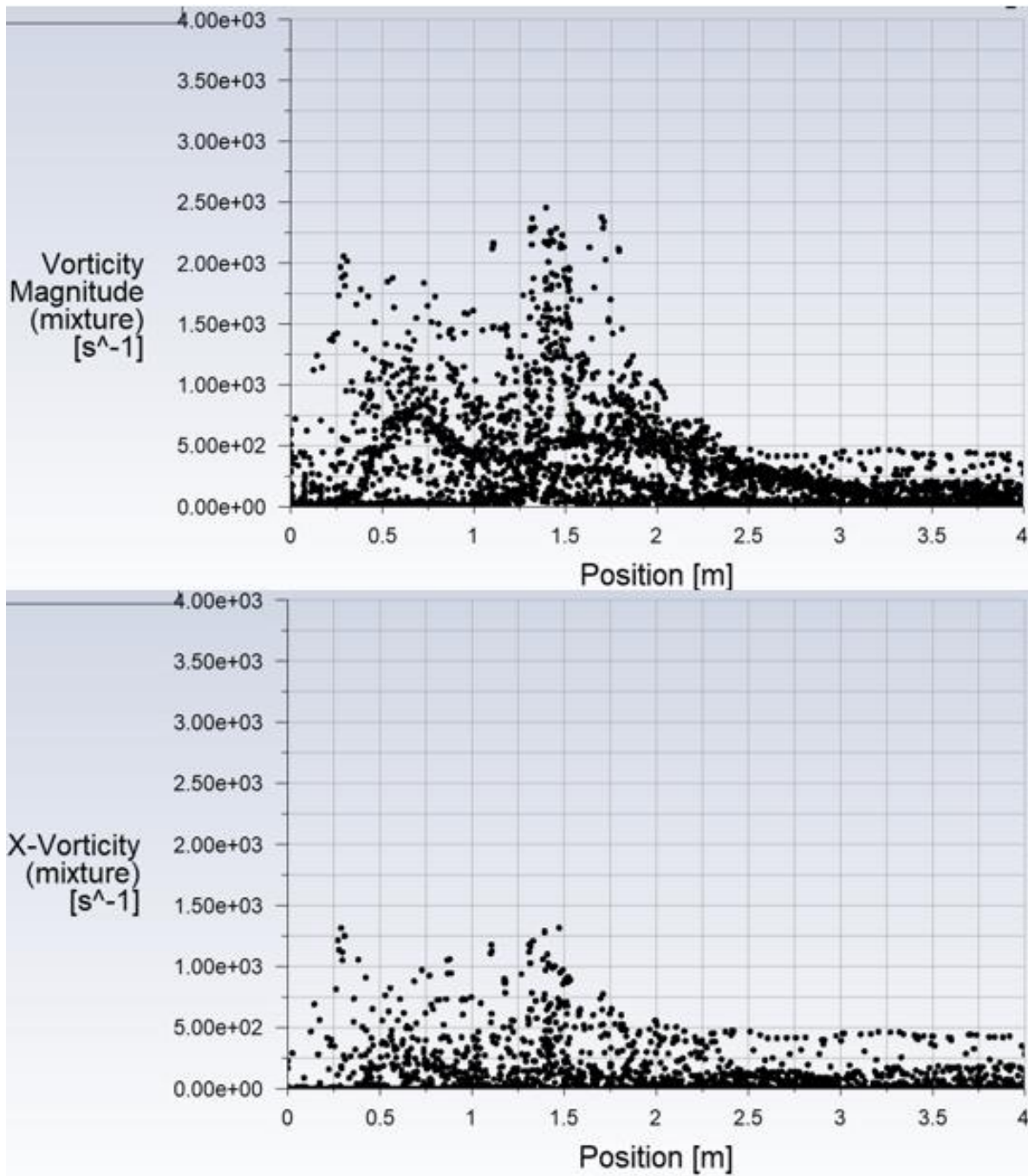
Plot 3.20: Design.10 vorticity magnitude (top) and vorticity in X-axis (bottom)
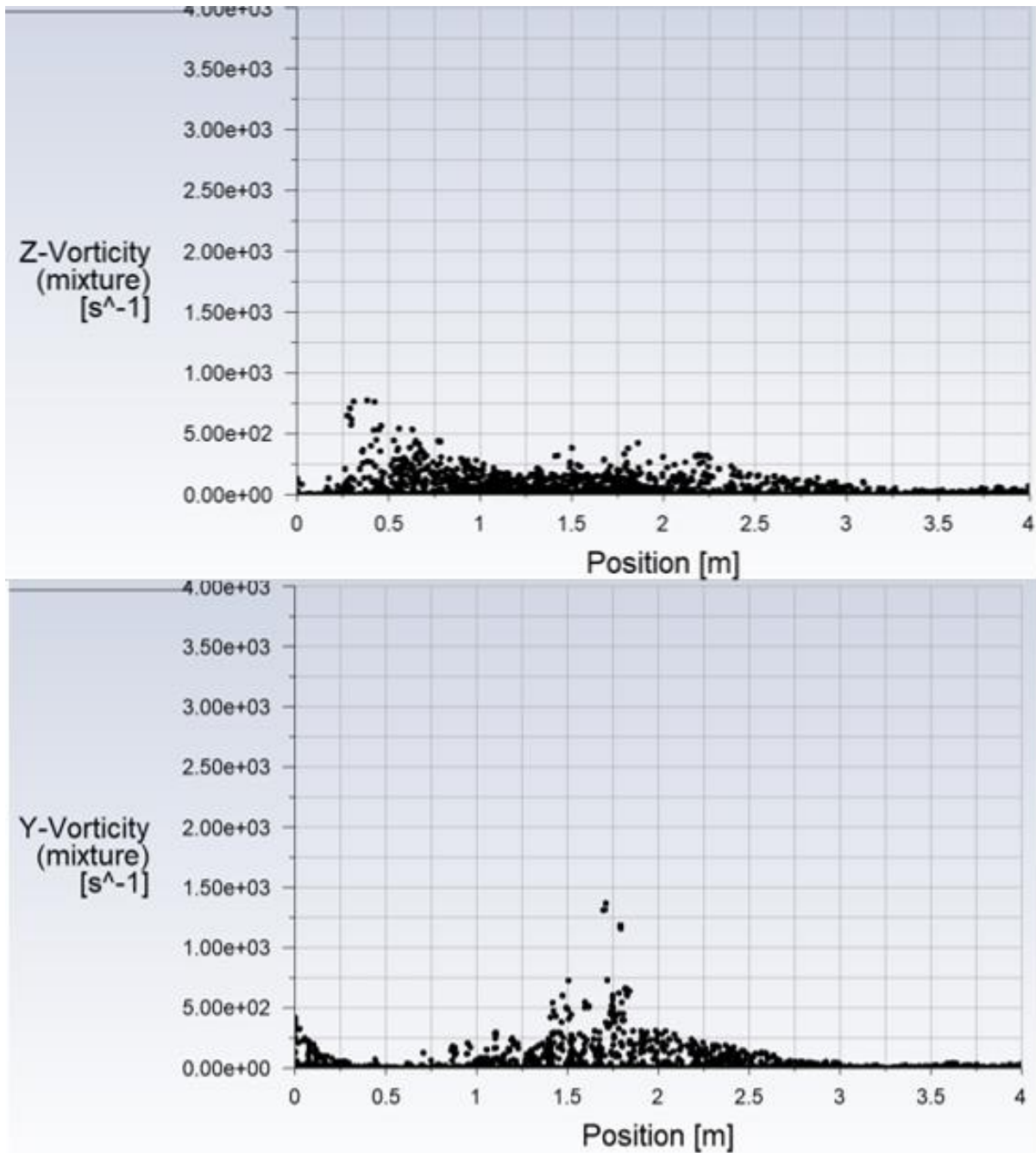
Plot 3.21: Design.10 vorticity in Z-axis (top) and vorticity in Y-axis (bottom)
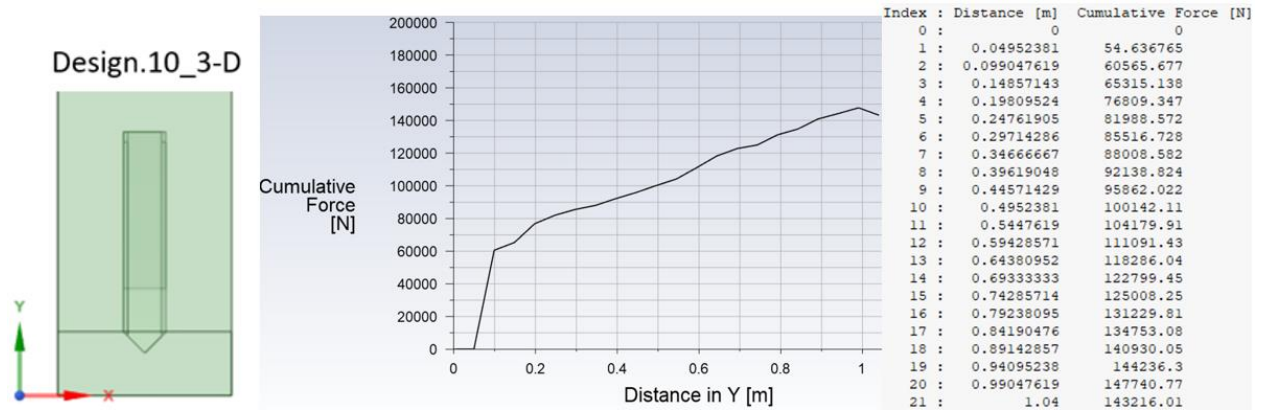
Plot 3.22: Design.10 drag force by scoop height

Force on the scoop was about 143kN, so about the same as Design.6. This demonstrates that the guard rails are a significant boost to water drag as water contacting a little more than half the area in Design.10 as in Design.6 has about 2.8% more force, 143kN to 139kN. Hand calculation validation at 0.1-meter height of scoop produces about 50kN compared to computational 60kN. The major difference in the calculation being the area estimate in the hand calculation. A drop from 1 meter to 1.04 meters in Plot 3.22 suggests that a flat top does have a reduction effect on the drag force acting on the scoop.

Careful consideration from analyzing the entire dataset available for Design.10 suggests that there is little benefit in adopting the "v" geometric design for increased drag. It reduces drag considerably from all designs apart from Design.6 and fluid flow behind the scoop will not generate any additional drag from water flow interaction behind the scoop. The only reason for consideration would be address issues beyond drag such as lift and less chaotic flow that may damage pusher sled attached to scoop.

Next is an analysis of Design.9 that did not fully converge at 300 m/s but it did enough to get a glimpse of fluid flow at near Mach speed. Final design recommendations and design uses will be made in Conclusion section.

98

3.3.2.6 Design.9 at 300 m/s

Out of all the designs that were simulated at 300 m/s all failed to converge completely. Design.9 water flow however managed to make it past the scoop, see Figure 3.53. There is an increased intensity in the flow viewed by the split of the water behind the scoop not as defined in the 100 m/s simulation. Also, there is a hydraulic jump in right contour of Figure 3.53 that provides insight as to the behavior of water at higher speeds.

Figure 3.53: Design.9 volumetric flow rate of water at 300 m/s
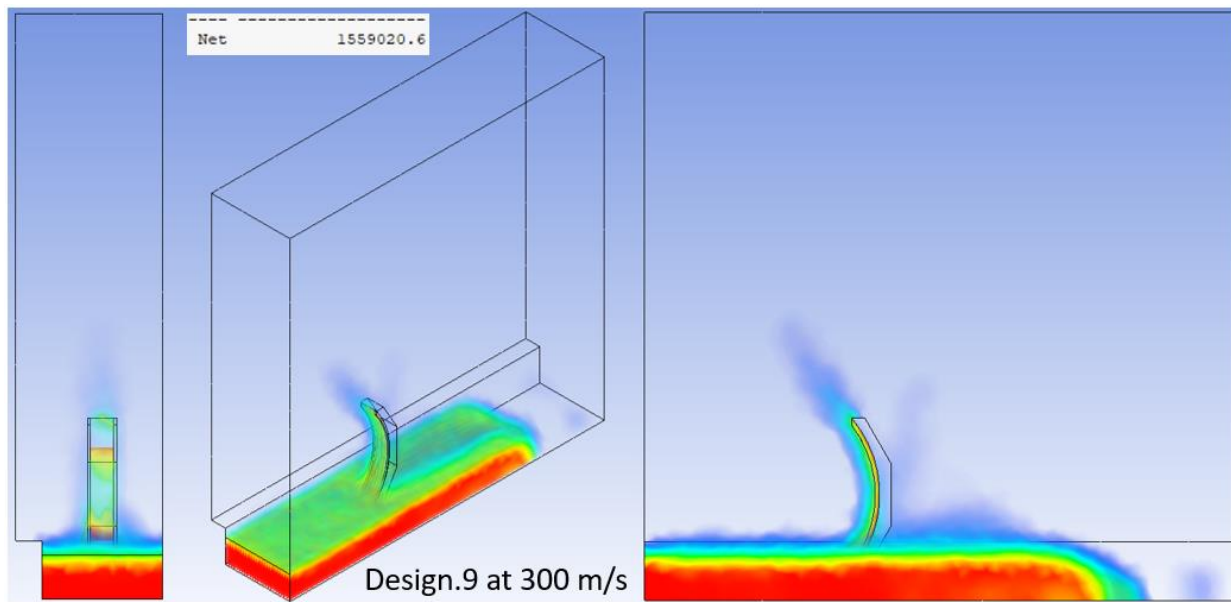
Force data is confusing to analyze due to the instability in the residuals, Plot.3.23. Plot in time shows the drop of along with the numerical instability of the residuals. Before model failure however the force seemed to be peaking at around 1,800kN. Net force in Figure 3.53 and in Plot 3.24 were captured as model was running prior to failure, the most accurate measure out of all is the top plot in Plot 3.23
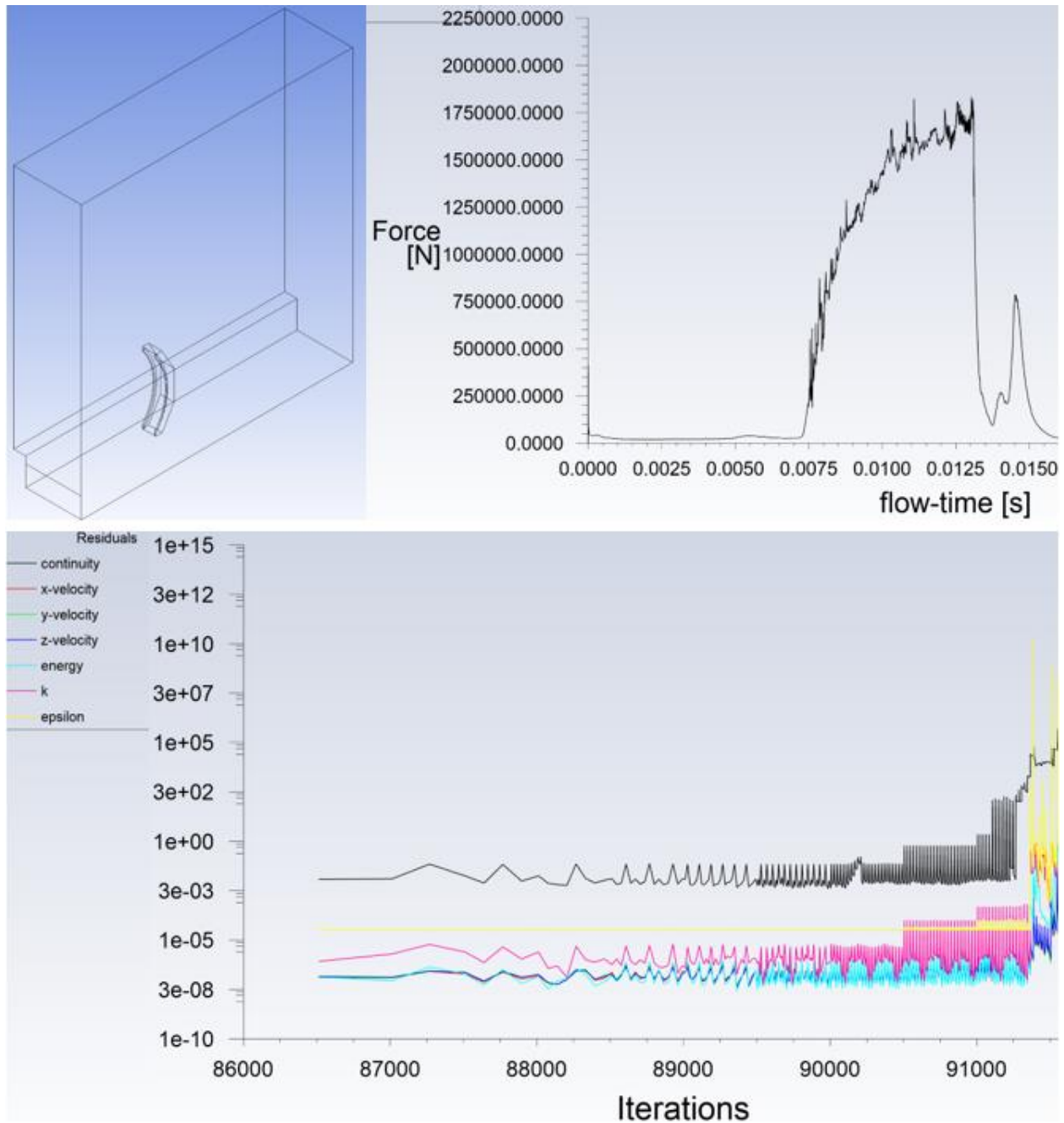
Plot 3.23: Design.9 drag force by time (top) and residuals by iteration (bottom) at 300 m/s

Index :	Distance [m]	Cumulative Force [N]
0 :	0	0
1 :	0.04952381	231222.96
2 :	0.099047619	524674.1
3 :	0.14857143	725707.21
4 :	0.19809524	897429.34
5 :	0.24761905	993646.86
6 :	0.29714286	1058385.2
7 :	0.34666667	1117316.6
8 :	0.39619048	1159424
9 :	0.44571429	1194631.5
10 :	0.4952381	1229156
11 :	0.5447619	1253325.2
12 :	0.59428571	1282377.3
13 :	0.64380952	1315389
14 :	0.69333333	1358403.8
15 :	0.74285714	1398773.6
16 :	0.79238095	1432952.9
17 :	0.84190476	1468165.9
18 :	0.89142857	1505427
19 :	0.94095238	1525143.9
20 :	0.99047619	1545666.7
21 :	1.04	1559020.6

Plot 3.24 Design.9 drag force at 300 m/s by scoop height

3.3.2.7 Conclusion

All geometric differences offer advantages depending on what is desired. Design.7 introduces side guards that channel flow very effectively increasing drag by 40%. In Designs. 8, 9, and 10 the removal of the small flat perpendicular surface to the flow reduced drag by about 8%. The cut in the bottom front of the scoop in Design.10 further reduced force by about 20%. Depending on the objective recommendations will be presented. Of particular interest is also that in Design.7 there is not a spike in velocity as compared with other designs. My hypothesis for this is that Design.7's front consists of a small vertical flat surface (perpendicular surface to flow) at it's bottom where water first makes contact that absorbed most of that velocity as reflected by the higher drag force experienced. Another discrepancy to address is a spike observed in figure 3.32 that is not present in figure 3.41, I believe the reason for this may be numerical or an issue with the mesh quality, structure, and fidelity caused by the slight change in geometry but further runs would need to be made to confirm.

Due to high reusability requirement of the pusher sled, design must be robust to perform under a wide range of testing velocities with different attached weights. It must provide braking capability at high speeds and be durable enough to last many tests. Below are four considerations when optimizing scoop and sled design.

101

1) Drag force braking sled and bringing it to a stop within a limited amount of distance

2) Lift force on sled

3) Roll force on sled

4) Damage to scoop and sled requiring maintenance and replacement.

The purpose of this study is to simulate different scoop features that affect fluid flow and make optimal scoop recommendations based on knowledge gained from the data in the different designs. For the first three on the list above, CFD can provide major design insight. Number four is limited to fluid flow and would require a fluid structure interaction (FSI) study.

The measure of pressure, force, velocity, vorticity, turbulent kinetic energy, and turbulent intensity acquired though each design was geared towards the purpose designing a scoop of optimal geometric design. Pressure offers a correlation with force, velocity in magnitude and all axis offers information about fluid flow behavior. Vorticity in magnitude and all axis provides information on eddy rotations and is correlated to turbulence which will impact forces in all directions and fluid flow. Having data in all axis for velocity and vorticity help gather perception on lift and roll that will be caused by the scoop. Turbulent kinetic energy is a description of flow intensity and turbulent intensity measures the unsteadiness of the flow. They are all important for the consideration of design as they have a direct impact on the list of four.

If the objective is to be conservative with the design and optimize for longevity and reduced risk of sled coming of the track, Design.10 would be the best with the additional feature of Design.9 60-degree angle trim from the back top part of the scoop. All quantified measures would be smaller and more stable. There would be a much smaller chance of lift, roll, and damage to the sled but it would come at the expense of the scoop main function which is to provide drag to stop the sled, about 20% less. The 20% deficit could be recovered by adding Design.7 perpendicular surfaces at the top and bottom but it would cause more turbulence. That would be the safest optimal design.

For maximum drag I would recommend Design.9 with Design.7 perpendicular surfaces, this would increase drag for Design.9 by about 8%. To offset the increase in turbulence that can

cause, lift, roll, and damage the Design.9 back top cut of 60-degree feature works best. To prove that Design.9 feature reduces turbulence and suffers no decline in force from Design.7 and Design.8 flat back top see Figure 3.54 and Plot 3.25. An additional advantage of Design.9 is that the drag produced would be the most out of all the designs once integrated with the pusher sled. The reason for this is the volumetric flow rate of water contour in Figure 3.55 shows that a larger volume of water would contact pusher component of sled and cause additional drag. It would come at the expense of potential damage and maintenance requirement, FSI study would be required.
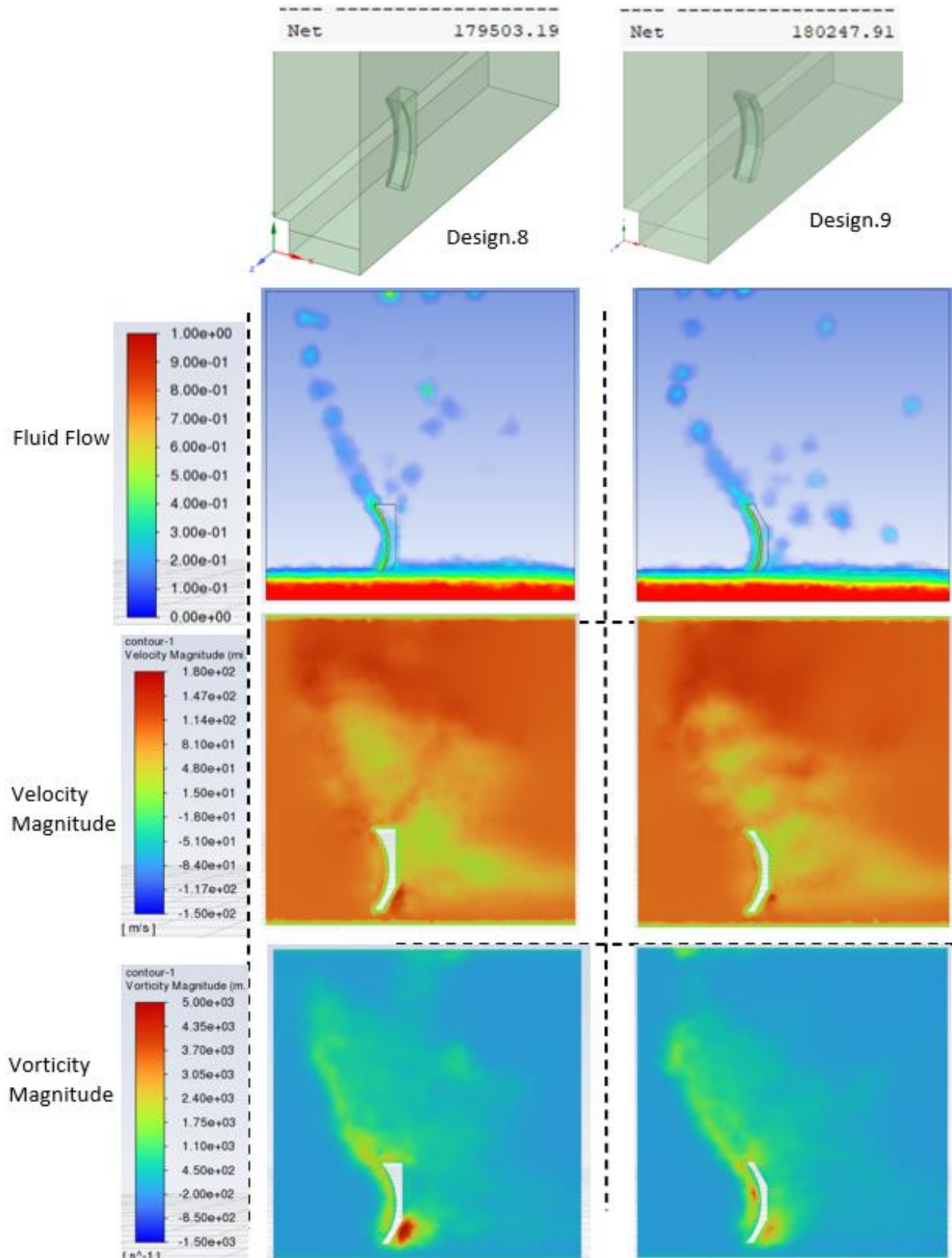
Figure 3.54: Design.8 and Design.9 qualitative comparison at 100 m/s
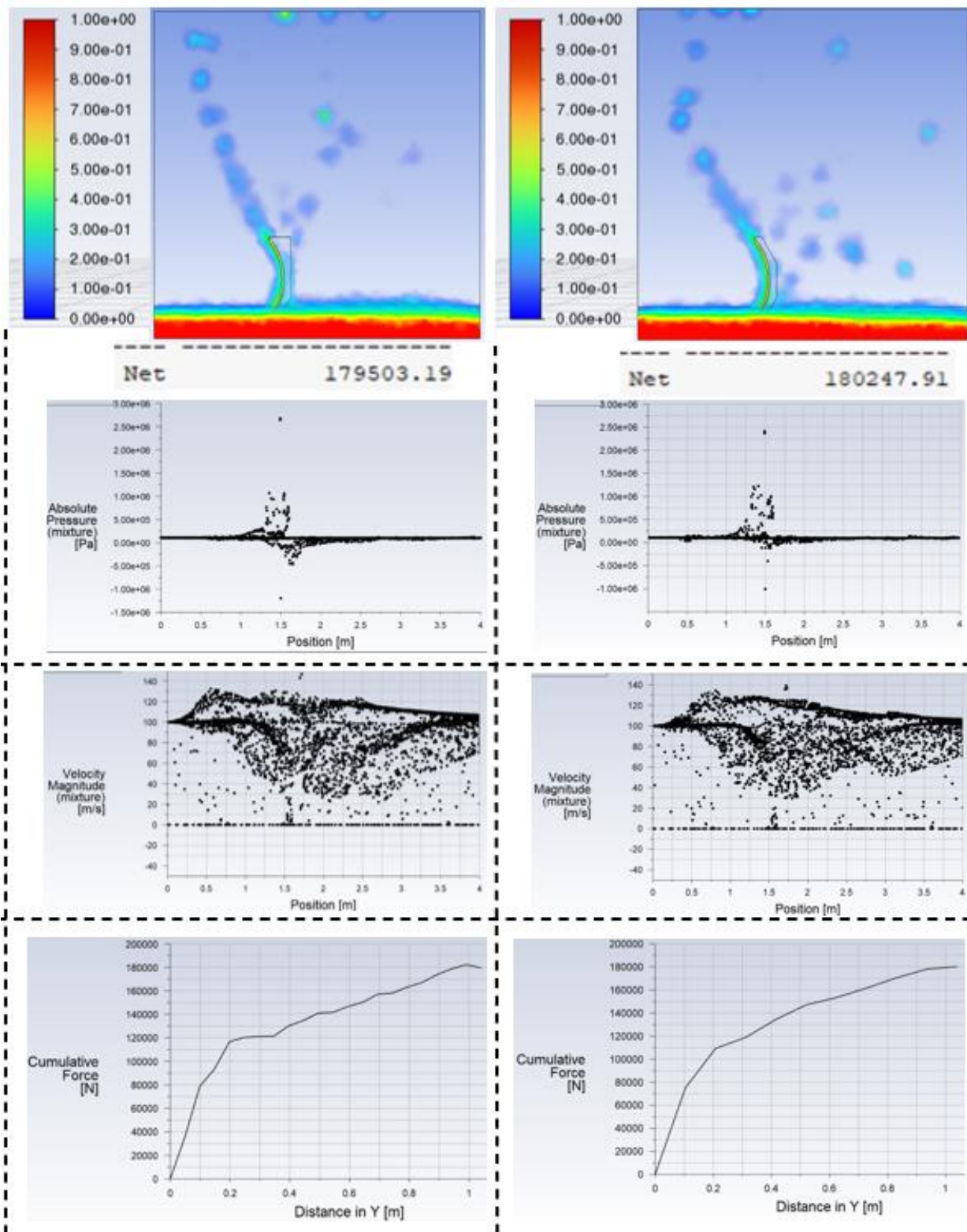
Plot 3.25: Design.8 and Design.9 quantitative comparison at 100 m/s.
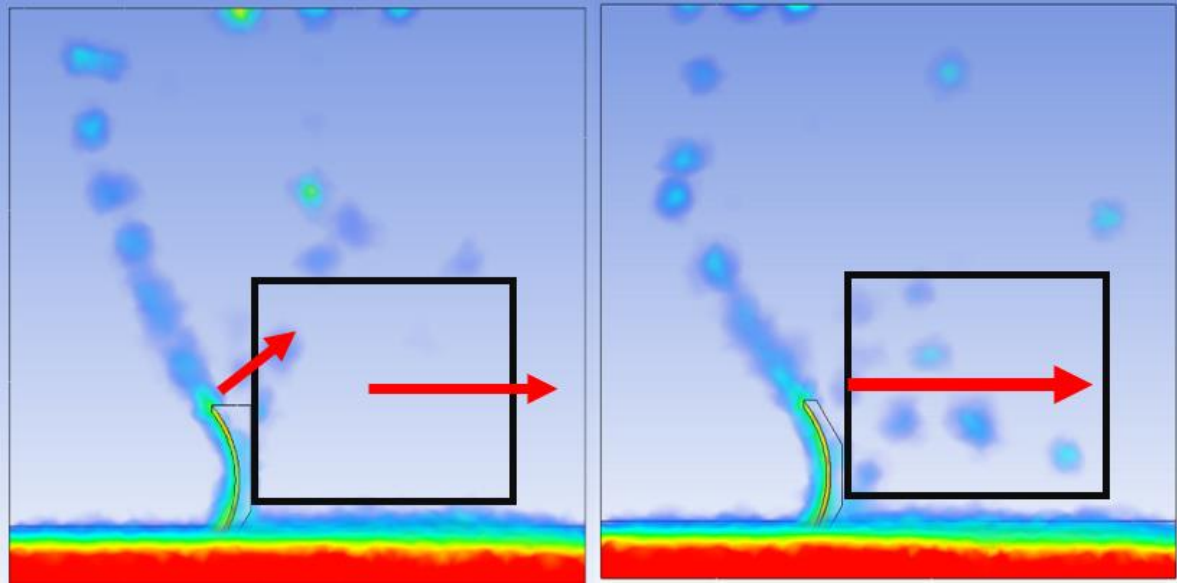
Figure 3.56: Design.8 (left) and Design.9 (right) at 100 m/s water volumetric flow rate qualitative comparison

Chapter 4: Machine Learning Framework

4.1 INTRODUCTION

In addition to providing a CFD geometric study of fluid flow through a scoop, a framework for integrating machine learning (ML) with CFD is provided. CFD is very computationally expensive each geometric design taking days to complete. ML can be very expensive but only during the training once trained results can be produced very quickly. To this end, a program framework was developed to help the research group organize and structure the integration.
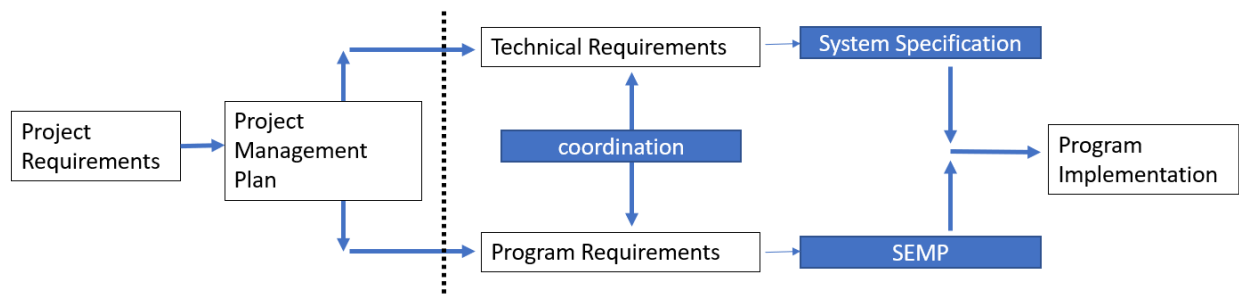
Figure 4.1: Program Framework

In figure 4.1, a program framework is displayed. It consists of two main components, one technical and one management. For the project of integration only the framework is provided, the actual development and execution will have to be done by them.

On the technical side, high level requirements are:

1) Increase fidelity of CFD models
2) Reduce time required for flow simulation
3) Reduce computational resources required for flow simulation
4) Create a robust neural network that can model flows between 100 m/s and 300 m/s fluid flow
5) Reduce training times for successive neural networks.

To meet these requirements the following technical framework is suggested, Figure 4.2.
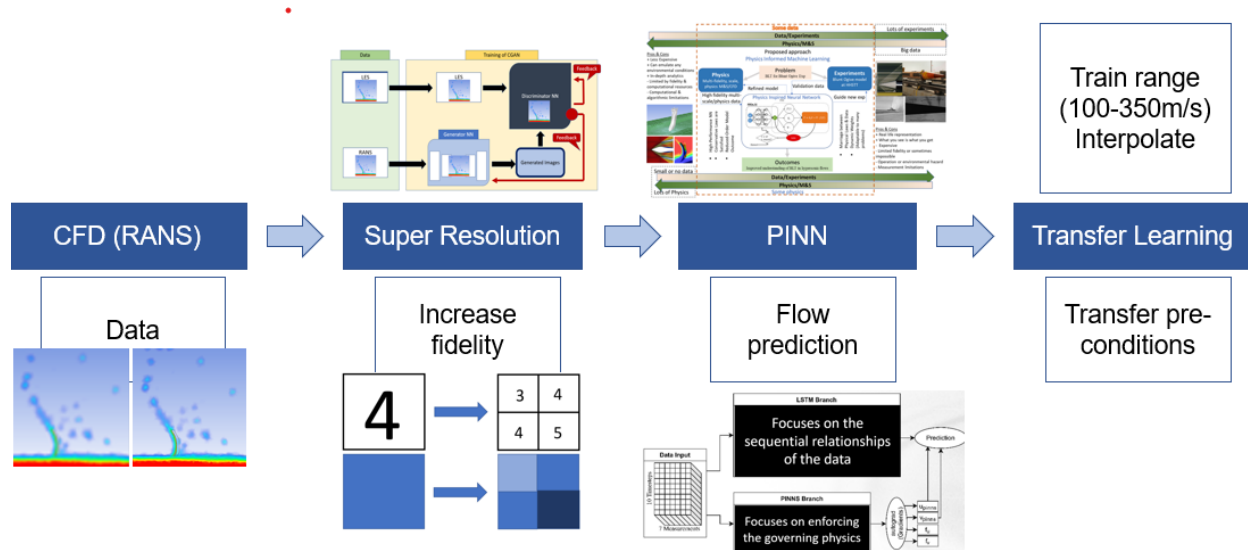
Figure 4.2: Machine Learning Framework

The CFD data in 3-D modeling is in RANS the objective of super sampling would be to increase fidelity. PINNs would reduce time requirement and computational cost of fluid simulations. Finally, using transfer learning once the initial neural net is trained at a specific velocity the next neural nets could be trained quicker.

On the project management side, Figure 4.3, the management system is broken into three major components. We have UTEP researchers, outside researchers, and computational resources. Inside UTEP would be our reaserch group comprised of engineers and computer scientists. Orange is for institutions, organizations, bureaucracies while blue are people directly involved in research work.
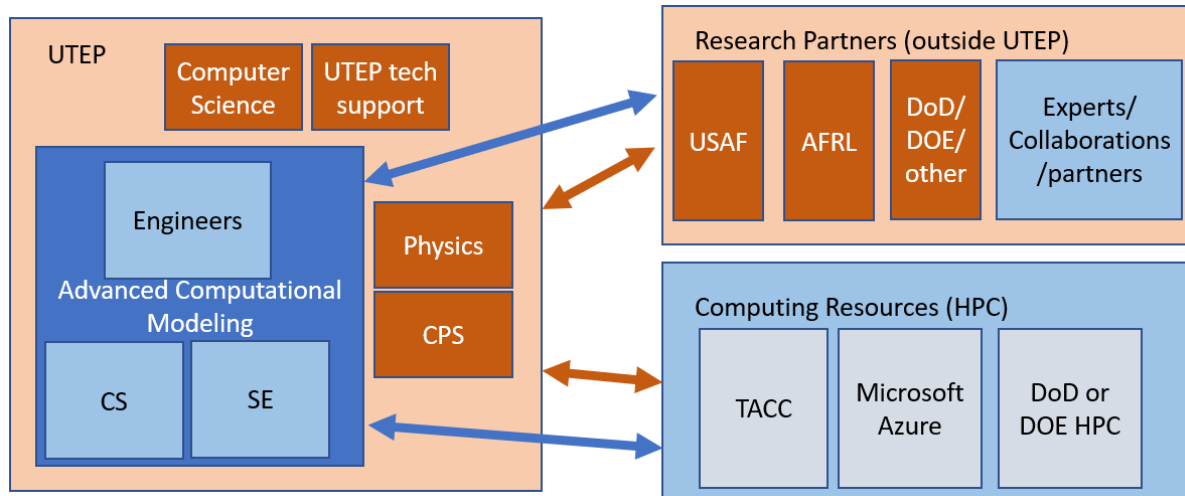
Figure 4.3: System Diagram

4.2 SUPER RESOLUTION

Super Resolution works by having two sets of data, one low resolution and the other high resolutionon. The purpose the neural network in super sampling is to find the weights that transform an area in which we have all fours into a more detailed area where they are not all fours. In figure 4.4 at the top we have a space in which the entire square are all fours, what the neural network would do is find the weights to transform the RANS low fidelity (left on Figure 4.4) to high fidelity RANS (right on Figure 4.4) and get a better "picture" as seen at the bottom of Figure 4.4.

To accomplish this two RANS models must be simulated and completed, for example one with lets say 100,000 elements and another with 400,000 elemnts. If the structures of the mesh are consistent with each other we have the situation with Figure 4.4. Then to get the transformation of low fidelity model to high fidelity model we will use a Conditional Generative Adversarial Network (cGAN), Figure 4.5.
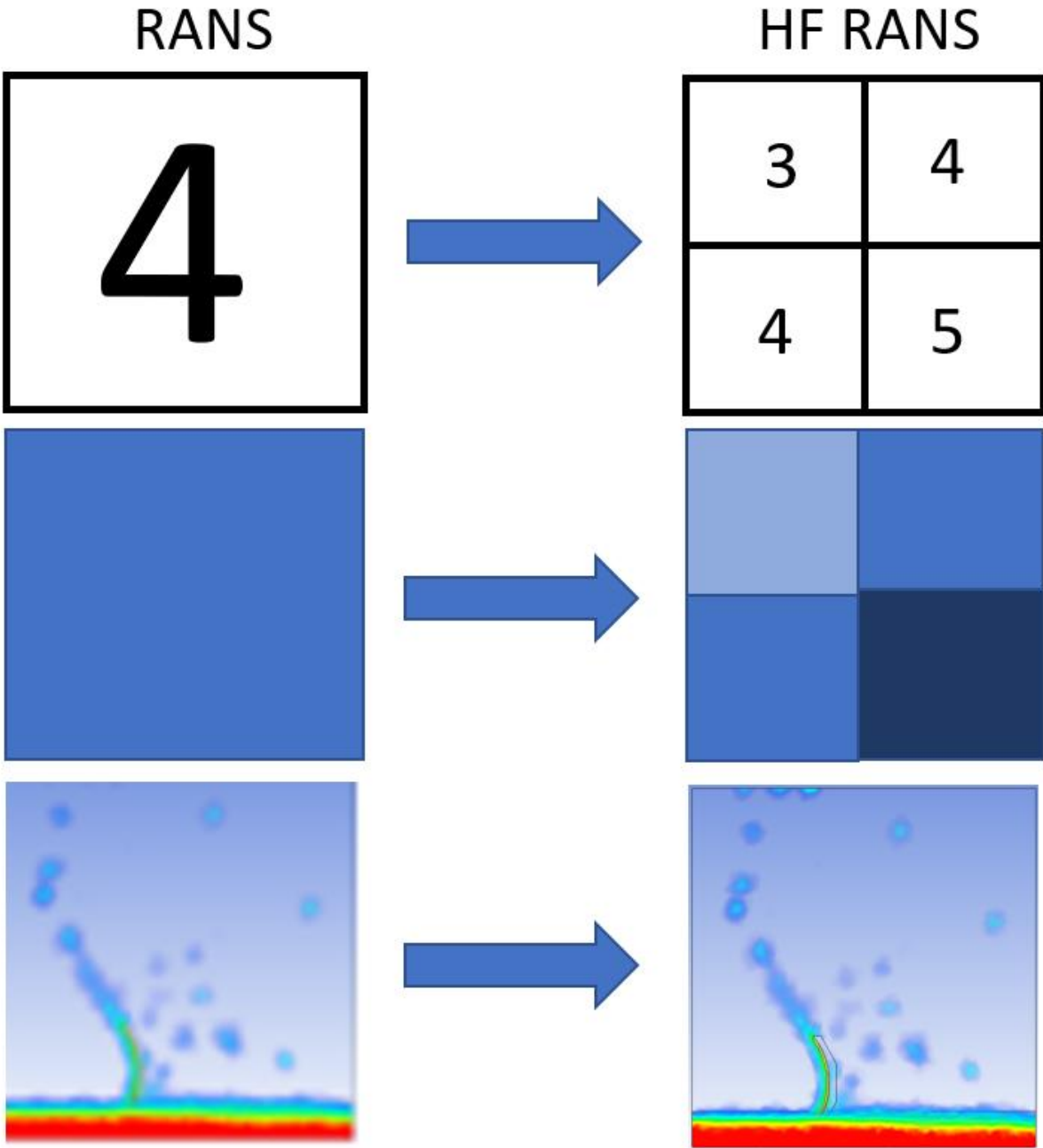
Figure 4.4: Super Resolution illustration, images on the right have more 'detail' or resolution

The way the cGAN works is by training two neural networks, one that is called the discriminator and is trained in high fidelity images. The discriminator is responosible for authentacating if an image is "real" or "fake", if it determines its "fake" there is a feedback function that provides input to our second neural net called the the generator. The generator would

be trained on lower fidelity images and would produce them to feed to the discriminator. After many iterations of producing images to fool the discriminator, the idea is that enough feedback would be provided to the generator to produce images of the quality to fool the discriminator into thinking the images it is providing it are real. At this point you have your transformation algorithm that you can use on other low-fidelity images to convert them to higher fidelity.
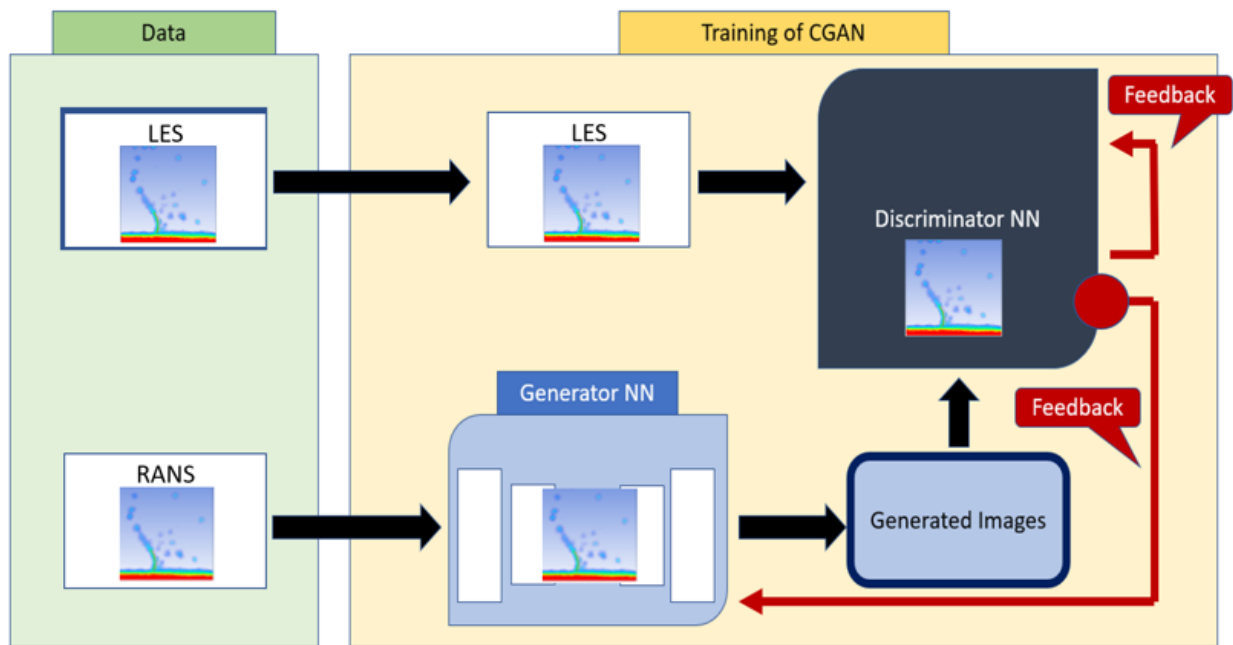
Figure 4.5: Suggested cGAN architecture for Super Resolution

Increasing the fidelity in this manner is not saying that the transformation will be exactly as a high-fidelity image, but the idea would be that the results would be closer to higher fidelity than a regular low fidelity RANS.

4.3 Physics Informed Neural Networks (PINNs)

In continuation with the theme of expensive computational modeling, the next component of the framework are PINNs. The concept of PINNs is leveraging strengths from computational modeling simulating physics with experimental data. In Figure 4.6, the general idea of PINNs is

illustrated. By leveraging both sides fluid flow can be modeled faster and accurately. PINNs is more accurate than a regular NN because it incorporates some physics and faster than traditional CFD because it doesn't solve for Navier Stokes equations.
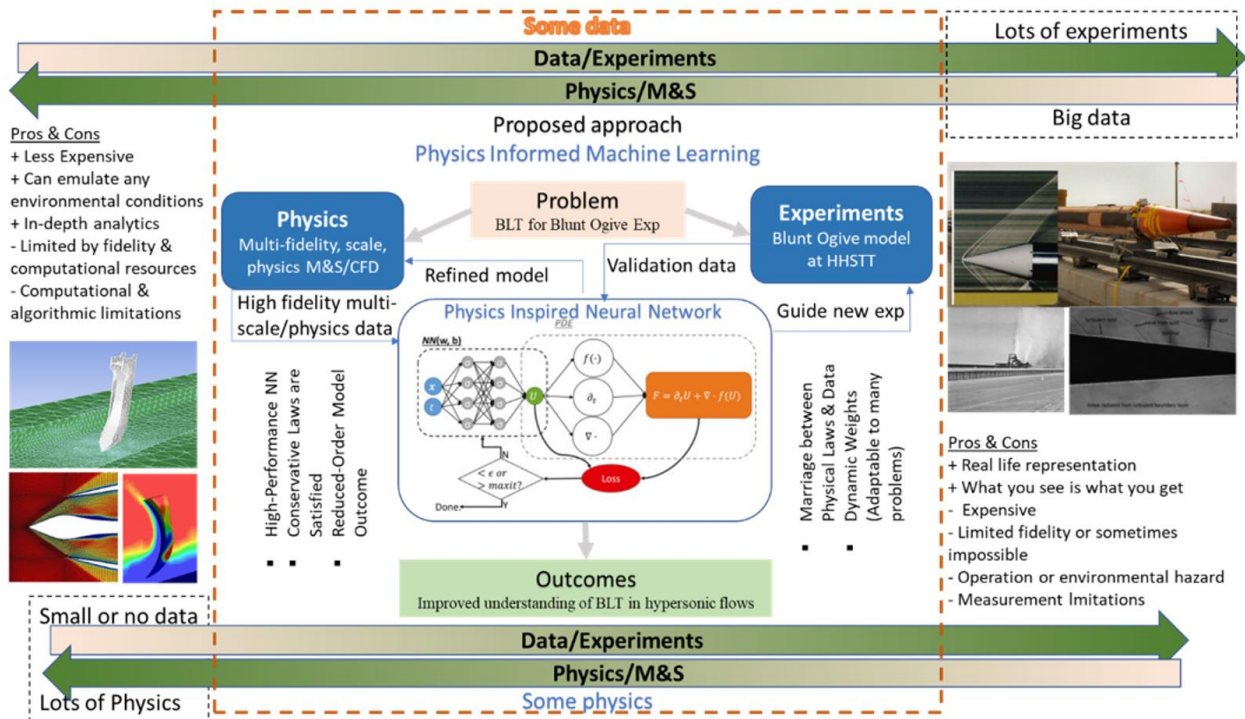
Figure 4.6: Physics Informed Neural Network function diagram

In addition to PINNs, Long Short-Term Memory (LSTM) were also used and integrated into them to create a Physics-Informed Long-Short Term Memory (PILSTM) Neural Network that would perform better than either individually, see Figure 4.7. LSTM is a type of Recurrent Neural Network (RNN) that are used for time based relationships (37). To test PINN, LSTM, and PILSTM data from a 2-D case was used for training, see Figure 4.8. The neural nets were trained on 80% of the data set from the simulation and the other 20% was used to test. To test the accuracy of the models, mean squared error of the velocity in x and y axis were used (u and v).
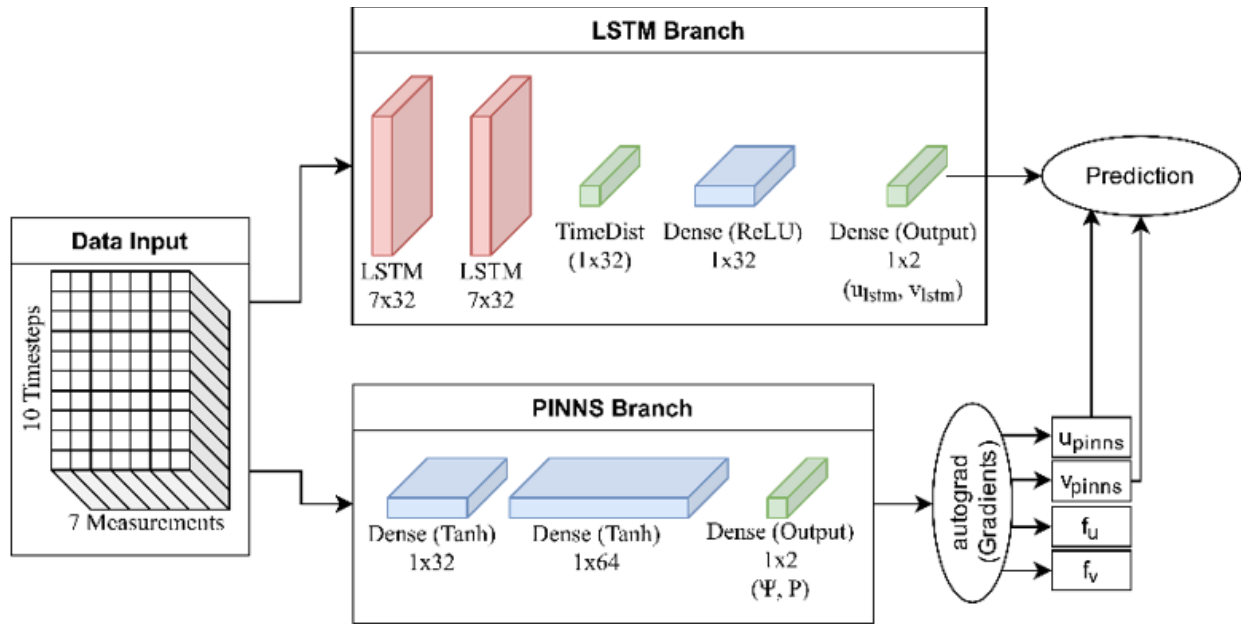
Figure 4.7: 2-D Physics-Informed Long Short-Term Memory Architecture (37)
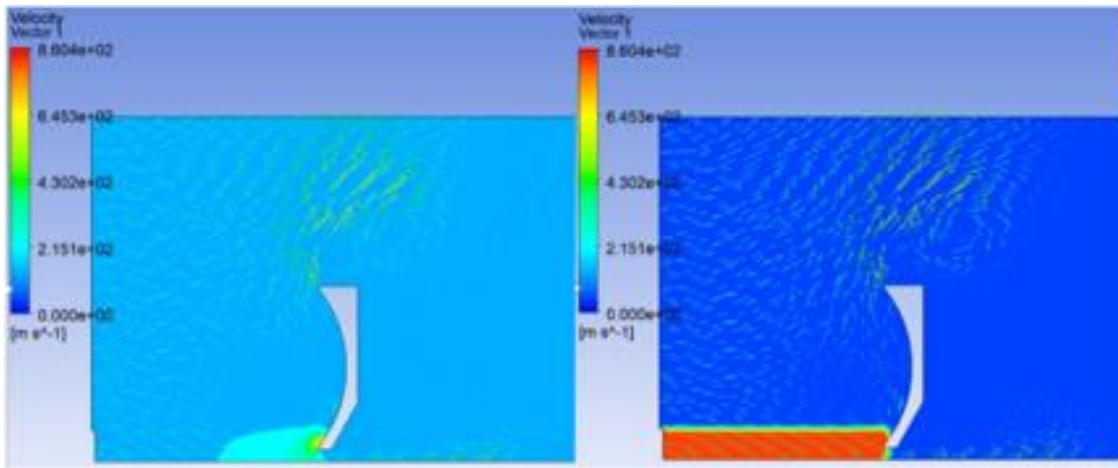
Figure 4.8: 2-D data used to train Neural Networks (37)

On Table 4.1 are the results from the 200 epochs of training. Although the values are not very accurate, with more data and time the errors can be reduced. The purpose of the work was to a proof of concept for machine learning in fluid modeling but there is still much work to do to complete and fully validate.

Table 4.1: Training Results for different Neural Networks (37)

MODEL	U	V	TRAIN TIME
BASELINE	10.01	2.69	N/A
PINNS ONLY	5709	12038	200 epochs
LSTM ONLY	1.7811	8.6962	200 epochs
PINNS+LSTM	**0.4677**	**1.2794**	200 epochs

4.4 TRANSFER LEARNING

When training a neural network essentially all that is happening is weights to convert inputs into outputs are being determined. Transfer learning capitalizes on using the weights from a previous trained network as pre-conditions for a new one, essentially having a better starting point and having a quicker training time. Transfer learning would be used to train fluid flows at small velocity changes from each other, for example once a neural network trained for fluid flow at 100 m/s the weights from it can be used as a starting point for training the same model but at 150 m/s.
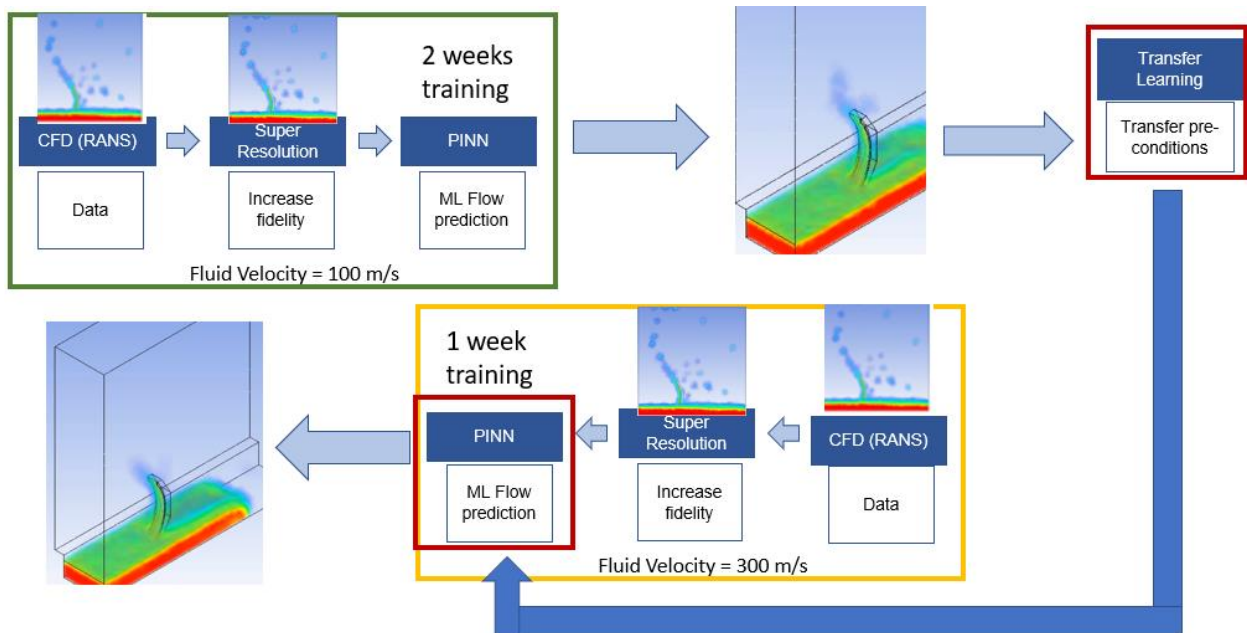
Figure 4.7: Transfer Learning Process Flow

4.5 INTEGRATION

Integrating all the models would be as follows:

1) From "quick" RANS model, fidelity would be increased using super resolution.

2) Then from the super resolution dataset a PINN would be trained for a case involving 100 m/s

3) Finally, when it comes to train a model at 150 m/s, transfer learning would be used to have the pre-existing conditions from 100 m/s trained model used to train the 150 m/s model faster.

There will be some errors associated with each step but the more training and iterations that are done should reduce it. The size of the errors would be difficult to quantify and can only be known from doing it. The utility of such framework would come from hopefully having a robust though not perfect still "useful" ML modeling algorithm that can model fluid flow very quickly with relatively little computational resources required compared to now.

4.6 PROJECT MANAGEMENT

To organize the project use cases were created, Figure 4.7, so that roles and functions can be specified. Having specific roles and functions allows for clarity and productivity. Figure 4.8 illustrates the coordination between the different functions while Figures 4.9, 10, 11, and 12 are Input, Control, Mechanism, and Output diagrams used to organize for each use case function. All diagrams in this section are color coded for easy connection between the diagrams, central block in diagram aligns with the system it belongs to in the Framework Use Case.
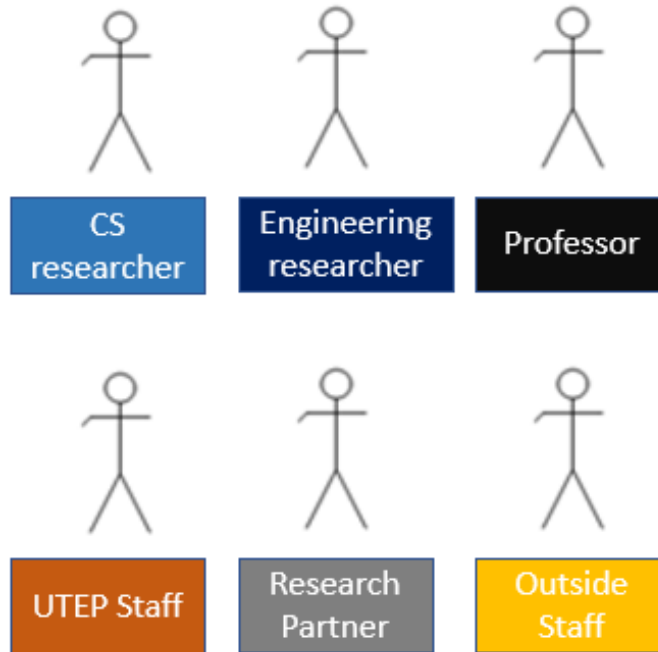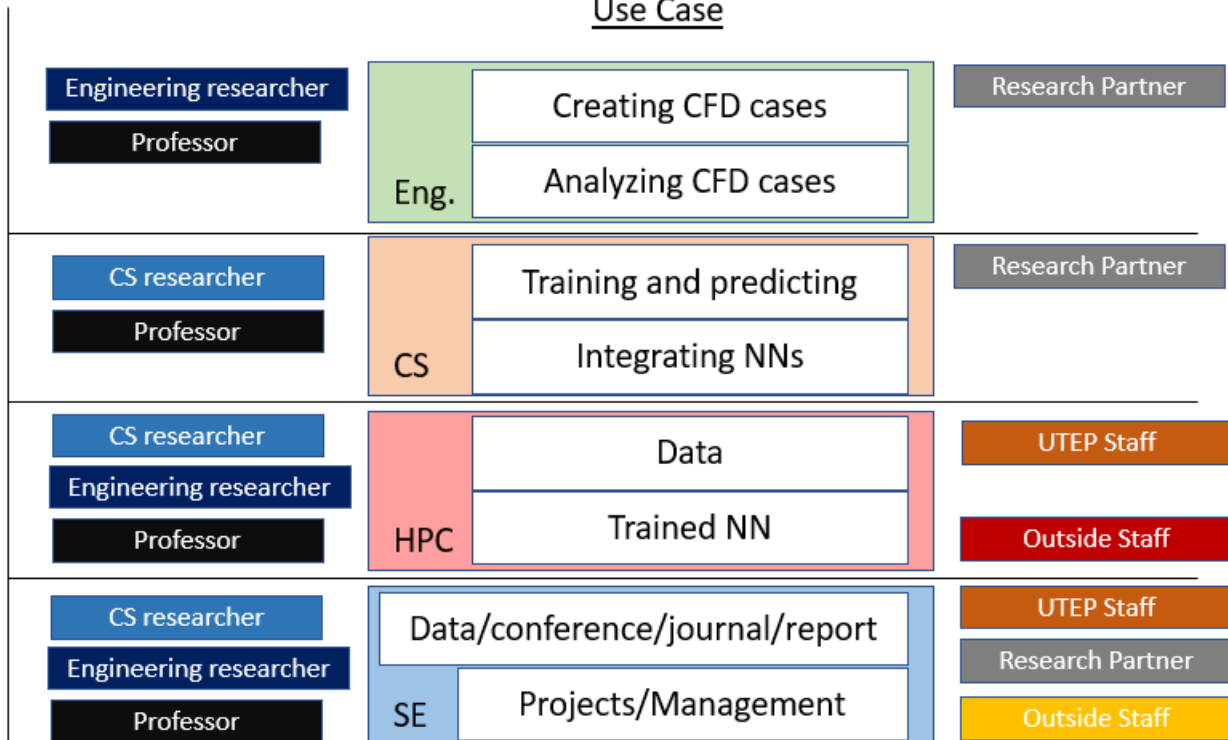
Figure 4.8: Framework Use Case
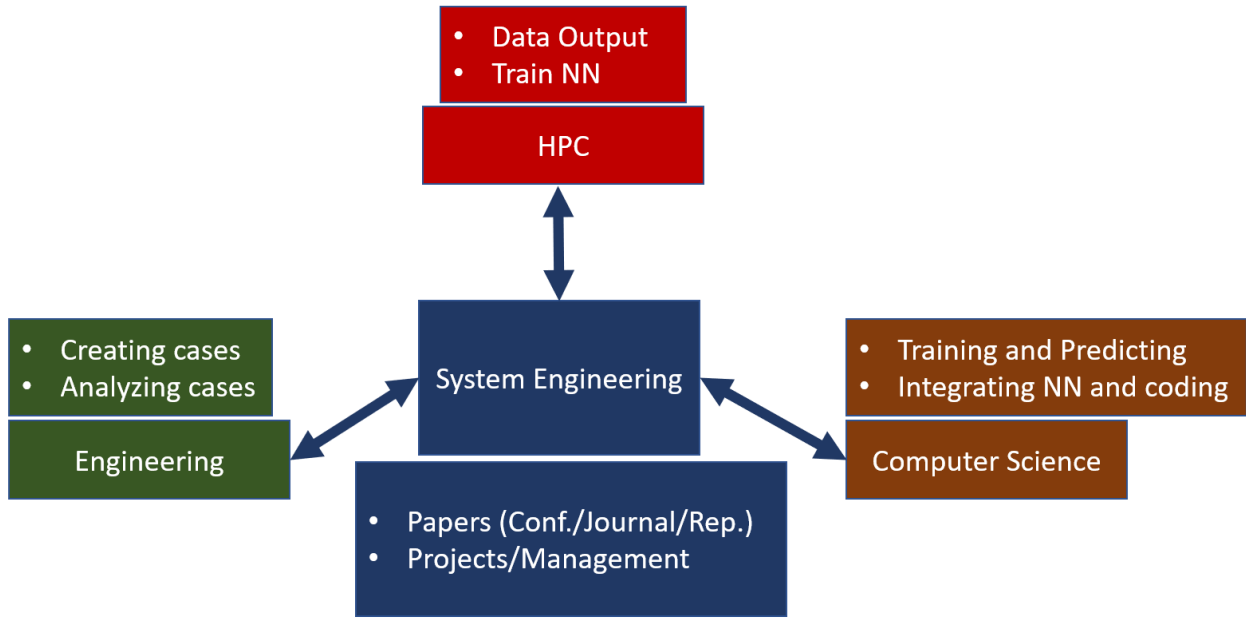
Figure 4.9: Functional Flow
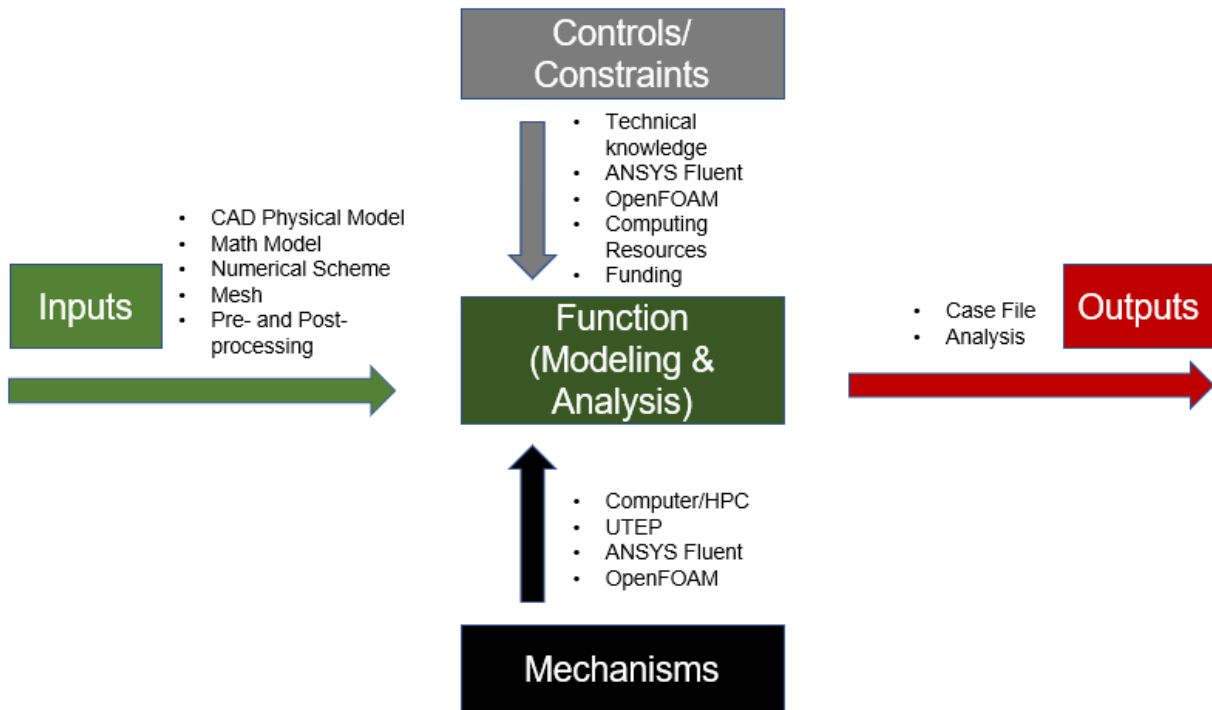
Figure 4.10: Input Control Output Mechanism diagram for Engineering Use Case
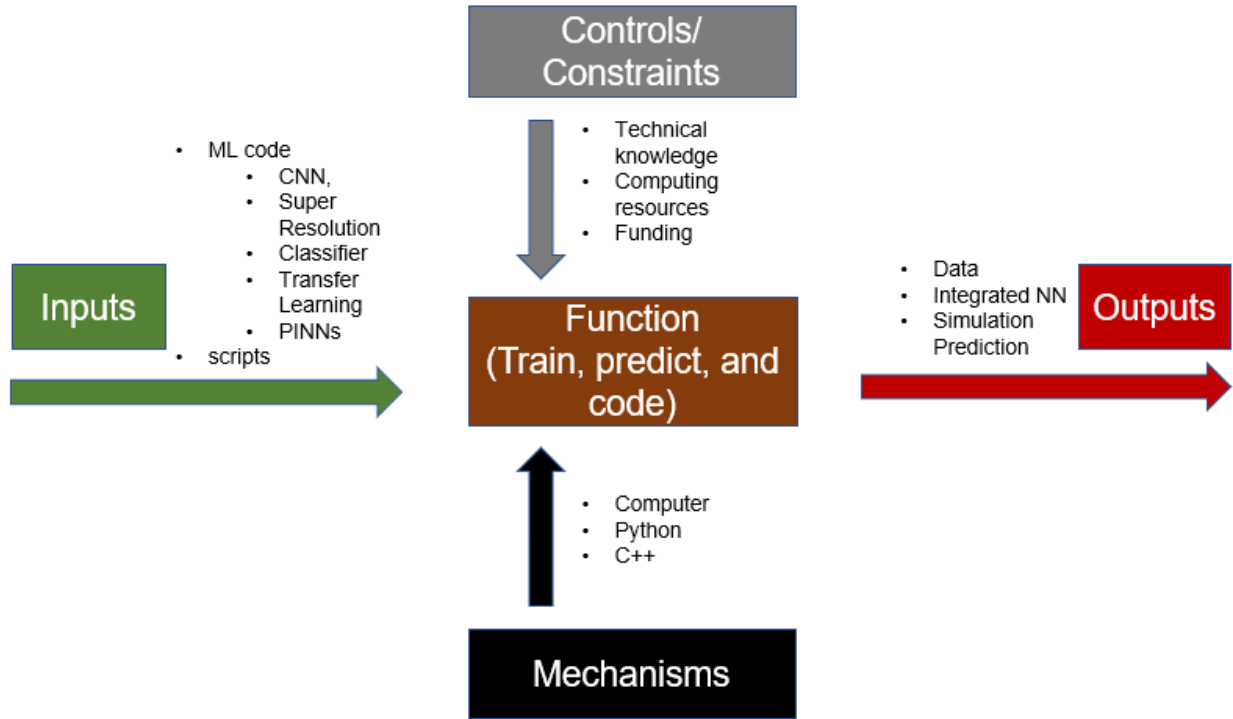
Figure 4.11: Input Control Output Mechanism diagram for Computer Science Use Case
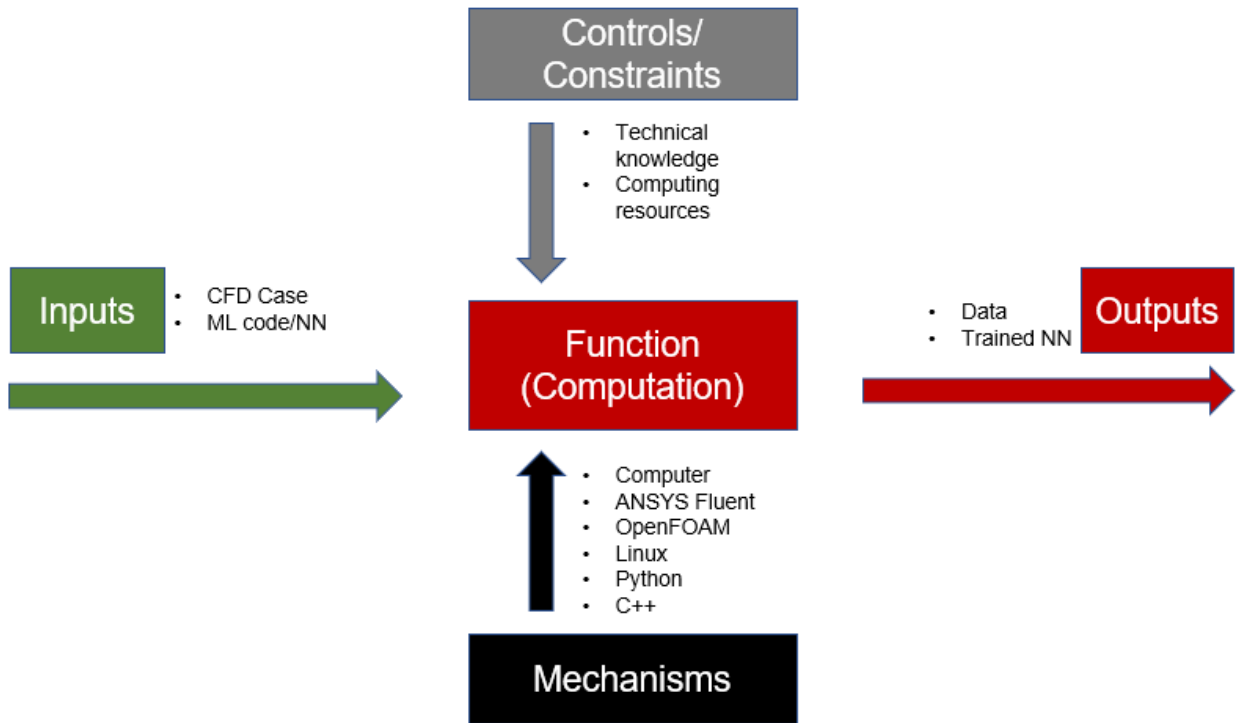
Figure 4.12: Input Control Output Mechanism diagram for High Performance Computing Use Case
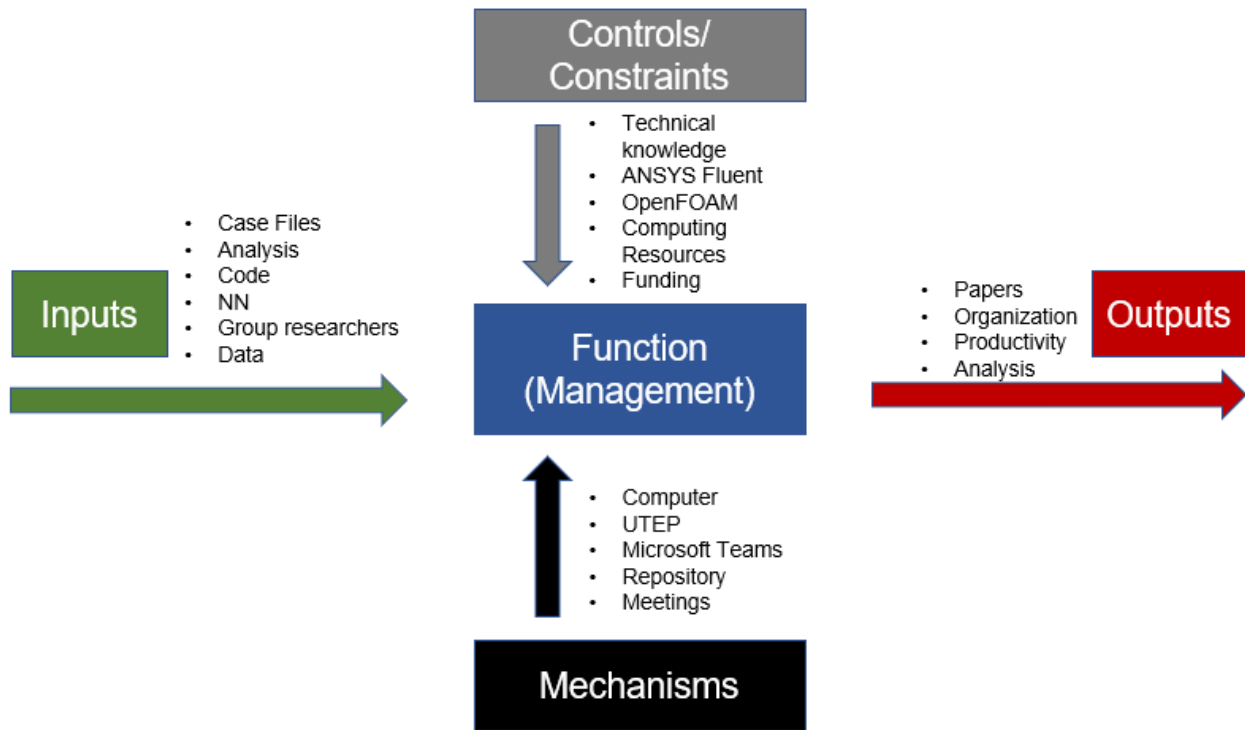
Figure 4.13: Input Control Output Mechanism diagram for Systems Engineering Use Case

Chapter 5: Conclusion

5.1 PUTTING IT TOGETHER

Before this study began, to my knowledge, there was little study of optimal geometric design for the water braking scoop and of the fundamental problems of:

- How does boundary layer transition influence turbulence and the effects of drag and lift forces acting on the sled?

- How effective can CFD be in modeling multi-physics phenomena and how may this tool be leveraged to improve capability of testing capability at HHSTT?

- How can advances in machine learning be leveraged to mitigate computational expense associated with CFD?

My contribution to HHSTT would be the study of scoop design, geometric features, their impact on braking capability, and optimal scoop design features. Furthermore, I have created a

framework to integrate CFD with ML that will hopefully lead to faster useful fluid simulations at lower computational costs that my research group can continue to implement in future studies. Additional contributions and completed objectives by this work:

- Quantification of scoop design and geometric features impact on braking capability.

- Framework to integrate CFD with ML

- Literature on high-speed test track water braking

- Model three-dimensional multi-phase flows

- Identify geometric features that improve sled drag performance and quantify such improvements

- Perform sensitivity analysis on different modeling parameters

- Develop framework to address high computational cost, fidelity, and turnaround time associated with computational fluid dynamics

The study was important because it identified geometric design features to improve braking capability, allowing for braking at higher velocities and improving braking through increased drag from water. Improving water braking can lead to an optimized aerodynamic design of the scoop. This would allow the sled to reach and sustain higher velocities profiles while maintaining recoverability capability. From a scientific perspective although more work is required for further analysis the following research questions have been answered to an extent that there is value in the work and its study should be continued.

- How does boundary layer transition influence turbulence and the effects of drag and lift forces acting on the sled?

- How effective can CFD be in modeling multi-physics phenomena and how may this tool be leveraged to improve capability of testing capability at HHSTT?

- How can advances in machine learning be leveraged to mitigate computational expense associated with CFD?

5.2 LESSONS AND FUTURE WORK

In the development of the 3D predictive model, convergence issues associated with the numerical mesh, initial/boundary conditions, and compressibility of the fluids were encountered. Once all fluid flow scales are resolved, the effect of inflow velocities of water and air on the braking of the sled can be studied at its finest scales. Though optimal scoop designs were determined for two different conditions, further study is required for different velocity profiles, water levels, fluid structure interaction, integration of the scoop with the rest of the pusher sled, mesh dependency study, as well as higher fidelity turbulence modeling. However, computational Fluid Dynamics is very computationally expensive so a framework for integrating machine learning with CFD would be useful to speed up modeling. Though there will be issues with errors, the more data that is fed into the networks the more accurate it will become. Reynolds-Averaged Navier Stokes can provide an average estimate of all the scales, which could be used as training data, although the most accurate way to do it would be through LES or DNS. Higher fidelity models would be needed to study turbulence and boundary layer transition in greater detail, for mesh dependency studies, and to provide more accurate data for machine learning neural net. Finally, CFD integration with ML could be useful, even if it is not as accurate as CFD alone. Verification, validation, integration, and testing should be completed and implemented into the developed framework.

Many simulations failed due to poor mesh quality, element type, and structure near curves and sharp edges. Suggestions and/or corrections were using double precision, implicit to explicit model, higher fidelity, better quality mesh by having it structured, reducing time step size, having 2nd order upwind and k-w turbulence models. CFD requires large amount of computational resources, simulations were done on personal computer, hence limitation on mesh quality, element number, time steps, and models recommend running in HPC on an unrestricted ANSYS Fluent license if possible/available.

Some research questions for future work include:

- How do vibrations, caused by fluid flow and sled bounce, impact sled and the forces acting on it?

- How do shockwave interactions impact turbulence and forces acting on sled? How does it impact testing safety and results?

- How does temperature driven effects from friction of both air and water at hypersonic speed influence ablation of sled slippers?

References

1. Hooser, M., Schwing, A.: Validation of dynamic simulation techniques at the Holloman High-Speed Test Track. In: 38th Aerospace Sciences Meeting and Exhibit. American Institute of Aeronautics and Astronautics

2. Turnbull, D., Hooser, C., Hooser, M., Myers, J.: Soft Sled Test Capability at the Holloman High-Speed Test Track. In: U.S. Air Force T&E Days 2010. American Institute of Aeronautics and Astronautics

3. Kennan, Z.A.: Determination of the constitutive equations for 1080 steel and vascomax 300. AIR FORCE INST OF TECH WRIGHT-PATTERSON AFB OH SCHOOL OF ENGINEERING AND MANAGEMENT (2005)

4. Minto, D.: CTEIP Funded Advances in Hypersonic Testing at The Hollman High-Speed Test Track. In: 24th AIAA Aerodynamic Measurement Technology and Ground Testing Conference. American Institute of Aeronautics and Astronautics

5. Marren, D., Lu, F.: Advanced Hypersonic Test Facilities. American Institute of Aeronautics and Astronautics (2002)

6. Minto, D.: The Holloman High-Speed Test Track Hypersonic Upgrade Program. In: 22nd AIAA Aerodynamic Measurement Technology and Ground Testing Conference. p. 3034

7. Minto, D.: Recent increases in hypersonic test capabilities at the Holloman High-Speed Test Track. In: 38th Aerospace Sciences Meeting and Exhibit. p. 154 (2000)

8. Minto, D.W., Bosmajian, N.: Hypersonic test capabilities at the Holloman high-speed test track. Prog. Astronaut. Aeronaut. 198, 499–530 (2002)

9. Cinnamon, J.D., Palazotto, A.N.: Analysis and simulation of hypervelocity gouging impacts for a high-speed sled test. Int. J. Impact Eng. 36, 254–262 (2009).

10.   Factor, L.: Holloman High-Speed Test Track Design Manual. Res. Summ. 1, 2 (2005)

11.   Maker, D., Meyer, C.: Reusable thrust-powered sled mounted on an inclined track for launching spacecraft and airborne vehicles at supersonic speeds, (2006)

12.   RASMUSSEN, H.: Captive flight testing by means of rocket sleds. In: 3rd Aerodynamics Testing Conference. p. 364 (1968)

13.   Uncapher, W.L., Hohnstreiter, G.F.: Radioactive material package testing capabilities at Sandia National Laboratories. Sandia National Labs., Albuquerque, NM (United States) (1995)

14.   Bower, W., Kibens, V., Cary, A., Alvi, F., Raman, G., Annaswamy, A., Malmuth, N.: High-frequency excitation active flow control for high-speed weapon release (HIFEX). In: 2nd AIAA Flow Control Conference. p. 2513 (2004)

15.   Schetz, J.A.: Aerodynamics of high-speed trains. Annu. Rev. Fluid Mech. 33, 371–414 (2001)

16.   Hong-Qi, T.: Study evolvement of train aerodynamics in China [J]. J. Traffic Transp. Eng. 1, 1–9 (2006)

17.   Weinstein, L.M., Minto, D.: Focusing schlieren photography at the Holloman high-speed test track. In: 22nd International Congress on high-speed photography and photonics. pp. 865–874. International Society for Optics and Photonics (1997)

18.   Nakata, D., Yajima, J., Nishine, K., Higashino, K., Tanatsugu, N., Kozu, A.: Research and development of high-speed test track facility in Japan. In: 50th AIAA Aerospace Sciences Meeting including the New Horizons Forum and Aerospace Exposition. p. 928 (2012)

19.   Gidaspow, D.: Multiphase flow and fluidization. (1994)

20.   Kotteda, V.M.K., Kumar, V., Spotz, W.: Dakota Integrated with MFiX for UQ Analysis:

Sensitivity of particle size on the pressure in a fluidized bed DEM simulations. In: 2018 Workshop on Multiphase Flow Science. National Energy Technology Laboratory (2018)

21. Delgado, P., Chen, F., Kumar, V., Harris, C., Katta, K.: Simulation Of Single And Two-Phase Newtonian Flow In Carbon Capture And Storage Processes Using Variational Methods.

22. ASME: Guide for Verification and Validation in Computational Solid Mechanics. Am. Soc. Mech. Eng. (2006).

23. Oberkampf, W.L., Trucano, T.G.: Verification and validation in computational fluid dynamics. Prog. Aerosp. Sci. (2002).

24. Sargent, R.G., Balci, O.: History of verification and validation of simulation models. In: Proceedings - Winter Simulation Conference (2018)

25. Kleijnen, J.P.C.: Verification and validation of simulation models. Eur. J. Oper. Res. (1995). doi:10.1016/0377-2217(94)00016-6

26. Jayanti, S.: Computational Fluid Dynamics for Engineers and Scientists. (2018)

27. CFD-Committee: Guide: Guide for the Verification and Validation of Computational Fluid Dynamics Simulations. (2002)

28. Muller, Jens-Dominik (2016) *Essentials of Computational Fluid Dynamics*. Boca Raton, FL: Taylor & Francis Group.

29. Geron, Aurelien. (2017). *Hands-On Machine Learning with Scikit-Learn & TensorFlow*. Sebastopol, CA: O'Reilly.

30. D. A. L. Jimenez, "Implementing Large Eddy Simulation to Numerical Simulation of Optical Wave Propagation," 2018.

31. Goodfellow I., Pouget-Abadie J., Mirza M., Xu B., Warde-Farley D., Ozair S., Courville

A., Bengio Y., "Generative Adverserial Nets", NIPS, 2014.

32. Radfor A., Metz L., Chintala S., "Unsupervised Representation Learning with Deep Convolutional Generative Adversarial Networks", arXiv:1511.06434v2, 2016.

33. Schawinski K., Zhang C., Zhang H., Fowler L., Santhanam G.K., "Generative adversarial networks recover features in astrophysical images of galaxies beyond the deconvolution limit", *Monthly Notices Royal Astronomical Soc.: Lett.*, vol. 467, no. 1, pp. L110-L114, May 2017.

34. Terrazas, J., Kotteda, V. M. Krushnarao, Kumar, V., Edmonds R. & Zeisset M., The CFD Modeling of the Water Braking Phenomena for the Holloman High-Speed Test Track, presented at the ASME-JSME-KSME 2019 8th Joint Fluids Engineering Conference in San Francisco, CA.

35. L.F.R. Sanchez, "Machine Learning Analysis to Characterize Phase Variations in Lasre Propagation Through Deep Turbulence," 2020.

36. M Raissi, P Perdikaris, GE Karniadakis - Journal of Computational Physics, 2019

37. Jose Perez, Rafael Baez, Jose Terrazas, Arturo Rodriguez, Daniel Villanueva, Olac Fuentes, Vinod Kumar, Brandon Paez, Abdiel Cruz, Physics-Informed Long-Short Term Memory Neural Network Performance on Holloman High-Speed Test Track Sled Study, FEDSM2022, August 1-3, 2022, Toronto, Canada

Vita

Jose Terrazas received his B.S. in Mechanical Engineering, M.S. in Systems Engineering as well as Computational Science, and a Graduate Certificate in Big Data Analytics from The University of Texas at El Paso (UTEP). He is currently pursuing a PhD in Mechanical Engineering at UTEP under Dr. Vinod Kumar.

Areas of research include multi-phase modeling in water braking phenomena during high-speed braking using Computational Fluid Dynamics (CFD) and Machine Learning (ML) for the deconvolution of turbulence in images. He has received recognition by the Office of Research and Sponsored Projects at UTEP and was recognized for demonstrated excellence and skill in Project and Systems Engineering Management. In addition, Jose was a 2018, 2019, and 2021 Air Force Research Lab Summer Student Fellow.